Nonlinear dynamics of elementary rotor systems with compliant plain journal bearings

Citation for published version (APA):
Vrande, van de, B. L. (2001). *Nonlinear dynamics of elementary rotor systems with compliant plain journal bearings*. [Phd Thesis 1 (Research TU/e / Graduation TU/e), Mechanical Engineering]. Technische Universiteit Eindhoven. https://doi.org/10.6100/IR550147

DOI:
10.6100/IR550147

Document status and date:
Published: 01/01/2001

Document Version:
Publisher’s PDF, also known as Version of Record (includes final page, issue and volume numbers)

Please check the document version of this publication:

• A submitted manuscript is the version of the article upon submission and before peer-review. There can be important differences between the submitted version and the official published version of record. People interested in the research are advised to contact the author for the final version of the publication, or visit the DOI to the publisher's website.
• The final author version and the galley proof are versions of the publication after peer review.
• The final published version features the final layout of the paper including the volume, issue and page numbers.

Link to publication

General rights
Copyright and moral rights for the publications made accessible in the public portal are retained by the authors and/or other copyright owners and it is a condition of accessing publications that users recognise and abide by the legal requirements associated with these rights.

- Users may download and print one copy of any publication from the public portal for the purpose of private study or research.
- You may not further distribute the material or use it for any profit-making activity or commercial gain
- You may freely distribute the URL identifying the publication in the public portal.

If the publication is distributed under the terms of Article 25fa of the Dutch Copyright Act, indicated by the “Taverne” license above, please follow below link for the End User Agreement:

www.tue.nl/taverne

Take down policy
If you believe that this document breaches copyright please contact us at:

openaccess@tue.nl

providing details and we will investigate your claim.

Download date: 04. Oct. 2023

NONLINEAR DYNAMICS OF ELEMENTARY ROTOR SYSTEMS WITH COMPLIANT PLAIN JOURNAL BEARINGS

CIP-DATA LIBRARY TECHNISCHE UNIVERSITEIT EINDHOVEN

Vrande, Bram L. van de

Nonlinear dynamics of elementary rotor systems with compliant plain journal bearings / by Bram L. van de Vrande. – Eindhoven : Technische Universiteit Eindhoven, 2001.
Proefschrift. – ISBN 90-386-2623-1
NUGI 834
Trefwoorden: rotordynamica / rotors ; niet-lineaire dynamica / rotors ; glijlagers
Subject headings: rotor dynamics / rotors ; nonlinear dynamics / rotors ; journal bearings

Printed by Drukkerij Laurasia B.V., Rijen, The Netherlands

NONLINEAR DYNAMICS OF ELEMENTARY ROTOR SYSTEMS WITH COMPLIANT PLAIN JOURNAL BEARINGS

PROEFSCHRIFT

ter verkrijging van de graad van doctor aan de
Technische Universiteit Eindhoven, op gezag van de
Rector Magnificus, prof.dr. R.A. van Santen, voor een
commissie aangewezen door het College voor
Promoties in het openbaar te verdedigen
op 12 december 2001 om 16.00 uur

door

Bram Lodewijk van de Vrande

geboren te Delft

Dit proefschrift is goedgekeurd door de promotoren:

prof.dr.ir. D.H. van Campen
en
prof.dr.ir. E.A. Muijderman

Copromotor:
dr.ir. A. de Kraker

To my wife
Anne-Françoise

Contents

Samenvatting

In veel praktische situaties worden zogenaamde vervormbare glijlagers, dat wil zeggen, glijlagers met een relatief elastisch loopvlak gebruikt. Een voorbeeld van een vervormbaar glijlager is het watergesmeerde rubber glijlager dat wordt gebruikt om de schroefas in schepen te ondersteunen. Vanwege het feit dat glijlagers niet-lineaire elementen zijn, kunnen zij een significante invloed hebben op de dynamica van een rotor-lager systeem. Echter, de dynamica van grote rotor-lager systemen wordt in het algemeen bestudeerd met behulp van lineaire modellen, waarbij de glijlagers zijn gelineariseerd rond een evenwichtspositie. Voor een beter inzicht in de dynamica van een niet-lineair rotor-lager systeem dient een niet-linear dynamische analyse te worden uitgevoerd.

In dit proefschrift zijn vervormbare korte en lange gewone glijlagermodellen voor rotordynamische toepassingen ontwikkeld. Deze modellen bestaan uit ruimtelijk gediscretiseerde niet-lineaire partiële differentiaalvergelijkingen, wat in feite grote stelsels niet-lineaire gewone differentiaalvergelijkingen zijn. Vanwege de dimensie van deze stelsels, zijn de standaardmethodes om trillingen van niet-lineair dynamische systemen te berekenen te inefficiënt. Derhalve is tevens een efficiënte numerieke methode om trillingen van partiële differentiaalvergelijkingen te berekenen ontwikkeld.

De niet-lineaire dynamica van een rotor-lager syteem met een starre rotor in twee vervormbare glijlagers is bestudeerd voor verschillende waarden van de relatieve vervormbaarheid van het loopvlak, met gebruikmaking van zowel het korte als het lange lagermodel. Het blijkt dat verhogen van de relatieve vervormbaarheid van het loopvlak de stabiliteitsgrens van een gebalanceerde rotor in vervormbare korte glijlagers verlaagt, terwijl het de stabiliteitsgrens van dezelfde rotor in vervormbare lange glijlagers verhoogt. Voor een ongebalanceerde rotor in vervormbare korte glijlagers heeft de relatieve vervormbaarheid van het loopvlak een significante invloed op de rotorsnelheden waarbij de tak van synchrone trillingen van stabiliteit verandert en op de vorm van de tak van subsynchrone trillingen. Voor dezelfde rotor in vervormbare lange glijlagers veroorzaakt verhogen van de relatieve vervormbaarheid van het loopvlak een verhoging van de rotorsnelheid waarbij de tak van synchrone trillingen instabiel wordt. Het blijkt dat in tegenstelling tot starre glijlagermodellen de minimale filmdikte van de vervormbare glijlagermodellen nul en zelfs negatief kan worden. Met andere woorden, de vervormbare glijlagermodellen voorspellen de mogelijkheid van contact tussen de as en het lager. Omdat contact niet is opgenomen in de modellen kunnen fysisch onmogelijke trillingen met negatieve filmdiktes gevonden worden. Voor starre glijlagermodellen kan contact helemaal niet optreden vanwege het

feit dat ofwel een oneindig grote belasting ofwel een oneindig lange tijd nodig zou zijn.

Tijdens experimenten aan een rotor-lager systeem met een flexibele as in een watergesmeerd rubber glijlager is een niet-lineair fenomeen waargenomen. De tak van synchrone trillingen bevat twee zogenaamde cyclic folds, waarbij de tak van richting verandert. Als de rotorsnelheid gevarieerd wordt voorbij één van deze cyclic folds, springt het systeem naar een afgelegen deel van de tak van synchrone trillingen. Dit fenomeen wordt waarschijnlijk veroorzaakt door de niet-lineaire elasticiteit van het rubber loopvlak van het watergesmeerde rubber glijlager.

Summary

In many practical situations, so-called compliant journal bearings, that is, journal bearings with a relatively elastic bearing liner are used. An example of a compliant journal bearing is the water-lubricated rubber-lined journal bearing that is used to support the propeller shaft in ships. Because of the fact that journal bearings are nonlinear elements, they can have a significant influence on the dynamics of a rotor-bearing system. However, the dynamics of large rotor-bearing systems are generally studied using linear models, where the journal bearings are linearized about an equilibrium position. For a better insight in the dynamics of a nonlinear rotor-bearing system, a nonlinear dynamic analysis needs to be carried out.

In this thesis, compliant short and long plain journal-bearing models for rotordynamic applications are developed. These models consist of spatially discretized nonlinear partial differential equations, which are in fact large systems of nonlinear ordinary differential equations. Because of the dimension of these systems, the standard methods to calculate vibrations of nonlinear dynamic systems are too inefficient. Therefore, also an efficient numerical method to calculated vibrations of partial differential equations is developed.

The nonlinear dynamics of a rotor-bearing system with a rigid rotor in two compliant journal bearings are studied for different values of the relative bearing-liner compliance, using both the short and the long bearing models. It turns out that increasing the relative bearing-liner compliance decreases the stability threshold of a balanced rotor in compliant short journal bearings, while it increases the stability threshold of the same rotor in compliant long journal bearings. For an unbalanced rotor in compliant short journal bearings, the relative bearing-liner compliance has a significant influence on the rotor speeds at which the branch of synchronous vibrations changes stability and on the shape of the branch of subsynchronous vibrations. For the same rotor in compliant long journal bearings, increasing the relative bearing-liner compliance causes an increase in the rotor speed, at which the branch of synchronous vibrations becomes unstable. It appears that in contrast to rigid journal-bearing models the minimum film thickness of the compliant journal-bearing models can become zero and even negative. In other words, the compliant journal-bearing models predict the possibility of contact between the journal and the bearing. Because contact is not included in the models, physically impossible vibrations with negative film thicknesses can be found. For rigid journal-bearing models, contact cannot occur at all because of the fact that either an infinitely large load or an infinitely long time would be needed.

During experiments on a rotor-bearing system with a flexible shaft in a water-lubricated rubber-lined journal bearing, a nonlinear phenomenon is observed. The branch of synchronous vibrations contains two so-called cyclic folds, at which the branch changes its direction. If the rotor speed is varied past one of these cyclic folds, the system jumps to a remote part of the branch of synchronous vibrations. This phenomenon is probably caused by the nonlinear elasticity of the rubber bearing liner of the water-lubricated rubber-lined journal bearing.

Notation

General Notation

a, A	scalar
$\boldsymbol{a}$	(column) vector
$\boldsymbol{A}$	matrix
$a(\cdot)$	function (of one variable)

Operators

$\lvert a\rvert$	absolute value of a
$\boldsymbol{a}^\mathsf{T}$	transpose of $\boldsymbol{a}$
$\boldsymbol{a}^\mathsf{T}\boldsymbol{b}$	inner product of $\boldsymbol{a}$ and $\boldsymbol{b}$
$\boldsymbol{a} \times \boldsymbol{b}$	outer product of $\boldsymbol{a}$ and $\boldsymbol{b}$
$\lVert\boldsymbol{a}\rVert$	$= \sqrt{\boldsymbol{a}^\mathsf{T}\boldsymbol{a}}$, euclidian norm or length of $\boldsymbol{a}$
$\partial a/\partial b$	partial derivative of a with respect to b
$\dot{a}$	total derivative of a with respect to t
a'	total derivative of a with respect to τ

Symbols

$\mathbf{0}$	null vector

α	angle from $\boldsymbol{v}_\mathrm{s}^*$ to $\boldsymbol{\epsilon}$
β_1, β_2	path-following angles
γ	attitude angle
ϵ	small number
	$= \lVert\boldsymbol{\epsilon}\rVert$, nondimensional eccentricity
$\boldsymbol{\epsilon}$	$= \boldsymbol{e}/C$, nondimensional eccentricity vector
θ	angular coordinate
λ	bifurcation parameter
$\mathit{\Lambda}$	$= L/D$, length-diameter ratio
$\mathit{\Delta}\lambda$	correction of λ
μ	lubricant viscosity
ν	Poisson's ratio
σ	path-following step size
τ	$= \mathit{\Omega}_0 t$, nondimensional time
τ_ϕ, τ_z	shear stresses in the ϕ- and z-directions
ϕ	angular coordinate

$\boldsymbol{\phi}_t$	flow
ω	angular forcing frequency
ω_{H}	angular frequency at a primary Hopf bifurcation
ω_{w}	angular whirl frequency
$\boldsymbol{\varPhi}_t$	$= \partial\boldsymbol{\phi}_t/\partial\boldsymbol{u}_0\|_{\boldsymbol{u}_0,\lambda}$, fundamental matrix
$\varOmega$	angular rotor speed
$\varOmega^*$	$= \varOmega/\varOmega_0$, nondimensional angular rotor speed
$\varOmega_0$	$= \varOmega$, for stiffness and damping coefficients
	$= \sqrt{F_0/mC}$, for rotor-bearing system
a	unbalance
a^*	$= a/C$, nondimensional unbalance
b	damping
b^*	$= (C/R)^2 Cb/\mu LD$, nondimensional damping
$\boldsymbol{b}_\lambda$	$= \partial\boldsymbol{f}/\partial\lambda\|_{\boldsymbol{u},\lambda}$
	$= \partial\boldsymbol{\phi}_T/\partial\lambda\|_{\boldsymbol{u}_0,\lambda}$
	$= \partial\boldsymbol{\phi}_{\varDelta t}/\partial\lambda\|_{\boldsymbol{u}_i,\lambda}$
$\boldsymbol{b}_T$	$= \partial\boldsymbol{\phi}_T/\partial T\|_{\boldsymbol{u}_0,\lambda}$
	$= \partial\boldsymbol{\phi}_{\varDelta t}/\partial T\|_{\boldsymbol{u}_i,\lambda}$
B	$= 6\mu\varOmega_0 d(1+\nu)(1-2\nu)/(C/R)^2 CE(1-\nu)$, nondimensional relative bearing-liner compliance
C	radial clearance
d	liner thickness
D	journal diameter
e	eccentricity
$\boldsymbol{e}$	eccentricity vector
E	Young's modulus
$\boldsymbol{f}$	vector field
F	force
F^*	$= (C/R)^2 F/\mu\varOmega_0 LD$, nondimensional force
$\boldsymbol{g}$	Runge-Kutta approximation of $\boldsymbol{f}$
$\boldsymbol{G}$	$= \partial\boldsymbol{\phi}_{\varDelta t}/\partial\boldsymbol{u}_i\|_{\boldsymbol{u}_i,\lambda}$
h	$= H/C$, nondimensional film thickness
H	film thickness
i	index
	imaginary unit
$\boldsymbol{i}$	unit vector
$\boldsymbol{i}_i$	ith column of $\boldsymbol{I}$
I_m^{jk}	$= \int \sin^j\phi\cos^k\phi h^{-m}\,\mathrm{d}\phi$, the journal-bearing integral
$\boldsymbol{I}$	identity matrix
$\boldsymbol{I}_p$	p-dimensional identity matrix
$\boldsymbol{j}_i$	ith column of $\boldsymbol{J}$
$\boldsymbol{J}$	Jacobian matrix
k	path-following point number
	stiffness
k^*	$= (C/R)^2 Ck/\mu\varOmega LD$, nondimensional stiffness
L	bearing length

m	number of time intervals
	mass
$\boldsymbol{m}_i$	ith column of $\boldsymbol{M}$
$\boldsymbol{M}$	$= \boldsymbol{\varPhi}_T$, monodromy matrix
n	system dimension
n_{pf}	maximum number of path-following points
$\boldsymbol{O}$	null matrix
p	pressure
$\bar{p}$	$= \int p \, \mathrm{d}z$, average pressure
p^*	$= (C/R)^2 p / 6\mu\varOmega_0$, nondimensional pressure
$\bar{p}^*$	$= \int p^* \, \mathrm{d}z^*$, nondimensional average pressure
p_λ, p_T, $\boldsymbol{p_u}$	prediction-direction λ-, T-, and $\boldsymbol{u}$-components
r	radial coordinate
$\boldsymbol{r}$	residual vector
R	journal radius
S	$= (C/R)^2 F_{\mathrm{b}} / \mu\varOmega LD$, Sommerfeld number
t	time
$\varDelta t$	$= T/m$, length of time interval
T	period
$\varDelta T$	correction of T
u	$= U/C$, nondimensional bearing-liner deformation
$\boldsymbol{u}$	state vector
$\delta\boldsymbol{u}$	perturbation of $\boldsymbol{u}$
$\varDelta\boldsymbol{u}$	correction of $\boldsymbol{u}$
U	bearing-liner deformation
$\mathcal{U}$	subspace of $\boldsymbol{M}$
$\boldsymbol{v}_{\mathrm{s}}$	$= \dot{\boldsymbol{e}} - (0, 0, \frac{1}{2}\varOmega) \times \boldsymbol{e}$, pure-squeeze velocity vector
v_{s}^*	$= \lVert \boldsymbol{v}_{\mathrm{s}}^* \rVert$, nondimensional pure-squeeze velocity
$\boldsymbol{v}_{\mathrm{s}}^*$	$= \boldsymbol{\epsilon}' - (0, 0, \frac{1}{2}\varOmega^*) \times \boldsymbol{\epsilon}$, nondimensional pure-squeeze velocity vector
W	impedance
x, y, z	coordinate system
z^*	$= z/L$, nondimensional coordinate

Subscripts

0	constant
ϵ, γ	parallel and normal to $\boldsymbol{e}$
ξ, η	parallel and normal to $\boldsymbol{v}_{\mathrm{s}}$
b	bearing
i	at index i
	at $t = i\varDelta t$
p, q	with regard to $\mathcal{U}$ and $\mathcal{U}^\perp$
x, y, z	in the x-, y-, and z-directions

Superscripts

$\perp$	orthogonal complement
(k)	at path-following point k
short, long	with regard to the short and long bearing models

Chapter 1

Introduction

In this chapter, the motivation of the research described in this thesis will be summarized and a brief survey of some literature on journal bearings and rotordynamics will be given. The objectives will be presented and an overview will explain the organization of the rest of the text.

1.1 Motivation

This thesis deals with compliant journal bearings, that is, journal bearings with a relatively elastic bearing liner. These bearings are frequently used and there is a demand from practice for rotordynamic models. Other bearing configurations, in which some kind of compliance is present, such as an elastically supported rigid bearing will not be treated here. For the compliant journal bearings treated in this thesis, the elasticity of the bearing liner is of the same order of magnitude as that of the lubricant film. An example of such a compliant journal bearing is the water-lubricated rubber-lined journal bearing with axial grooves which is used in the stern tube of ships to support the propellor shaft, in dredge cutter heads, and in continuously immersed centrifugal pumps. An advantage of this bearing is the fact that abrasive particles such as sand can easily be rolled over the rubber surface and washed out of the bearing via the axial grooves. In rigid bearings, such particles would cause severe cutting and scoring of the metal bearing components.

Because of the fact that journal bearings are nonlinear elements, they can have a significant influence on the dynamics of an otherwise linear rotor-bearing system. However, the dynamics of large rotor-bearing systems are generally investigated using linear models, where the nonlinearities of the journal bearings are linearized about an equilibrium position. Because of this linearization, these models can only be applied for the analysis of small-amplitude period-1 (or harmonic) solutions (also called synchronous vibrations) about the equilibrium position and for the stability analysis of the equilibrium position (to determine the stability threshold). In order to be able to calculate other possible solutions of a nonlinear rotor-bearing system, such as period-k (or $1/k$ subharmonic) solutions where $k = 2, 3, \dots$ (also called subsynchronous vibrations), quasi-periodic solutions, and chaotic solutions, but also to determine the stability of periodic solutions and to locate bifurcations, a nonlinear dynamic analysis needs to be carried out. Because of the fact that with a nonlinear dynamic analysis more aspects of the dynamics of nonlinear systems can be studied, such an analysis provides a better insight in the behavior of a nonlinear rotor-bearing system than a linear dynamic analysis of the linearized model.

The standard methods to calculate periodic solutions of nonlinear dynamic systems, such as the shooting and finite-difference methods, are developed for relatively small systems of ordinary differential equations. An efficient method to calculate periodic solutions of large nonlinear systems, in which the nonlinearities are local, such as the journal bearings in rotor-bearing systems, uses the so-called component mode synthesis technique (Fey *et al.*, 1996; Fey, 1992). In this method, the local nonlinearities are temporarily removed from the system and the component mode synthesis technique is applied to reduce the number of degrees of freedom of the components of the resulting linear system. Subsequently, the local nonlinearities are replaced and a nonlinear model with a reduced number of degrees of freedom results. The standard methods can then be used to analyze the reduced nonlinear model.

1.2 Literature Survey

In this section, a brief survey of some literature on journal bearings and rotordynamics with regard to the research described in this thesis is given.

Journal Bearings

Reynolds (1886) developed the two-dimensional partial differential equation, known as the Reynolds equation, which governs the pressure in the lubricant film of a journal bearing. For rigid journal bearings, the Reynolds equation is a linear partial differential equation in the lubricant pressure; for compliant journal bearings on the other hand, the Reynolds equation is a nonlinear partial differential equation. This is caused by the fact that, in contrast to rigid bearing, for compliant bearings the film thickness is not known as a function of the eccentricity but is coupled to the pressure by way of the elasticity of the bearing liner.

If an assumption is made about the length of the bearing, the Reynolds equation can be simplified by reducing its dimension to one. The two assumptions that can be made are an (infinitely) short and an (infinitely) long (or perfectly sealed) bearing. For rigid journal bearings, these simplifications cause the Reynolds equation to degenerate into a linear ordinary differential equation, which can be solved analytically; however, for compliant journal bearings, the simplified Reynolds equation remains a nonlinear partial differential equation (but only one-dimensional instead of two-dimensional). This is caused by the fact that the Reynolds equation contains a term with the time derivative of the film thickness. For the calculation of the static properties of compliant journal bearings, the time derivative of the film thickness is set to zero, so that then the simplified Reynolds equation degenerates into a nonlinear ordinary differential equation. Since for compliant journal bearings the Reynolds equation is nonlinear, it cannot be solved analytically.

The short-bearing solution of the Reynolds equation is known as the Ocvirk solution (Ocvirk and DuBois, 1953); the long-bearing solution as the Sommerfeld solution (Sommerfeld, 1904); Moes and Bosma (1981) introduced an analytical approximate finite-length-bearing solution for rigid journal bearings, which is based on the analytical short- and long-bearing solutions. The exact finite-length-bearing solution for rigid bearings can be calculated numerically by discretization of the two-dimensional Reynolds equation with for example finite differences of finite elements.

Booker (1971, 1969, 1965a) introduced the so-called mobility method for dynamically loaded rigid journal bearings and gave analytical expressions for the short, long, and an approximate finite-length bearing. The mobility method is developed for connecting-rod bearings in internal-combustion engines, in which the dynamics of the rotor are negligible and the load on the bearing is known as a function of time. Therefore, in the mobility method the journal velocity is defined as a function of the applied load on the bearing and the journal position, so that this method is unsuitable for rotordynamic applications. Another method for dynamically loaded rigid journal bearings is the so-called impulse method (Blok, 1975). This method is closely related to the mobility method and can also not be applied in rotordynamics. A method for rotordynamic applications of rigid journal bearings is the so-called impedance method (Childs *et al.*, 1977). This method defines the bearing reaction force as a function of the journal position and the journal velocity, so that it can be used as a dynamic model of a journal bearing. Childs *et al.* (1977) demonstrate that impedance vectors can easily be derived from mobility vectors. Therefore, existing mobility descriptions of journal bearings can be converted into impedance descriptions, so that they can indirectly be applied in rotordynamics. Moes and Bosma (1981) published a list of mobility and impedance descriptions for the short, long, and an approximate finite-length bearing.

In the theory of elastohydrodynamic lubrication (Gohar, 1988; Dowson and Higginson, 1977, 1959), elastic deformations of lubricated bearing surfaces are considered. However, this theory is developed for heavily loaded line and point contacts, which can be found in for example gear teeth, cams, and rolling-element bearings, where deformations are relatively small. Compliant journal bearings on the other hand are relatively lightly loaded and their deformations are relatively large (one or two orders of magnitude greater than those occurring in elastohydrodynamic lubrication). Also, as for the mobility method, the load is assumed to be known as a function of time, so that the elastohydrodynamic contact model is unsuitable for rotordynamic applications.

A theoretical study of compliant journal bearings was carried out by Higginson (1966), who calculated static properties of a long plain journal bearing with an elastic bearing liner. The elasticity of the bearing liner is described by an approximate model for a thin liner on a rigid backing. For the sake of simplicity, the same approximation will be used for the compliant journal-bearing models developed in this thesis. Conway and Lee (1975) treated a model similar to that studied by Higginson (1966) but also considered pressure dependence of the lubricant viscosity. In a later paper (Conway and Lee, 1977), they studied the compliant short plain journal bearing. Nilsson (1979) determined the dynamic coefficients of a compliant plain journal bearing and observed the dependence of these coefficients on the angular excitation frequency to angular rotor speed ratio. The stiffness and damping coefficients were calculated for an angular excitation frequency to angular rotor speed ratio of one, which is the value for unbalance excitation.

Several publications (Goenka and Oh, 1986; Fantino and Frene, 1985; LaBouff and Booker, 1985; Oh and Goenka, 1985; van der Tempel *et al.*, 1985) present methods for dynamically loaded compliant journal bearings. However, as for the mobility method for rigid journal bearings, these methods assume the load on the bearing to be known as a function of time, so that they are unsuitable for rotordynamic applications. The rotordynamic model of a compliant short plain journal bearing developed in this thesis was published before (van de Vrande and de Kraker, 1999).

Rotordynamics

Generally, the dynamics of rotor-bearing systems are investigated using a finite-dimensional linear model (Childs, 1993; Ehrich, 1992; Vance, 1988). To obtain such a model, the continuous system is discretized by means of the lumped-parameter, finite-difference, or finite-element method and the stiffness and damping coefficients of the journal bearings are determined by means of linearization about an equilibrium position. Lund (1987) gives a review of the concept of the dynamic coefficients of journal bearings. The resulting linear rotor-bearing model can then be analyzed using standard software packages to calculate critical rotor speeds and stability thresholds.

Fuller (1984) studied the dependence on the bearing stiffness of the critical rotor speeds of a flexible shaft in two bearings, which were modeled as linear springs. In this thesis, a somewhat similar but more complicated investigation is done on a rigid rotor in two compliant journal bearings. Here, the dependence of the nonlinear rotordynamics on the relative compliance of the bearing liner is investigated. For the sake of simplicity, only plain journal bearings are considered, although in practice plain journal bearings are rarely used because of the fact that the stability properties of these bearings are inferior to those of for example multi-lobe and spiral-groove journal bearings. However, the results of the compliant plain journal-bearing models can be considered as a first approximation of compliant journal bearings with more complicated geometries, such as the water-lubricated rubber-lined journal bearing with axial grooves mentioned before.

Different types of rigid journal bearings, which are frequently used in practice, including multi-lobe journal bearings and spiral-groove journal bearings, are listed by Someya (1989). Glienicke and Walter (1980) studied the critical speeds and stability boundaries of shafts in multi-lobe journal bearings. A method for the accurate calculation of spiral-groove bearings was presented by Muijderman (1967). The stability region of a rigid rotor in spiral-groove journal bearings was investigated by Reinhoudt (1972). Muijderman (1986) presented algebraic formulas for the first critical speed and the stability threshold of a flexibly supported rigid rotor in journal bearings considering both the cylindrical and the conical mode of the rotor.

Generally, the study of the dynamics of nonlinear rotor-bearing systems is restricted to the calculation of transients by means of numerical integration. Using the analytical short-bearing model, Kirk and Gunter (1976a,b) carried out transient calculations for both balanced and unbalanced rigid rotors in rigid short plain journal bearings. A systematic approach to analyze nonlinear dynamic systems is by means of the so-called path-following (or pseudo-arclength continuation) method (Fey, 1992; Doedel *et al.*, 1991; Seydel, 1988). A nonlinear dynamic analysis of both balanced and unbalanced flexible rotors in a rigid approximate finite-length plain journal bearing was carried out by van de Vorst *et al.* (1996); van de Vorst (1996). Adiletta *et al.* (1997a,b) analyzed the nonlinear dynamics of an unbalanced rigid rotor in rigid short plain journal bearings both numerically and experimentally.

1.3 Objectives

The first objective of this thesis is to develop compliant plain journal-bearing models for rotordynamic applications. These models can be obtained by extending the classical rigid plain journal-bearing models to journal bearings with an elastic bearing liner. Because of the fact that the compliant plain journal-bearing models consist of spatially discretized nonlinear partial differential equations, which are in fact large systems of nonlinear ordinary differential equations, the standard methods to calculate periodic solutions of nonlinear dynamic systems are too inefficient. Therefore, the second objective is to develop an efficient numerical method to calculate periodic solutions of general spatially discretized nonlinear partial differential equations. This method will be obtained by extending the finite-difference method to partial differential equations using the so-called NPGS approach (Lust, 1997). The method that uses the component mode synthesis technique to reduce the number of degrees of freedom of large nonlinear systems cannot be used for the compliant journal-bearing models because of the fact that the nonlinearity is not local. It is a nonlinearity in the partial differential equation, which becomes global in the large system of ordinary differential equations that follows from the spatial discretization.

1.4 Overview

In chapter 2, a brief introduction to the theory of nonlinear dynamics will be given. In chapter 3, the standard steady-state solvers and the NPGS method will be described, and the finite-difference method will be extended to spatially discretized nonlinear partial differential equations. In chapter 4, the classical rigid plain journal-bearing models will be described and compliant short and long plain journal-bearing models for rotordynamic applications will be developed. Also stiffness and damping coefficients about an equilibrium position will be calculated. Subsequently, in chapter 5 the different journal-bearing models will be applied in a symmetric rotor-bearing system with a rigid rotor in two plain journal bearings. For the rigid plain journal bearings, the influence of the unbalance on the nonlinear dynamics of the rotor will be investigated; for the compliant plain journal bearings, the influence of the relative bearing-liner compliance on the nonlinear dynamics of a balanced and an unbalanced rotor will be studied. A nonlinear phenomenon observed during experiments on a rotor-bearing system with a flexible shaft in a water-lubricated rubber-lined journal bearing will be briefly described. Finally, in chapter 6, the conclusions of this thesis will be drawn and a number of recommendations for further research will be given.

Chapter 2

Nonlinear Dynamics

In this chapter, a brief introduction to the theory of nonlinear dynamics will be given. First, it will be shown that both autonomous dynamic systems and harmonically excited non-autonomous dynamic systems can be put into the so-called autonomous state-space form, which is a set of autonomous nonlinear first-order ordinary differential equations. Because of this, only one numerical solution method needs to be developed for both autonomous and harmonically excited non-autonomous dynamic systems, based on the autonomous state-space form. Subsequently, the known steady-state solutions of an autonomous nonlinear dynamic system will be given and approaches for determining the stability of fixed points and periodic solutions will be presented. Finally, the so-called co-dimension one bifurcations, at which the stability of a branch of steady-state solutions changes qualitatively, will be listed. Generally, these are the only bifurcations that can be encountered if one parameter of the system is varied to follow a branch of steady-state solutions.

2.1 Autonomous State-Space Form

A nonlinear dynamic system is called autonomous if it does not explicitly depend on time. The so-called autonomous state-space form of such a system is given by

$$\dot{\boldsymbol{u}}(t) = \boldsymbol{f}(\boldsymbol{u}(t), \lambda) \tag{2.1}$$

which is an n-dimensional set of autonomous nonlinear first-order ordinary differential equations. In this set of equations, $\boldsymbol{u}(\cdot) \in \mathbb{R}^n$ is the state vector, $\boldsymbol{f}(\cdot, \cdot) \in \mathbb{R}^n$ is the vector field, $\lambda \in \mathbb{R}$ is the parameter of the system that will be varied to follow a branch of steady-state solutions (also called the bifurcation parameter), $t \in \mathbb{R}$ is time, and an overdot denotes the total derivative with respect to t. The set of equations (2.1) combined with the initial condition $\boldsymbol{u}(0) = \boldsymbol{u}_0$ constitutes an initial-value problem. The solution of this initial-value problem is written as $\boldsymbol{\phi}_t(\boldsymbol{u}_0, \lambda)$ and is called the flow.

A nonlinear dynamic system is called non-autonomous if it explicitly depends on time. The state-space form of such a system is given by

$$\dot{\boldsymbol{u}}(t) = \boldsymbol{f}(\boldsymbol{u}(t), t, \lambda)$$

If the explicit time dependence of a non-autonomous system is caused by a harmonical excitation, its state-space form can be rewritten as

$$\dot{\boldsymbol{u}}(t) = \boldsymbol{f}(\boldsymbol{u}(t), \sin(\omega t), \cos(\omega t), \lambda) \tag{2.2}$$

where ω is the angular excitation frequency. This n-dimensional harmonically excited non-autonomous state-space form can be put into an $(n+2)$-dimensional autonomous state-space form by adding the following nonlinear oscillator (Doedel *et al.*, 1998):

$$\begin{cases} \dot{u}_{n+1} = u_{n+1} + \omega u_{n+2} - u_{n+1}(u_{n+1}^2 + u_{n+2}^2) \\ \dot{u}_{n+2} = -\omega u_{n+1} + u_{n+2} - u_{n+2}(u_{n+1}^2 + u_{n+2}^2) \end{cases}$$

The (asymptotically) stable solution of this oscillator is given by

$$\begin{cases} u_{n+1} = \sin(\omega t) \\ u_{n+2} = \cos(\omega t) \end{cases}$$

To eliminate the explicit time dependence of the harmonically excited non-autonomous set of equations (2.2), the $\sin(\omega t)$ and $\cos(\omega t)$ terms are replaced by the extra state variables u_{n+1} and u_{n+2}, respectively.

Because of the fact that both autonomous dynamic systems and harmonically excited non-autonomous dynamic systems can be put into the autonomous state-space form (2.1), only one numerical solution method needs to be developed for both kinds of systems. Therefore, the numerical methods described in the next chapter will all be based on the autonomous state-space form.

An example of a harmonically excited non-autonomous nonlinear dynamic system is the symmetric rotor-bearing system with a rigid rotor that will be studied in chapter 5. Figure 2.1 schematically shows a cross-section of one of the bearings of this rotor-bearing system. The rotor with mass m and unbalance a is supported by two plain journal bearings. In this chapter, the journal bearings are assumed to be rigid and the bearing reaction force components in the x- and y-directions are calculated using the classical short-bearing model, described in chapter 4. The length-diameter ratio of the journal bearings is chosen equal to one. The rotor rotates with a constant angular speed $\mathit{\Omega}$ about the z-axis and a constant load F_0 is applied to the rotor in the negative y-direction. The nondimensional equations of motion of the rotor are given by

$$\begin{cases} \epsilon_x'' = 2F_x^*/F_0^* + \mathit{\Omega}^{*2} a^* \cos(\mathit{\Omega}^* \tau) \\ \epsilon_y'' = 2F_y^*/F_0^* + \mathit{\Omega}^{*2} a^* \sin(\mathit{\Omega}^* \tau) - 1 \end{cases} \tag{2.3}$$

where ϵ_x and ϵ_y are the nondimensional displacements of the rotor in the x- and y-directions, respectively, F_x^* and F_y^* are the nondimensional bearing reaction force components in the x- and y-directions, respectively, τ is nondimensional time and a prime denotes the total derivative with respect to τ. The harmonically excited non-autonomous rotor-bearing system (2.3) can be put into the

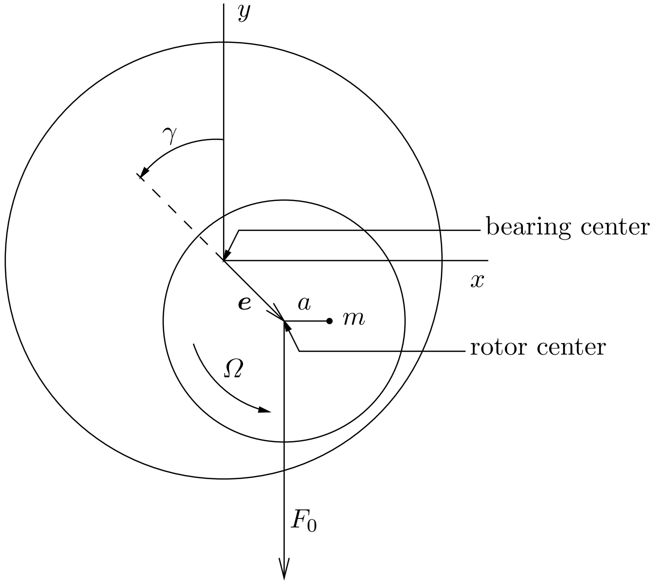

Figure 2.1: Cross-section of one of the bearings of a symmetric rigid rotor in two plain journal bearings

following 6-dimensional autonomous state-space form:

$$\begin{cases} u_1' = u_2 \\ u_2' = 2F_x^*/F_0^* + \Omega^{*2}a^*u_6 \\ u_3' = u_4 \\ u_4' = 2F_y^*/F_0^* + \Omega^{*2}a^*u_5 - 1 \\ u_5' = u_5 + \Omega^*u_6 - u_5(u_5^2 + u_6^2) \\ u_6' = -\Omega^*u_5 + u_6 - u_6(u_5^2 + u_6^2) \end{cases}$$

where $u_1 = \epsilon_x$, $u_2 = \epsilon_x'$, $u_3 = \epsilon_y$, $u_4 = \epsilon_y'$, and u_5 and u_6 are the extra state variables of the nonlinear oscillator. If the rotor is balanced, so that $a^* = 0$, the rotor-bearing system is autonomous and the nonlinear oscillator, given by the last two equations of the autonomous state-space form, can be removed. Therefore, the dimension of the autonomous state-space form of the balanced rotor-bearing system is 4.

2.2 Steady-State Solutions

The four known steady-state solutions of an autonomous nonlinear dynamic system are: the fixed point, the periodic solution, the quasi-periodic solution, and the chaotic solution. In contrast to the steady-state solutions of a linear dynamic system, the steady-state solutions of a nonlinear dynamic system can coexist for certain parameter sets. It is therefore generally impossible to find all the steady-state solutions of a nonlinear dynamic system.

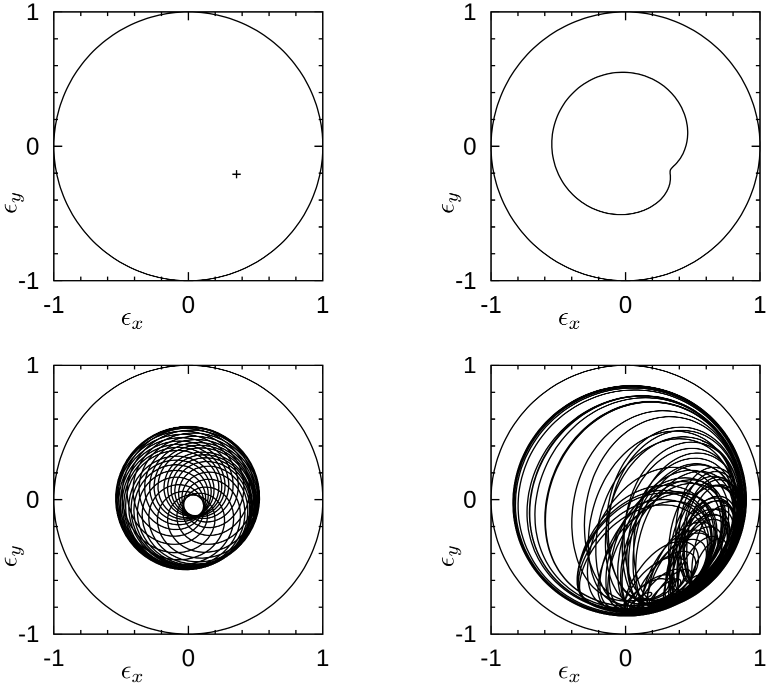

Figure 2.2: Steady-state solutions of a rigid rotor in rigid short plain journal bearings

A fixed point $(\boldsymbol{u}, \lambda)$ is an equilibrium position of the system, in which by definition the time derivative of the state vector is equal to zero ($\dot{\boldsymbol{u}}(t) = \boldsymbol{0}$). Therefore, fixed points can be found by solving the following set of equations, resulting from the substitution of $\dot{\boldsymbol{u}}(t) = \boldsymbol{0}$ into (2.1):

$$\boldsymbol{f}(\boldsymbol{u}, \lambda) = \boldsymbol{0} \tag{2.4}$$

Note that harmonically excited non-autonomous systems do not possess fixed points, so that this set of equations has no solutions. The upper-left panel of figure 2.2 shows a fixed point of the (autonomous) rotor-bearing system for $\Omega^* = 0.5$, $a^* = 0$, and $F_0^* = 1$.

A periodic solution $\boldsymbol{\phi}_t(\boldsymbol{u}_0, \lambda)$ with $t \in [0, T]$ is a solution, in which the system returns to the same state after a certain minimum period $T > 0$. Therefore, periodic solutions can be found by solving the following two-point boundary-value problem:

$$\begin{cases} \dot{\boldsymbol{u}}(t) = \boldsymbol{f}(\boldsymbol{u}(t), \lambda) & t \in [0, T] \\ \boldsymbol{u}(0) = \boldsymbol{u}(T) \end{cases} \tag{2.5}$$

For autonomous dynamic systems, the period of the periodic solution is an unknown, whereas for harmonically excited non-autonomous systems, the period of the periodic solution is an integer multiple of the excitation period: $T = k2\pi/\omega$ ($k = 1, 2, \ldots$). If $k = 1$, the period of the periodic solution is equal to the excitation period and the periodic solution is called a period-1 or harmonic solution;

if $k > 1$, the periodic solution is called a period-k or $1/k$ subharmonic solution. The upper-right panel of figure 2.2 shows a period-2 solution of the rotor-bearing system for $\Omega^* = 6$, $a^* = 0.2$, and $F_0^* = 1$.

A quasi-periodic solution is a solution that possesses two or more incommensurate frequencies, that is, two or more frequencies with irrational ratios. For autonomous systems, these frequencies are unknowns, whereas for harmonically excited non-autonomous systems, one of these frequencies is equal to the excitation frequency and the other frequencies are unknowns. Parker and Chua (1989) describe two methods to calculate so-called 2-periodic solutions (quasi-periodic solutions with two incommensurate frequencies). The lower-left panel of figure 2.2 shows a part of a quasi-periodic solution of the rotor-bearing system for $\Omega^* = 12$, $a^* = 0.3$, and $F_0^* = 1$.

A chaotic solution is a bounded solution which is “none of the above” and the only available method to calculate such a solution is brute-force numerical integration. The lower-right panel of figure 2.2 shows a part of a chaotic solution of the rotor-bearing system for $\Omega^* = 2.646$, $a^* = 0.3$, and $F_0^* = 26.46$ (these parameters are taken from Adiletta *et al.*, 1996).

2.3 Local Stability

The local stability of a fixed point or a periodic solution can be determined by applying an infinitesimally small perturbation to the solution and examining the evolution in time of this perturbation. The fixed point or the periodic solution is (asymptotically) stable if the perturbation converges to zero; it is unstable if the perturbation diverges.

For a fixed point $(\boldsymbol{u}, \lambda)$, the evolution of an initial perturbation $\delta\boldsymbol{u}(0) = \delta\boldsymbol{u}_0$ of $\boldsymbol{u}$ at $t = 0$ is found from the linearization of (2.1):

$$\delta\dot{\boldsymbol{u}}(t) = \boldsymbol{J}(\boldsymbol{u}, \lambda)\delta\boldsymbol{u}(t) \tag{2.6}$$

where $\boldsymbol{J} = \partial\boldsymbol{f}/\partial\boldsymbol{u}$ is the so-called Jacobian matrix. The stability of the fixed point is determined by the eigenvalues of the Jacobian matrix: if all the eigenvalues have negative real parts, the fixed point is (asymptotically) stable; if there is an eigenvalue with a positive real part, the fixed point is unstable.

For a periodic solution $\boldsymbol{\phi}_t(\boldsymbol{u}_0, \lambda)$ with period T, the evolution of a perturbation $\delta\boldsymbol{u}_0$ of $\boldsymbol{u}_0$ is governed by

$$\delta\boldsymbol{u}(t) = \boldsymbol{\Phi}_t\delta\boldsymbol{u}_0 \tag{2.7}$$

where the so-called fundamental matrix $\boldsymbol{\Phi}_t = \partial\boldsymbol{\phi}_t/\partial\boldsymbol{u}_0|_{\boldsymbol{u}_0,\lambda}$ follows from the variational equation

$$\dot{\boldsymbol{\Phi}}_t = \boldsymbol{J}(\boldsymbol{\phi}_t(\boldsymbol{u}_0, \lambda), \lambda)\boldsymbol{\Phi}_t \tag{2.8}$$

with the initial condition $\boldsymbol{\Phi}_0 = \boldsymbol{I}$. The stability of the periodic solution is determined by the eigenvalues of the so-called monodromy matrix $\boldsymbol{M} = \boldsymbol{\Phi}_T$. These eigenvalues are called the Floquet multipliers. One of the Floquet multipliers, called the the trivial Floquet multiplier, is equal to one because of the fact that a perturbation $\delta\boldsymbol{u}_0$ in the direction of the vector field $\boldsymbol{f}(\boldsymbol{u}_0, \lambda)$ neither converges nor diverges. If all the remaining Floquet multipliers have magnitudes less than

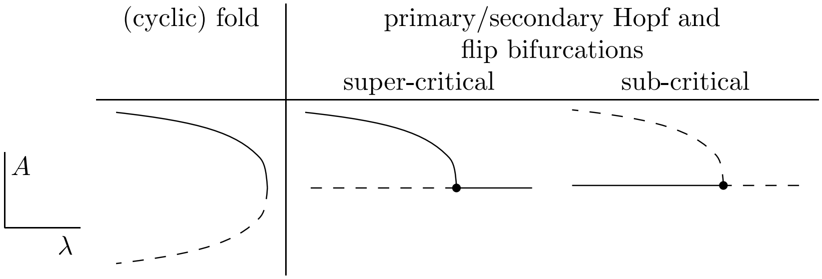

Figure 2.3: Appearance of co-dimension one bifurcations in bifurcation diagram

one, the solution is (asymptotically) stable; if there is a Floquet multiplier with a magnitude greater than one, the solution is unstable.

2.4 Co-dimension One Bifurcations

If one parameter of the system is varied, a branch of steady-state solutions can be followed by means of the path-following method. The (local) stability of a branch of steady-state solutions can change qualitatively at so-called co-dimension one bifurcations. Generally, these are the only bifurcations that can be encountered if one parameter is varied. For fixed points, the co-dimension one bifurcations are: the fold and the primary Hopf bifurcation; for periodic solutions, the co-dimension one bifurcations are: the cyclic fold, the secondary Hopf (or Neimark) bifurcation, and the flip (or period-doubling) bifurcation. From some co-dimension one bifurcations, another branch of steady-state solutions emanates.

Figure 2.3 shows the appearance of the co-dimension one bifurcations in a bifurcation diagram, where a scalar measure A of the solution is plotted against the bifurcation parameter λ. In this figure, solid lines represent branches of stable steady-state solutions, dashed lines represent branches of unstable steady-state solutions, and dots represent bifurcation points. Depending on the bifurcation, the branches contain fixed points or periodic solutions; however, the branch that emanates from the secondary Hopf bifurcation contains quasi-periodic solutions. It is possible that the branches that meet at a co-dimension one bifurcation are all unstable. In that case, the unstable branches that are stable in figure 2.3 have less unstable eigenvalues or Floquet multipliers than the unstable branches that are also unstable in the figure. (A stable/unstable eigenvalue denotes an eigenvalue with a negative/positive real part; a stable/unstable Floquet multiplier denotes a Floquet multiplier with a magnitude less/greater than one.) The different bifurcations depicted in figure 2.3 can also appear horizontally or vertically mirrored.

At one side of a fold, two fixed points coexist, one with one unstable eigenvalue more than the other. At the fold, these fixed points coincide and one eigenvalue is equal to zero. At the other side of the fold, there are (locally) no fixed points.

At one side of a primary Hopf bifurcation, a fixed point and a periodic solution coexist. At the primary Hopf bifurcation, the fixed point and the periodic solution coincide, the fixed point has a pair of complex conjugated eigenvalues with zero real part ($\pm i\omega_{\mathrm{H}}$), and the periodic solution (with amplitude zero) has an angular frequency ω_{H}. At the other side of the primary Hopf bifurcation, there is (locally) no periodic solution and the fixed point gained or lost two stable eigenvalues. If the fixed point gained two stable eigenvalues, the primary Hopf bifurcation is called super-critical; if the fixed point lost two stable eigenvalues, the primary Hopf bifurcation is called sub-critical.

At one side of a cyclic fold, two periodic solutions coexist, one with one unstable Floquet multiplier more than the other. At the cyclic fold, these periodic solutions coincide and, besides the trivial Floquet multiplier, a second Floquet multiplier is equal to one. At the other side of the cyclic fold, there are (locally) no periodic solutions.

At one side of a secondary Hopf bifurcation, a periodic solution and a quasi-periodic solution coexist. At the secondary Hopf bifurcation, the periodic solution and the quasi-periodic solution coincide and the periodic solution has a pair of complex conjugated Floquet multipliers with magnitude one. At the other side of the secondary Hopf bifurcation, there is (locally) no quasi-periodic solution and the periodic solution gained or lost two stable Floquet multipliers. If the periodic solution gained two stable Floquet multipliers, the secondary Hopf bifurcation is called super-critical; if the periodic solution lost two stable Floquet multipliers, the secondary Hopf bifurcation is called sub-critical.

At one side of a flip bifurcation, a period-1 and a period-2 solution coexist. For autonomous systems, the period of the period-2 solution is only approximately equal to twice the period of the period-1 solution. For harmonically excited non-autonomous systems, this equality is exact. At the flip bifurcation, the two periodic solutions coincide and the period-1 solution has a Floquet multiplier equal to -1. At the other side of the flip bifurcation, there is (locally) no period-2 solution and the period-1 solution gained or lost one stable Floquet multiplier. If the period-1 solution gained one stable Floquet multiplier, the flip bifurcation is called super-critical; if the period-1 solution lost one stable Floquet multiplier, the flip bifurcation is called sub-critical.

Chapter 3

Steady-State Solvers and Path-Following

In this chapter, the standard steady-state solvers and the NPGS method will be described. The standard periodic-solution solvers are developed for small systems of nonlinear ordinary differential equations. To investigate the dynamics of the compliant journal-bearing models developed in the next chapter, a method to calculate periodic solutions of nonlinear partial differential equations is needed. An existing numerical method for partial differential equations is the shooting-based NPGS method. Since the shooting method is not as efficient as the finite-difference method, the NPGS approach will be used to extend the finite-difference method to partial differential equations. The path-following method, which is used to follow branches of steady-state solutions by varying one parameter of the system, will be described for the different steady-state solvers. Approaches for locating co-dimension one bifurcations and branch switching to branches emanating from co-dimension one bifurcations will also be given. Finally, the efficiency of the different periodic-solution solvers will be compared.

3.1 Standard Steady-State Solvers

Fixed points can be found by solving (2.4) using the Newton method. For periodic solutions, the two-point boundary-value problem (2.5) needs to be solved, for which several approaches are available. The shooting method uses numerical integration to repeatedly solve an initial-value problem until the periodicity boundary condition is satisfied. Examples of software packages based on the shooting method are CANDYS/QA (Jansen, 1995) and BIFPACK (Seydel, 1999). In the multiple-shooting method, the period is divided into a number of intervals and numerical integration is carried out for the initial-value problems in all the intervals. A software package that implements the multiple-shooting method is MUSN (Ascher *et al.*, 1995). The finite-difference method replaces the time derivative of the state vector by a finite-difference approximation to transform the two-point boundary-value problem into a (large) system of nonlinear algebraic equations, in which the periodicity boundary condition is substituted. The finite element package DIANA (de Witte *et al.*, 2000) offers a nonlinear dynamics module, which includes the shooting, multiple-shooting, and finite-difference methods. The popular software package AUTO 97 (Doedel *et al.*, 1998) uses the adaptive-mesh orthogonal collocation method to calculate periodic solutions of autonomous systems. This method, which resembles the finite-difference method, will not be treated in this thesis.

Fixed Points

For a given parameter λ, a fixed point $\boldsymbol{u}$ of (2.1) can be found by solving (2.4) using the Newton method with an initial guess for $\boldsymbol{u}$, yielding the following linear iteration system in the correction $\Delta\boldsymbol{u}$:

$$\boldsymbol{J}(\boldsymbol{u},\lambda)\Delta\boldsymbol{u} = -\boldsymbol{f}(\boldsymbol{u},\lambda)$$

The columns $\boldsymbol{j}_i(\boldsymbol{u},\lambda)$ $(i = 1,\ldots,n)$ of the Jacobian matrix $\boldsymbol{J}(\boldsymbol{u},\lambda)$ can be approximated by forward differences:

$$\boldsymbol{j}_i(\boldsymbol{u},\lambda) \approx \frac{\boldsymbol{f}(\boldsymbol{u}+\epsilon\boldsymbol{i}_i,\lambda) - \boldsymbol{f}(\boldsymbol{u},\lambda)}{\epsilon}$$

where ϵ is a small number and $\boldsymbol{i}_i$ are the columns of the identity matrix. The approximate solution is updated according to

$$\boldsymbol{u} \leftarrow \boldsymbol{u} + \Delta\boldsymbol{u}$$

The stability of the fixed point can be determined from the Jacobian matrix, which is available as a byproduct of the Newton method.

Shooting Method

A periodic solution of (2.1) can be found by solving the two-point boundary-value problem (2.5). Using the shooting method, the two-point boundary-value problem is reduced to

$$\boldsymbol{r} = \boldsymbol{\phi}_T(\boldsymbol{u}_0,\lambda) - \boldsymbol{u}_0 = \boldsymbol{0} \tag{3.1}$$

where $\boldsymbol{r}$ is the residual and $\boldsymbol{\phi}_T(\boldsymbol{u}_0,\lambda)$ is calculated by solving the initial-value problem (2.1) with the initial condition $\boldsymbol{u}(0) = \boldsymbol{u}_0$ from $t = 0$ to $t = T$ using numerical integration. A solution $(\boldsymbol{u}_0, T)$ of (3.1) is not unique; there are n equations in $n+1$ unknowns (the n components of $\boldsymbol{u}_0$ and T). This is caused by the fact that the phase of a periodic solution of an autonomous system is free; in other words, $\boldsymbol{u}_0$ can be any point on the periodic solution.

For a given parameter λ, a solution of (3.1) can be found using the Newton method with initial guesses for $\boldsymbol{u}_0$ and T, adding a so-called phase condition to fix the phase and, accordingly, make the linear iteration system in the corrections $\Delta\boldsymbol{u}_0$ and ΔT solvable:

$$\begin{pmatrix} \boldsymbol{M}-\boldsymbol{I} & \boldsymbol{b}_T \\ \boldsymbol{f}^{\mathsf{T}}(\boldsymbol{u}_0,\lambda) & 0 \end{pmatrix} \begin{pmatrix} \Delta\boldsymbol{u}_0 \\ \Delta T \end{pmatrix} = -\begin{pmatrix} \boldsymbol{r} \\ 0 \end{pmatrix} \tag{3.2}$$

In this set of equations, $\boldsymbol{M}$ is the monodromy matrix and

$$\boldsymbol{b}_T = \left.\frac{\partial\boldsymbol{\phi}_T}{\partial T}\right|_{\boldsymbol{u}_0,\lambda} = \boldsymbol{f}(\boldsymbol{\phi}_T(\boldsymbol{u}_0,\lambda),\lambda)$$

The columns $\boldsymbol{m}_i$ $(i = 1, \dots, n)$ of $\boldsymbol{M}$ can be approximated by forward differences:

$$\boldsymbol{m}_i \approx \frac{\boldsymbol{\phi}_T(\boldsymbol{u}_0 + \epsilon \boldsymbol{i}_i, \lambda) - \boldsymbol{\phi}_T(\boldsymbol{u}_0, \lambda)}{\epsilon}$$

The phase condition $\boldsymbol{f}^\mathsf{T}(\boldsymbol{u}_0, \lambda)\Delta\boldsymbol{u}_0 = 0$ forces the corrections of the state to be orthogonal to the vector field; in this way, $\boldsymbol{u}_0$ does not move in the "free" direction during the iteration process. The approximate solution is updated according to

$$\begin{cases} \boldsymbol{u}_0 \leftarrow \boldsymbol{u}_0 + \Delta\boldsymbol{u}_0 \\ T \leftarrow T + \Delta T \end{cases}$$

The stability of the periodic solution can be determined from the monodromy matrix, which is available as a byproduct of the shooting method. The free phase of the periodic solution is the cause of the fact that one of the Floquet multipliers (the trivial Floquet multiplier) is equal to one; the associated eigenvector is $\boldsymbol{f}(\boldsymbol{u}_0, \lambda)$.

Multiple-Shooting Method

In the multiple-shooting method, the period is divided into m intervals of equal length and the two-point boundary problem (2.5) is reduced to

$$\begin{cases} \boldsymbol{r}_i = \boldsymbol{\phi}_{\Delta t}(\boldsymbol{u}_i, \lambda) - \boldsymbol{u}_{i+1} = \boldsymbol{0} \qquad i = 0, \dots, m-2 \\ \boldsymbol{r}_{m-1} = \boldsymbol{\phi}_{\Delta t}(\boldsymbol{u}_{m-1}, \lambda) - \boldsymbol{u}_0 = \boldsymbol{0} \end{cases} \tag{3.3}$$

where $\Delta t = T/m$ and $\boldsymbol{\phi}_{\Delta t}(\boldsymbol{u}_i, \lambda)$ is calculated by solving the initial-value problem (2.1) with initial conditions $\boldsymbol{u}(i\Delta t) = \boldsymbol{u}_i$ from $t = i\Delta t$ to $t = (i+1)\Delta t$ using numerical integration.

For a given parameter λ, a solution of (3.3) can be found using the Newton method with initial guesses for $\boldsymbol{u}_i$ $(i = 0, \dots, m-1)$ and T, adding the phase condition to make the linear iteration system in the corrections $\Delta\boldsymbol{u}_i$ and ΔT solvable:

$$\begin{pmatrix} \boldsymbol{G}_0 & -\boldsymbol{I} & & & \boldsymbol{b}_{T,0} \\ & \boldsymbol{G}_1 & -\boldsymbol{I} & & \boldsymbol{b}_{T,1} \\ & & \ddots & \ddots & \vdots \\ -\boldsymbol{I} & & & \boldsymbol{G}_{m-1} & \boldsymbol{b}_{T,m-1} \\ \boldsymbol{f}^\mathsf{T}(\boldsymbol{u}_0, \lambda) & \boldsymbol{0}^\mathsf{T} & \dots & \boldsymbol{0}^\mathsf{T} & 0 \end{pmatrix} \begin{pmatrix} \Delta\boldsymbol{u}_0 \\ \Delta\boldsymbol{u}_1 \\ \vdots \\ \Delta\boldsymbol{u}_{m-1} \\ \Delta T \end{pmatrix} = - \begin{pmatrix} \boldsymbol{r}_0 \\ \boldsymbol{r}_1 \\ \vdots \\ \boldsymbol{r}_{m-1} \\ 0 \end{pmatrix} \tag{3.4}$$

In this set of equations,

$$\boldsymbol{G}_i = \left. \frac{\partial \boldsymbol{\phi}_{\Delta t}}{\partial \boldsymbol{u}_i} \right|_{\boldsymbol{u}_i, \lambda} \quad \text{and} \quad \boldsymbol{b}_{T,i} = \left. \frac{\partial \boldsymbol{\phi}_{\Delta t}}{\partial T} \right|_{\boldsymbol{u}_i, \lambda} = \tfrac{1}{m} \boldsymbol{f}(\boldsymbol{\phi}_{\Delta t}(\boldsymbol{u}_i, \lambda), \lambda)$$

By using the forward recursion

$$\begin{cases} \Delta\boldsymbol{u}_{i+1} = \boldsymbol{G}_i \Delta\boldsymbol{u}_i + \boldsymbol{b}_{T,i}\Delta T + \boldsymbol{r}_i \qquad i = 0, \dots, m-2 \\ \Delta\boldsymbol{u}_0 = \boldsymbol{G}_{m-1}\Delta\boldsymbol{u}_{m-1} + \boldsymbol{b}_{T,m-1}\Delta T + \boldsymbol{r}_{m-1} \end{cases} \tag{3.5}$$

the $(mn+1)$-dimensional system (3.4) is condensed into the same $(n+1)$-dimensional system (3.2) as that of the shooting method, but where

$$\begin{aligned}
\boldsymbol{M} &= \boldsymbol{G}_{m-1}\cdots\boldsymbol{G}_1\boldsymbol{G}_0\\
\boldsymbol{b}_T &= \boldsymbol{b}_{T,m-1} + \boldsymbol{G}_{m-1}\boldsymbol{b}_{T,m-2} + \ldots + \boldsymbol{G}_{m-1}\cdots\boldsymbol{G}_2\boldsymbol{G}_1\boldsymbol{b}_{T,0}\\
\boldsymbol{r} &= \boldsymbol{r}_{m-1} + \boldsymbol{G}_{m-1}\boldsymbol{r}_{m-2} + \ldots + \boldsymbol{G}_{m-1}\cdots\boldsymbol{G}_2\boldsymbol{G}_1\boldsymbol{r}_0
\end{aligned}$$

In each iteration step, first the corrections $\Delta\boldsymbol{u}_0$ and ΔT are calculated from (3.2), after which $\Delta\boldsymbol{u}_i$ $(i=1,\ldots,m-1)$ can be found from (3.5). The approximate solution is updated according to

$$\begin{cases} \boldsymbol{u}_i \leftarrow \boldsymbol{u}_i + \Delta\boldsymbol{u}_i & i = 0,\ldots,m-1\\ T \leftarrow T + \Delta T \end{cases} \tag{3.6}$$

The stability of the periodic solution can be determined from the monodromy matrix, which is available as a byproduct of the multiple-shooting method.

Finite-Difference Method

In the finite-difference method, the period is divided into m intervals of equal length and in the two-point boundary-value problem (2.5) the time derivative of the state vector is replaced by a finite-difference scheme according to

$$\begin{cases} (\boldsymbol{u}_{i+1} - \boldsymbol{u}_i)/\Delta t = \boldsymbol{g}(\boldsymbol{u}_i, \lambda, \Delta t) & i = 0,\ldots,m-2\\ (\boldsymbol{u}_0 - \boldsymbol{u}_{m-1})/\Delta t = \boldsymbol{g}(\boldsymbol{u}_{m-1}, \lambda, \Delta t) \end{cases} \tag{3.7}$$

where the boundary condition has been substituted and $\boldsymbol{g}(\boldsymbol{u}_i, \lambda, \Delta t)$ is an approximation of the average vector field for t between $i\Delta t$ and $(i+1)\Delta t$, as used in an explicit Runge-Kutta integration scheme. For the improved Euler method (which is a second-order Runge-Kutta scheme),

$$\boldsymbol{g}(\boldsymbol{u}_i, \lambda, \Delta t) = \tfrac{1}{2}(\boldsymbol{k}_1 + \boldsymbol{k}_2)$$

where

$$\begin{cases} \boldsymbol{k}_1 = \boldsymbol{f}(\boldsymbol{u}_i, \lambda)\\ \boldsymbol{k}_2 = \boldsymbol{f}(\boldsymbol{u}_i + \Delta t\boldsymbol{k}_1, \lambda) \end{cases}$$

A third-order scheme is given by

$$\boldsymbol{g}(\boldsymbol{u}_i, \lambda, \Delta t) = \tfrac{1}{6}(\boldsymbol{k}_1 + \boldsymbol{k}_2 + 4\boldsymbol{k}_3)$$

where

$$\begin{cases} \boldsymbol{k}_1 = \boldsymbol{f}(\boldsymbol{u}_i, \lambda)\\ \boldsymbol{k}_2 = \boldsymbol{f}(\boldsymbol{u}_i + \Delta t\boldsymbol{k}_1, \lambda)\\ \boldsymbol{k}_3 = \boldsymbol{f}(\boldsymbol{u}_i + \tfrac{1}{4}\Delta t(\boldsymbol{k}_1 + \boldsymbol{k}_2), \lambda) \end{cases}$$

For the classical fourth-order Runge-Kutta scheme,

$$\boldsymbol{g}(\boldsymbol{u}_i, \lambda, \Delta t) = \tfrac{1}{6}(\boldsymbol{k}_1 + 2\boldsymbol{k}_2 + 2\boldsymbol{k}_3 + \boldsymbol{k}_4)$$

where

$$\begin{cases} \boldsymbol{k}_1 = \boldsymbol{f}(\boldsymbol{u}_i, \lambda) \\ \boldsymbol{k}_2 = \boldsymbol{f}(\boldsymbol{u}_i + \frac{1}{2}\Delta t \boldsymbol{k}_1, \lambda) \\ \boldsymbol{k}_3 = \boldsymbol{f}(\boldsymbol{u}_i + \frac{1}{2}\Delta t \boldsymbol{k}_2, \lambda) \\ \boldsymbol{k}_4 = \boldsymbol{f}(\boldsymbol{u}_i + \Delta t \boldsymbol{k}_3, \lambda) \end{cases}$$

Subsequently, (3.7) is rewritten as

$$\begin{cases} \boldsymbol{r}_i = \Delta t \boldsymbol{g}(\boldsymbol{u}_i, \lambda, \Delta t) - \boldsymbol{u}_{i+1} + \boldsymbol{u}_i = \boldsymbol{0} \qquad i = 0, \dots, m-2 \\ \boldsymbol{r}_{m-1} = \Delta t \boldsymbol{g}(\boldsymbol{u}_{m-1}, \lambda, \Delta t) - \boldsymbol{u}_0 + \boldsymbol{u}_{m-1} = \boldsymbol{0} \end{cases} \tag{3.8}$$

For a given parameter λ, a solution of these equations can be found using the Newton method with initial guesses for $\boldsymbol{u}_i$ $(i = 0, \dots, m-1)$ and T, adding the phase condition to make the linear iteration system in the corrections $\Delta \boldsymbol{u}_i$ and ΔT solvable. The resulting iteration system is the same system (3.4) as that of the multiple-shooting method, but where

$$\boldsymbol{G}_i = \Delta t \left. \frac{\partial \boldsymbol{g}}{\partial \boldsymbol{u}_i} \right|_{\boldsymbol{u}_i, \lambda, \Delta t} + \boldsymbol{I} \quad \text{and} \quad \boldsymbol{b}_{T,i} = \frac{1}{m} \left(\boldsymbol{g}(\boldsymbol{u}_i, \lambda, \Delta t) + \Delta t \left. \frac{\partial \boldsymbol{g}}{\partial \Delta t} \right|_{\boldsymbol{u}_i, \lambda, \Delta t} \right)$$

For the improved Euler method,

$$\begin{aligned} \boldsymbol{G}_i &= \tfrac{1}{2}\Delta t \{ \boldsymbol{J}(\boldsymbol{u}_i, \lambda) + \boldsymbol{J}(\boldsymbol{u}_i + \Delta t \boldsymbol{k}_1, \lambda)(\boldsymbol{I} + \Delta t \boldsymbol{J}(\boldsymbol{u}_i, \lambda)) \} + \boldsymbol{I} \\ \boldsymbol{b}_{T,i} &= \tfrac{1}{2m}(\boldsymbol{k}_1 + \boldsymbol{k}_2 + \Delta t \boldsymbol{J}(\boldsymbol{u}_i + \Delta t \boldsymbol{k}_1, \lambda)\boldsymbol{k}_1) \end{aligned}$$

for the third-order scheme,

$$\begin{aligned} \boldsymbol{G}_i = \tfrac{1}{6}\Delta t \{ &\boldsymbol{J}(\boldsymbol{u}_i, \lambda) + \boldsymbol{J}(\boldsymbol{u}_i + \Delta t \boldsymbol{k}_1, \lambda)(\boldsymbol{I} + \Delta t \boldsymbol{J}(\boldsymbol{u}_i, \lambda)) + \\ &4\boldsymbol{J}(\boldsymbol{u}_i + \tfrac{1}{4}\Delta t(\boldsymbol{k}_1 + \boldsymbol{k}_2), \lambda) \\ &(\boldsymbol{I} + \tfrac{1}{4}\Delta t \{ \boldsymbol{J}(\boldsymbol{u}_i, \lambda) + \boldsymbol{J}(\boldsymbol{u}_i + \Delta t \boldsymbol{k}_1, \lambda)(\boldsymbol{I} + \Delta t \boldsymbol{J}(\boldsymbol{u}_i, \lambda)) \}) \} + \boldsymbol{I} \\ \boldsymbol{b}_{T,i} = \tfrac{1}{6m}(&\boldsymbol{k}_1 + \boldsymbol{k}_2 + 4\boldsymbol{k}_3 + \Delta t \{ \boldsymbol{J}(\boldsymbol{u}_i + \Delta t \boldsymbol{k}_1, \lambda)\boldsymbol{k}_1 + \\ &\boldsymbol{J}(\boldsymbol{u}_i + \tfrac{1}{4}\Delta t(\boldsymbol{k}_1 + \boldsymbol{k}_2), \lambda)(\boldsymbol{k}_1 + \boldsymbol{k}_2) \}) \end{aligned}$$

and for the classical fourth-order Runge-Kutta scheme,

$$\begin{aligned} \boldsymbol{G}_i = \tfrac{1}{6}\Delta t \{ &\boldsymbol{J}(\boldsymbol{u}_i, \lambda) + 2\boldsymbol{J}(\boldsymbol{u}_i + \tfrac{1}{2}\Delta t \boldsymbol{k}_1, \lambda)(\boldsymbol{I} + \tfrac{1}{2}\Delta t \boldsymbol{J}(\boldsymbol{u}_i, \lambda)) + \\ &2\boldsymbol{J}(\boldsymbol{u}_i + \tfrac{1}{2}\Delta t \boldsymbol{k}_2, \lambda)\{ \boldsymbol{I} + \tfrac{1}{2}\Delta t \boldsymbol{J}(\boldsymbol{u}_i + \tfrac{1}{2}\Delta t \boldsymbol{k}_1, \lambda)(\boldsymbol{I} + \tfrac{1}{2}\Delta t \boldsymbol{J}(\boldsymbol{u}_i, \lambda)) \} + \\ &\boldsymbol{J}(\boldsymbol{u}_i + \Delta t \boldsymbol{k}_3, \lambda)(\boldsymbol{I} + \Delta t \boldsymbol{J}(\boldsymbol{u}_i + \tfrac{1}{2}\Delta t \boldsymbol{k}_2, \lambda) \\ &\{ \boldsymbol{I} + \tfrac{1}{2}\Delta t \boldsymbol{J}(\boldsymbol{u}_i + \tfrac{1}{2}\Delta t \boldsymbol{k}_1, \lambda)(\boldsymbol{I} + \Delta t \boldsymbol{J}(\boldsymbol{u}_i, \lambda)) \}) \} + \boldsymbol{I} \\ \boldsymbol{b}_{T,i} = \tfrac{1}{6m}\{ &\boldsymbol{k}_1 + 2\boldsymbol{k}_2 + 2\boldsymbol{k}_3 + \boldsymbol{k}_4 + \Delta t(\boldsymbol{J}(\boldsymbol{u}_i + \tfrac{1}{2}\Delta t \boldsymbol{k}_1, \lambda)\boldsymbol{k}_1 + \\ &\boldsymbol{J}(\boldsymbol{u}_i + \tfrac{1}{2}\Delta t \boldsymbol{k}_2, \lambda)\boldsymbol{k}_2 + \boldsymbol{J}(\boldsymbol{u}_i + \Delta t \boldsymbol{k}_3, \lambda)\boldsymbol{k}_3) \} \end{aligned}$$

As a simplification, the following approximations can be used:

$$\begin{cases} \boldsymbol{b}_{T,i} = \frac{1}{m}\boldsymbol{f}(\boldsymbol{u}_{i+1}, \lambda) \qquad i = 0, \dots, m-2 \\ \boldsymbol{b}_{T,m-1} = \frac{1}{m}\boldsymbol{f}(\boldsymbol{u}_0, \lambda) \end{cases}$$

which are inspired by the multiple-shooting method.

Using the forward recursion (3.5), the $(mn+1)$-dimensional iteration system (3.4) is condensed into the same $(n+1)$-dimensional system (3.2) as that of the shooting method. The corrections are found in the same way as in the multiple-shooting method and the approximate solution is updated according to (3.6).

The stability of the periodic solution can be determined from the monodromy matrix, which is available as a byproduct of the finite-difference method because of the choice of the finite-difference scheme.

3.2 NPGS Method

In this section, the shooting-based NPGS (Newton-Picard Gauss-Seidel) method developed by Lust (1997) will be described. This method can efficiently calculate periodic solutions of partial differential equations by exploiting the fact that such solutions have only a small number of Floquet multipliers close to or outside the unit circle. Since the shooting method is not as efficient as the finite-difference method, the NPGS approach will be used to extend the finite-difference method to partial differential equations.

Spatially Discretized Partial Differential Equations

Dynamic systems modeled by nonlinear partial differential equations can be put into the autonomous state-space form (2.1) by spatial discretization with for example finite differences. The standard periodic-solution solvers can then be used to calculate periodic solutions of such systems, but are too inefficient because of the fact that these solvers need the full monodromy matrix for the Newton method. The computation time of the monodromy matrix increases rapidly if the spatial discretization mesh is refined and, accordingly, the system dimension increases.

In spite of the fact that partial differential equations are infinite-dimensional, generally a periodic solution of a partial differential equation has only a few Floquet multipliers close to or outside the unit circle. Moreover, for an accurate discretization, the dynamics of the spatially discretized system must be independent of the mesh. Therefore, refining the mesh will only result in small changes in the Floquet multipliers close to and outside the unit circle and an increase in the number of Floquet multipliers close to zero.

This will be illustrated for the so-called Brusselator (Holodniok *et al.*, 1987), which models a chemical reaction:

$$\begin{cases} \partial u/\partial t = (D_u/L^2)\partial^2 u/\partial x^2 + u^2 v - (B+1)u + A \\ \partial v/\partial t = (D_v/L^2)\partial^2 v/\partial x^2 - u^2 v + Bu \end{cases}$$

The boundary conditions are given by $u(0,t) = u(1,t) = A$ and $v(0,t) = v(1,t) = B/A$. The spatial direction $x \in [0,1]$ is divided into equal intervals of length Δx and the second-order spatial derivatives are approximated by the second-order finite-difference schemes

$$\frac{\partial^2 u}{\partial x^2} \approx \frac{u_{i+1} - 2u_i + u_{i-1}}{\Delta x^2} \quad \text{and} \quad \frac{\partial^2 v}{\partial x^2} \approx \frac{v_{i+1} - 2v_i + v_{i-1}}{\Delta x^2}$$

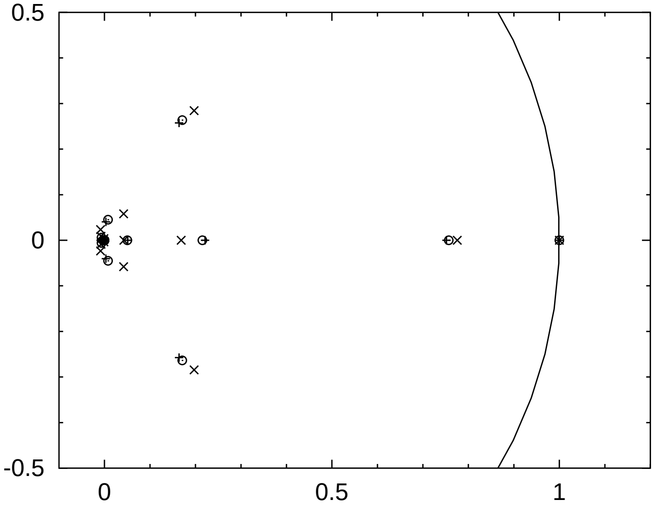

Figure 3.1: Floquet multipliers of a periodic solution of the Brusselator for three different meshes (×: $\Delta x = \frac{1}{8}$, $\odot$: $\Delta x = \frac{1}{16}$, and +: $\Delta x = \frac{1}{32}$)

where u_i and v_i represent u and v at $x = i\Delta x$, respectively. Figure 3.1 shows the complex plane with the Floquet multipliers of a (stable) periodic solution for $A = 2$, $B = 5.45$, $D_u = 0.008$, $D_v = 0.004$, and $L = 1$, using the three different meshes with $\Delta x = \frac{1}{8}$, $\frac{1}{16}$, and $\frac{1}{32}$. As expected, refining the mesh results in small changes in the Floquet multipliers close to the unit circle and an increase in the number of Floquet multipliers close to zero.

Shooting-Based NPGS Method

In the shooting-based NPGS method, the expensive Newton iteration is only carried out in the small subspace spanned by the eigenvectors of the monodromy matrix associated with the Floquet multipliers close to or outside the unit circle. In the orthogonal complement of this subspace, an efficient Picard iteration suffices. Therefore, the full monodromy matrix does not need to be calculated and the computation time can be reduced considerably.

Let the column vectors of the $(n \times p)$-matrix $\boldsymbol{V}_p$ define an orthonormal basis for the subspace $\mathcal{U}$ spanned by the eigenvectors of $\boldsymbol{M}$ associated with the p Floquet multipliers of greatest magnitude. The number p must be chosen such that, of these p Floquet multipliers, the multiplier with least magnitude has a magnitude (much) less than one, so that the Picard iteration converges. In practice, a minimum magnitude of about 0.5 gives satisfactory results. Let the column vectors of the $(n \times (n-p))$-matrix $\boldsymbol{V}_q$ define an orthonormal basis for $\mathcal{U}^\perp$, the orthogonal complement of $\mathcal{U}$.

The orthogonal projectors $\boldsymbol{P}$ and $\boldsymbol{Q}$ onto $\mathcal{U}$ and $\mathcal{U}^\perp$, respectively, are given by

$$\begin{aligned}\boldsymbol{P} &= \boldsymbol{V}_p\boldsymbol{V}_p^\mathsf{T}\\ \boldsymbol{Q} &= \boldsymbol{V}_q\boldsymbol{V}_q^\mathsf{T} = \boldsymbol{I} - \boldsymbol{V}_p\boldsymbol{V}_p^\mathsf{T}\end{aligned}$$

Using these projectors, $\Delta\boldsymbol{u}_0$ can be decomposed according to

$$\Delta\boldsymbol{u}_0 = \boldsymbol{P}\Delta\boldsymbol{u}_0 + \boldsymbol{Q}\Delta\boldsymbol{u}_0 = \boldsymbol{V}_p\Delta\bar{\boldsymbol{p}} + \boldsymbol{V}_q\Delta\bar{\boldsymbol{q}} = \Delta\boldsymbol{p} + \Delta\boldsymbol{q} \tag{3.9}$$

where $\Delta\bar{\boldsymbol{p}}$ and $\Delta\bar{\boldsymbol{q}}$ are p-dimensional and $(n-p)$-dimensional vectors, respectively. Substitution of (3.9) into (3.2) and premultiplication of the first n equations by $[\boldsymbol{Q}^\mathsf{T}\ \boldsymbol{V}_p]^\mathsf{T}$ yields

$$\begin{pmatrix} \boldsymbol{Q}(\boldsymbol{M}-\boldsymbol{I}) & \boldsymbol{O} & \boldsymbol{0} \\ \boldsymbol{V}_p^\mathsf{T}\boldsymbol{M} & \boldsymbol{V}_p^\mathsf{T}\boldsymbol{M}\boldsymbol{V}_p - \boldsymbol{I}_p & \boldsymbol{V}_p^\mathsf{T}\boldsymbol{b}_T \\ \boldsymbol{f}^\mathsf{T}(\boldsymbol{u}_0,\lambda) & \boldsymbol{f}^\mathsf{T}(\boldsymbol{u}_0,\lambda)\boldsymbol{V}_p & 0 \end{pmatrix} \begin{pmatrix} \Delta\boldsymbol{q} \\ \Delta\bar{\boldsymbol{p}} \\ \Delta T \end{pmatrix} = - \begin{pmatrix} \boldsymbol{Q}\boldsymbol{r} \\ \boldsymbol{V}_p^\mathsf{T}\boldsymbol{r} \\ 0 \end{pmatrix} \tag{3.10}$$

where use has been made of the fact that $\boldsymbol{Q}\boldsymbol{M}\boldsymbol{V}_p = \boldsymbol{O}$ because $\mathcal{U}$ is an invariant subspace of $\boldsymbol{M}$, $\boldsymbol{Q}\boldsymbol{V}_p = \boldsymbol{O}$, and $\boldsymbol{V}_p^\mathsf{T}\Delta\boldsymbol{q} = \boldsymbol{0}$. The $(1,3)$-term $\boldsymbol{Q}\boldsymbol{b}_T$ is put equal to zero because of the fact that $\boldsymbol{b}_T$ evaluated at the periodic solution is the eigenvector of $\boldsymbol{M}$ associated with the trivial Floquet multiplier. Therefore, $\boldsymbol{b}_T$ is a vector in the subspace $\mathcal{U}$, so that $\boldsymbol{Q}\boldsymbol{b}_T$ approaches zero as the iteration converges.

Using the fact that $\boldsymbol{Q}\Delta\boldsymbol{q} = \Delta\boldsymbol{q}$, the first n equations of (3.10) can be rewritten as

$$(\boldsymbol{Q}\boldsymbol{M} - \boldsymbol{I})\Delta\boldsymbol{q} = -\boldsymbol{Q}\boldsymbol{r}$$

This set of equations is solved approximately by Picard iteration

$$\Delta\boldsymbol{q} \leftarrow \boldsymbol{Q}\boldsymbol{M}\Delta\boldsymbol{q} + \boldsymbol{Q}\boldsymbol{r}$$

Using the initial guess $\Delta\boldsymbol{q} = \boldsymbol{0}$ and applying only one iteration yields

$$\Delta\boldsymbol{q} = \boldsymbol{Q}\boldsymbol{r} = (\boldsymbol{I} - \boldsymbol{V}_p\boldsymbol{V}_p^\mathsf{T})\boldsymbol{r} \tag{3.11}$$

The corrections $\Delta\bar{\boldsymbol{p}}$ and ΔT can then be solved from

$$\begin{pmatrix} \boldsymbol{V}_p^\mathsf{T}\boldsymbol{M}\boldsymbol{V}_p - \boldsymbol{I}_p & \boldsymbol{V}_p^\mathsf{T}\boldsymbol{b}_T \\ \boldsymbol{f}^\mathsf{T}(\boldsymbol{u}_0,\lambda)\boldsymbol{V}_p & 0 \end{pmatrix} \begin{pmatrix} \Delta\bar{\boldsymbol{p}} \\ \Delta T \end{pmatrix} = - \begin{pmatrix} \boldsymbol{V}_p^\mathsf{T}(\boldsymbol{r} + \boldsymbol{M}\Delta\boldsymbol{q}) \\ \boldsymbol{f}^\mathsf{T}(\boldsymbol{u}_0,\lambda)\Delta\boldsymbol{q} \end{pmatrix} \tag{3.12}$$

and the correction $\Delta\boldsymbol{u}_0$ is given by

$$\Delta\boldsymbol{u}_0 = \boldsymbol{V}_p\Delta\bar{\boldsymbol{p}} + \Delta\boldsymbol{q} \tag{3.13}$$

In the NPGS method, instead of using the monodromy matrix explicitly the basis $\boldsymbol{V}_p$ needs to be determined and only $p+1$ matrix-vector products with $\boldsymbol{M}$ ($\boldsymbol{M}\boldsymbol{V}_p$ and $\boldsymbol{M}\Delta\boldsymbol{q}$) are necessary. The basis $\boldsymbol{V}_p$ is approximated by orthogonal subspace iteration:

1. $\boldsymbol{V}_p \leftarrow \boldsymbol{M}\boldsymbol{V}_p$
2. orthonormalize $\boldsymbol{V}_p$

The matrix-vector products with $\boldsymbol{M}$ are approximated by forward differences:

$$\boldsymbol{M}\boldsymbol{v} \approx \frac{\boldsymbol{\phi}_T(\boldsymbol{u}_0 + \epsilon\boldsymbol{v},\lambda) - \boldsymbol{\phi}_T(\boldsymbol{u}_0,\lambda)}{\epsilon}$$

where ϵ is a small number.

The p Floquet multipliers of greatest magnitude, which determine the stability of the periodic solution, are the eigenvalues of the projected monodromy matrix $\boldsymbol{V}_p^\mathsf{T}\boldsymbol{M}\boldsymbol{V}_p$.

Finite-Difference-Based NPGS Method

Because of the choice of the finite-difference scheme in (3.7) and the forward recursion (3.5), the NPGS approach can be used to extend the finite-difference method to partial differential equations.

The only difference with the shooting-based NPGS method is that in the finite-difference-based NPGS method the matrix-vector product $\boldsymbol{w} = \boldsymbol{M}\boldsymbol{v}$ is given in terms of matrix-vector products with the Jacobian matrix $\boldsymbol{J}$:

$$\begin{cases} \boldsymbol{w} = \boldsymbol{v} & \\ \boldsymbol{w} \leftarrow \boldsymbol{G}_i \boldsymbol{w} & i = 0, \ldots, m-1 \end{cases}$$

where $\boldsymbol{G}_i$ is a function of $\boldsymbol{J}$, which depends on the applied difference scheme (the improved Euler scheme, the third-order scheme, or the classical fourth-order Runge-Kutta scheme). The matrix-vector products with $\boldsymbol{J}$ are approximated by forward differences:

$$\boldsymbol{J}\boldsymbol{w} \approx \frac{\boldsymbol{f}(\boldsymbol{u} + \epsilon \boldsymbol{w}, \lambda) - \boldsymbol{f}(\boldsymbol{u}, \lambda)}{\epsilon}$$

where ϵ is a small number.

3.3 Path-Following

With the path-following (or pseudo-arclength continuation) method (Fey, 1992; Doedel *et al.*, 1991; Seydel, 1988), the bifurcation parameter λ is varied to calculate branches of fixed points or periodic solutions. Starting from a known solution, this method follows a branch of solutions using a predictor-corrector mechanism. The predictor generates an initial guess for the corrector part, in which the Newton method is used to find the next solution on the branch. In the corrector part, the bifurcation parameter λ is considered as an unknown so that the path-following method is able to pass (cyclic) folds. Therefore, an extra equation called a parameterizing equation is needed to make the iteration system solvable.

A predictor can be found by extrapolation from the previous path-following points. An advantage of such a predictor is its short computation time; disadvantages are the start-up problem and the instability of higher-order extrapolating polynomials. A better predictor is found by using the tangent to the branch of steady-state solutions. This predictor can be calculated with little extra cost because of the availability of the Jacobian matrix for fixed points and the monodromy matrix for periodic solutions, respectively.

Fixed Points

In the first path-following step, the predictor direction $(\boldsymbol{p}_{\boldsymbol{u}}, p_\lambda)^{(1)}$ is calculated from

$$\begin{array}{ll} 1. & \boldsymbol{J}^{(1)} \boldsymbol{p}_{\boldsymbol{u}}^{(1)} = -\boldsymbol{b}_\lambda^{(1)} p_\lambda^{(1)} \\ 2. & \text{normalize } (\boldsymbol{p}_{\boldsymbol{u}}, p_\lambda)^{(1)} \end{array} \tag{3.14}$$

where

$$\boldsymbol{b}_\lambda = \left. \frac{\partial \boldsymbol{f}}{\partial \lambda} \right|_{\boldsymbol{u}, \lambda}$$

and the superscript (k) denotes evaluation at path-following point k. Initially, $p_\lambda^{(1)}$ is put equal to 1 if λ must be increased or to -1 if λ must be decreased. If path-following point 1 was calculated using the Newton method, only one extra back-substitution with the decomposition of the Jacobian matrix is needed to solve the linear system in (3.14).

The predictor is calculated from

$$\begin{cases} \boldsymbol{u}^{(k)} = \boldsymbol{u}^{(k-1)} + \sigma \boldsymbol{p}_{\boldsymbol{u}}^{(k-1)} \\ \lambda^{(k)} = \lambda^{(k-1)} + \sigma p_\lambda^{(k-1)} \end{cases}$$

where $k = 2, \ldots, n_{\mathrm{pf}}$ is the number of the path-following point, n_{pf} is the maximum number of path-following points, and σ is the path-following step size.

In the corrector part, (2.4) is solved using the Newton method with the predictor as the initial guess, adding a parameterizing equation to make the linear iteration system in the corrections $\Delta\boldsymbol{u}^{(k)}$ and $\Delta\lambda^{(k)}$ solvable:

$$\begin{pmatrix} \boldsymbol{J}^{(k)} & \boldsymbol{b}_\lambda^{(k)} \\ (\boldsymbol{p}_{\boldsymbol{u}}^{(k-1)})^\mathsf{T} & p_\lambda^{(k-1)} \end{pmatrix} \begin{pmatrix} \Delta\boldsymbol{u}^{(k)} \\ \Delta\lambda^{(k)} \end{pmatrix} = - \begin{pmatrix} \boldsymbol{f}^{(k)} \\ 0 \end{pmatrix} \tag{3.15}$$

The parameterizing equation $(\boldsymbol{p}_{\boldsymbol{u}}^{(k-1)})^\mathsf{T} \Delta\boldsymbol{u}^{(k)} + p_\lambda^{(k-1)} \Delta\lambda^{(k)} = 0$ forces the corrections to be orthogonal to the predictor direction. The approximate solution is updated according to

$$\begin{cases} \boldsymbol{u}^{(k)} \leftarrow \boldsymbol{u}^{(k)} + \Delta\boldsymbol{u}^{(k)} \\ \lambda^{(k)} \leftarrow \lambda^{(k)} + \Delta\lambda^{(k)} \end{cases}$$

In subsequent path-following steps, the predictor direction is calculated from

1. $\begin{pmatrix} \boldsymbol{J}^{(k)} & \boldsymbol{b}_\lambda^{(k)} \\ (\boldsymbol{p}_{\boldsymbol{u}}^{(k-1)})^\mathsf{T} & p_\lambda^{(k-1)} \end{pmatrix} \begin{pmatrix} \boldsymbol{p}_{\boldsymbol{u}}^{(k)} \\ p_\lambda^{(k)} \end{pmatrix} = \begin{pmatrix} \boldsymbol{0} \\ 1 \end{pmatrix}$
2. normalize $(\boldsymbol{p}_{\boldsymbol{u}}, p_\lambda)^{(k)}$

needing only one extra back-substitution with the decomposition of the iteration matrix. By demanding that the projection of the new predictor direction on the previous predictor direction equals 1, the direction of the branch is preserved.

As implemented in AUTO 97 (Doedel *et al.*, 1998), the adaptation of the path-following step size is determined by the convergence history of the corrector. If the number of iterations is equal to 0 or 1, σ is doubled; if it is equal to 2, σ is increased by 50%; if it is equal to 3, σ is increased by 10%; and if it is equal to $4, \ldots, 7$, σ is not changed. Furthermore, the step size is bounded by a user-defined maximum.

If in the corrector part there is no convergence (the number of iterations is more than 7), the norm of the residual $\|\boldsymbol{f}\|$ is not decreasing, or the norm of the corrections $\|(\Delta\boldsymbol{u}, \Delta\lambda)^{(k)}\|$ is not decreasing, the predictor will be discarded and a new predictor will be calculated after halving the step size.

According to Fey (1992), the path-following method may change the direction in which the branch of steady-state solutions is followed if the step size is too large, which often occurs at sharp curves in the branch. This can be avoided by monitoring the angle β_1, between the predictor direction and the line connecting the previous solution with the current approximate solution. The possibility that the path-following method jumps to another branch or to a remote part of the same branch can be diminished by also monitoring the angle β_2, between the projections on the hyperplane perpendicular to the λ-direction of the predictor direction and the line connecting the previous solution with the current approximate solution. If, during the corrector part, β_1 or β_2 becomes greater than a user-defined maximum, the predictor will be discarded and a new predictor will be calculated after halving the path-following step size.

If the step size becomes less than a user-defined minimum, the path-following method fails.

Shooting Method

For the shooting method, the predictor direction $(\boldsymbol{p}_{\boldsymbol{u}_0}, p_T, p_\lambda)^{(1)}$ is calculated from

$$\begin{array}{ll} 1. & \begin{pmatrix} \boldsymbol{M}^{(1)} - \boldsymbol{I} & \boldsymbol{b}_T^{(1)} \\ (\boldsymbol{f}^{(1)})^\mathsf{T} & 0 \end{pmatrix} \begin{pmatrix} \boldsymbol{p}_{\boldsymbol{u}_0}^{(1)} \\ p_T^{(1)} \end{pmatrix} = - \begin{pmatrix} \boldsymbol{b}_\lambda^{(1)} \\ 0 \end{pmatrix} p_\lambda^{(1)} \\ 2. & \text{normalize } (\boldsymbol{p}_{\boldsymbol{u}_0}, p_T, p_\lambda)^{(1)} \end{array} \tag{3.16}$$

where

$$\boldsymbol{b}_\lambda = \left. \frac{\partial \boldsymbol{\phi}_T}{\partial \lambda} \right|_{\boldsymbol{u}_0, \lambda}$$

The predictor is calculated from

$$\begin{cases} \boldsymbol{u}_0^{(k)} = \boldsymbol{u}_0^{(k-1)} + \sigma \boldsymbol{p}_{\boldsymbol{u}_0}^{(k-1)} \\ T^{(k)} = T^{(k-1)} + \sigma p_T^{(k-1)} \\ \lambda^{(k)} = \lambda^{(k-1)} + \sigma p_\lambda^{(k-1)} \end{cases}$$

In the corrector part, (3.1) is solved using the Newton method with the predictor as the initial guess, adding a parameterizing equation to make the linear iteration system in the corrections $\Delta \boldsymbol{u}_0^{(k)}$, $\Delta T^{(k)}$, and $\Delta \lambda^{(k)}$ solvable:

$$\begin{pmatrix} \boldsymbol{M}^{(k)} - \boldsymbol{I} & \boldsymbol{b}_T^{(k)} & \boldsymbol{b}_\lambda^{(k)} \\ (\boldsymbol{f}^{(k)})^\mathsf{T} & 0 & 0 \\ (\boldsymbol{p}_{\boldsymbol{u}_0}^{(k-1)})^\mathsf{T} & p_T^{(k-1)} & p_\lambda^{(k-1)} \end{pmatrix} \begin{pmatrix} \Delta \boldsymbol{u}_0^{(k)} \\ \Delta T^{(k)} \\ \Delta \lambda^{(k)} \end{pmatrix} = - \begin{pmatrix} \boldsymbol{r}^{(k)} \\ 0 \\ 0 \end{pmatrix} \tag{3.17}$$

The parameterizing equation $(\boldsymbol{p}_{\boldsymbol{u}_0}^{(k-1)})^\mathsf{T} \Delta \boldsymbol{u}_0^{(k)} + p_T^{(k-1)} \Delta T^{(k)} + p_\lambda^{(k-1)} \Delta \lambda^{(k)} = 0$ forces the corrections to be orthogonal to the predictor direction. The approximate solution is updated according to

$$\begin{cases} \boldsymbol{u}_0^{(k)} \leftarrow \boldsymbol{u}_0^{(k)} + \Delta \boldsymbol{u}_0^{(k)} \\ T^{(k)} \leftarrow T^{(k)} + \Delta T^{(k)} \\ \lambda^{(k)} \leftarrow \lambda^{(k)} + \Delta \lambda^{(k)} \end{cases}$$

In subsequent path-following steps, the predictor direction is calculated from

$$\begin{array}{ll} 1. & \begin{pmatrix} \boldsymbol{M}^{(k)} - \boldsymbol{I} & \boldsymbol{b}_T^{(k)} & \boldsymbol{b}_\lambda^{(k)} \\ (\boldsymbol{f}^{(k)})^\mathsf{T} & 0 & 0 \\ (\boldsymbol{p}_{\boldsymbol{u}_0}^{(k-1)})^\mathsf{T} & p_T^{(k-1)} & p_\lambda^{(k-1)} \end{pmatrix} \begin{pmatrix} \boldsymbol{p}_{\boldsymbol{u}_0}^{(k)} \\ p_T^{(k)} \\ p_\lambda^{(k)} \end{pmatrix} = \begin{pmatrix} \boldsymbol{0} \\ 0 \\ 1 \end{pmatrix} \\ 2. & \text{normalize } (\boldsymbol{p}_{\boldsymbol{u}_0}, p_T, p_\lambda)^{(k)} \end{array}$$

needing only one extra back-substitution with the decomposition of the iteration matrix.

Multiple-Shooting and Finite-Difference Methods

For the multiple-shooting and finite-difference methods, the predictor direction $(\boldsymbol{p}_{\boldsymbol{u}_0}, \boldsymbol{p}_{\boldsymbol{u}_1}, \dots, \boldsymbol{p}_{\boldsymbol{u}_{m-1}}, p_T, p_\lambda)^{(1)}$ is calculated from

$$\begin{array}{ll} 1. & \begin{pmatrix} \boldsymbol{M}^{(1)} - \boldsymbol{I} & \boldsymbol{b}_T^{(1)} \\ (\boldsymbol{f}^{(1)})^\mathsf{T} & 0 \end{pmatrix} \begin{pmatrix} \boldsymbol{p}_{\boldsymbol{u}_0}^{(1)} \\ p_T^{(1)} \end{pmatrix} = -\begin{pmatrix} \boldsymbol{b}_\lambda^{(1)} \\ 0 \end{pmatrix} p_\lambda^{(1)} \\ 2. & \boldsymbol{p}_{\boldsymbol{u}_{i+1}}^{(1)} = \boldsymbol{G}_i^{(1)} \boldsymbol{p}_{\boldsymbol{u}_i}^{(1)} + \boldsymbol{b}_{T,i}^{(1)} p_T^{(1)} + \boldsymbol{r}_i^{(1)} \qquad i = 0, \dots, m-2 \\ 3. & \text{normalize } (\boldsymbol{p}_{\boldsymbol{u}_0}, \boldsymbol{p}_{\boldsymbol{u}_1}, \dots, \boldsymbol{p}_{\boldsymbol{u}_{m-1}}, p_T, p_\lambda)^{(1)} \end{array} \tag{3.18}$$

where

$$\boldsymbol{b}_\lambda = \boldsymbol{b}_{\lambda,m-1} + \boldsymbol{G}_{m-1} \boldsymbol{b}_{\lambda,m-2} + \ldots + \boldsymbol{G}_{m-1} \cdots \boldsymbol{G}_2 \boldsymbol{G}_1 \boldsymbol{b}_{\lambda,0}$$

and

$$\boldsymbol{b}_{\lambda,i} = \left. \frac{\partial \boldsymbol{\phi}_{\Delta t}}{\partial \lambda} \right|_{\boldsymbol{u}_i, \lambda} \quad \text{or} \quad \boldsymbol{b}_{\lambda,i} = \Delta t \left. \frac{\partial \boldsymbol{g}}{\partial \lambda} \right|_{\boldsymbol{u}_i, \lambda, \Delta t}$$

for the multiple-shooting or finite-difference methods, respectively.

The predictor is calculated from

$$\begin{cases} \boldsymbol{u}_i^{(k)} = \boldsymbol{u}_i^{(k-1)} + \sigma \boldsymbol{p}_{\boldsymbol{u}_i}^{(k-1)} & i = 0, \dots, m-1 \\ T^{(k)} = T^{(k-1)} + \sigma p_T^{(k-1)} \\ \lambda^{(k)} = \lambda^{(k-1)} + \sigma p_\lambda^{(k-1)} \end{cases}$$

In the corrector part, (3.3) and (3.8) are solved using the Newton method with the predictor as the initial guess, adding a parameterizing equation to make the linear iteration system in the corrections $\Delta \boldsymbol{u}_i^{(k)}$ $(i = 0, \dots, m-1)$, $\Delta T^{(k)}$, and $\Delta \lambda^{(k)}$ solvable:

$$\begin{pmatrix} \boldsymbol{G}_0^{(k)} & -\boldsymbol{I} & & & \boldsymbol{b}_{T,0}^{(k)} & \boldsymbol{b}_{\lambda,0}^{(k)} \\ & \boldsymbol{G}_1^{(k)} & -\boldsymbol{I} & & \boldsymbol{b}_{T,1}^{(k)} & \boldsymbol{b}_{\lambda,1}^{(k)} \\ & & \ddots & \ddots & \vdots & \vdots \\ -\boldsymbol{I} & & & \boldsymbol{G}_{m-1}^{(k)} & \boldsymbol{b}_{T,m-1}^{(k)} & \boldsymbol{b}_{\lambda,m-1}^{(k)} \\ (\boldsymbol{f}^{(k)})^\mathsf{T} & \boldsymbol{0}^\mathsf{T} & \dots & \boldsymbol{0}^\mathsf{T} & 0 & 0 \\ (\boldsymbol{p}_{\boldsymbol{u}_0}^{(k-1)})^\mathsf{T} & \boldsymbol{0}^\mathsf{T} & \dots & \boldsymbol{0}^\mathsf{T} & p_T^{(k-1)} & p_\lambda^{(k-1)} \end{pmatrix} \begin{pmatrix} \Delta \boldsymbol{u}_0^{(k)} \\ \Delta \boldsymbol{u}_1^{(k)} \\ \vdots \\ \Delta \boldsymbol{u}_{m-1}^{(k)} \\ \Delta T^{(k)} \\ \Delta \lambda^{(k)} \end{pmatrix} = \\ - \left(\boldsymbol{r}_0^{(k)}, \boldsymbol{r}_1^{(k)}, \dots, \boldsymbol{r}_{m-1}^{(k)}, 0, 0 \right)$$

The parameterizing equation $(\boldsymbol{p}_{\boldsymbol{u}_0}^{(k-1)})^{\mathsf{T}} \Delta \boldsymbol{u}_0^{(k)} + p_T^{(k-1)} \Delta T^{(k)} + p_\lambda^{(k-1)} \Delta\lambda^{(k)} = 0$ forces a part of the corrections to be orthogonal to the predictor direction. The approximate solution is updated according to

$$\begin{cases} \boldsymbol{u}_i^{(k)} \leftarrow \boldsymbol{u}_i^{(k)} + \Delta \boldsymbol{u}_i^{(k)} & i = 0, \ldots, m-1 \\ T^{(k)} \leftarrow T^{(k)} + \Delta T^{(k)} & \\ \lambda^{(k)} \leftarrow \lambda^{(k)} + \Delta\lambda^{(k)} & \end{cases}$$

In subsequent path-following steps, the predictor direction is calculated from

1. $$\begin{pmatrix} \boldsymbol{G}_0^{(k)} & -\boldsymbol{I} & & & \boldsymbol{b}_{T,0}^{(k)} & \boldsymbol{b}_{\lambda,0}^{(k)} \\ & \boldsymbol{G}_1^{(k)} & -\boldsymbol{I} & & \boldsymbol{b}_{T,1}^{(k)} & \boldsymbol{b}_{\lambda,1}^{(k)} \\ & & \ddots & \ddots & \vdots & \vdots \\ -\boldsymbol{I} & & & \boldsymbol{G}_{m-1}^{(k)} & \boldsymbol{b}_{T,m-1}^{(k)} & \boldsymbol{b}_{\lambda,m-1}^{(k)} \\ (\boldsymbol{f}^{(k)})^{\mathsf{T}} & \boldsymbol{0}^{\mathsf{T}} & \ldots & \boldsymbol{0}^{\mathsf{T}} & 0 & 0 \\ (\boldsymbol{p}_{\boldsymbol{u}_0}^{(k-1)})^{\mathsf{T}} & \boldsymbol{0}^{\mathsf{T}} & \ldots & \boldsymbol{0}^{\mathsf{T}} & p_T^{(k-1)} & p_\lambda^{(k-1)} \end{pmatrix} \begin{pmatrix} \boldsymbol{p}_{\boldsymbol{u}_0}^{(k)} \\ \boldsymbol{p}_{\boldsymbol{u}_1}^{(k)} \\ \vdots \\ \boldsymbol{p}_{\boldsymbol{u}_{m-1}}^{(k)} \\ p_T^{(k)} \\ p_\lambda^{(k)} \end{pmatrix} = \\ (\boldsymbol{0}, \boldsymbol{0}, \ldots, \boldsymbol{0}, 0, 1)$$
2. normalize $(\boldsymbol{p}_{\boldsymbol{u}_0}, \boldsymbol{p}_{\boldsymbol{u}_1}, \ldots, \boldsymbol{p}_{\boldsymbol{u}_{m-1}}, p_T, p_\lambda)^{(k)}$

needing only one extra back-substitution with the decomposition of the iteration matrix.

3.4 Locating Bifurcations and Branch-Switching

During path-following, bifurcations can be encountered. Generally, these can only be co-dimension one bifurcations. Methods for locating such bifurcations can be divided into two classes: direct methods and indirect methods. The direct methods add one or more equations expressing the conditions for a bifurcation to the two-point boundary-value problem. The extended system of equations is then solved to locate the bifurcation. The methods described in this section belong to the class of indirect methods, in which a zero of a scalar test function is calculated to locate the bifurcation. The advantage of the indirect methods is that the standard path-following method can be used because of the fact that no equations are added to the two-point boundary-value problem. If during path-following a bifurcation is passed, the number of unstable eigenvalues or Floquet multipliers changes. By monitoring this number, the zero of the test function can be bracketed, and the false position method can be used to find the zero as a function of the path-following step size. For each co-dimension one bifurcation, a separate test function needs to be defined.

After a co-dimension one bifurcation has been found, branch-switching can be used to switch the direction of the path-following method and to calculate the branch of steady-state solutions that emanates from the bifurcation.

Branches of Fixed-Points

At a fold, the tangent to the branch of steady-state solutions is vertical, so that the predictor-direction parameter-component p_λ is equal to zero. Therefore, this component is used as the fold test function. The number of unstable eigenvalues changes by one if a fold is passed.

A primary Hopf bifurcation is characterized by a pair of complex conjugated eigenvalues with zero real part ($\pm i\omega_{\mathrm{H}}$). Therefore, the value of the real part of the pair of complex conjugated eigenvalues that crosses the imaginary axis is used as the primary Hopf bifurcation test function. The number of unstable eigenvalues changes by two if a primary Hopf bifurcation is passed.

The branch of periodic solutions that emanates from the primary Hopf bifurcation can be found by branch-switching: a predictor direction for this branch is determined and the path-following method for periodic solutions is started from the primary Hopf bifurcation.

The following is a slight modification of the method to determine a predictor direction by Jansen (1995). At a primary Hopf bifurcation, the matrix $\boldsymbol{J}^2+\omega_{\mathrm{H}}^2\boldsymbol{I}$ has a double zero eigenvalue. If $\boldsymbol{v}+i\boldsymbol{w}$ is the eigenvector of $\boldsymbol{J}$ associated with the eigenvalue $i\omega_{\mathrm{H}}$, then $\boldsymbol{v}$ and $\boldsymbol{J}\boldsymbol{v}$ span the eigenspace of $\boldsymbol{J}^2+\omega_{\mathrm{H}}^2\boldsymbol{I}$ associated with the zero eigenvalue. The vector $\boldsymbol{v}$ can be found from

$$\begin{pmatrix} \boldsymbol{J}^2+\omega_{\mathrm{H}}^2\boldsymbol{I} & \boldsymbol{w}_1 & \boldsymbol{w}_2 \\ \boldsymbol{w}_1^{\mathsf{T}} & 0 & 0 \\ \boldsymbol{w}_2^{\mathsf{T}} & 0 & 0 \end{pmatrix} \begin{pmatrix} \boldsymbol{v} \\ \phi_1 \\ \phi_2 \end{pmatrix} = \begin{pmatrix} \boldsymbol{0} \\ 1 \\ 1 \end{pmatrix}$$

where $\boldsymbol{w}_1$ and $\boldsymbol{w}_2$ are random vectors and the solution must have $\phi_1=\phi_2=0$. The eigenvector is normalized according to $\boldsymbol{v}\leftarrow\boldsymbol{v}/\|\boldsymbol{v}\|$.

The periodic solution at the primary Hopf bifurcation coincides with the fixed point and its period $T=2\pi/\omega_{\mathrm{H}}$. For the shooting method, the predictor direction is given by $(\boldsymbol{p}_{\boldsymbol{u}_0}, p_T, p_\lambda)^{(1)}=(\boldsymbol{v},0,0)$. For the multiple-shooting and finite-difference methods, the predictor direction is calculated from

1. $$\begin{cases} \boldsymbol{p}_{\boldsymbol{u}_i}^{(1)} = \boldsymbol{v}\cos(2\pi i/m)+(\boldsymbol{J}\boldsymbol{v}/\|\boldsymbol{J}\boldsymbol{v}\|)\sin(2\pi i/m) \qquad i=0,\ldots,m-1 \\ p_T^{(1)} = 0 \\ p_\lambda^{(1)} = 0 \end{cases}$$
2. normalize $(\boldsymbol{p}_{\boldsymbol{u}_0}, \boldsymbol{p}_{\boldsymbol{u}_1}, \ldots, \boldsymbol{p}_{\boldsymbol{u}_{m-1}}, p_T, p_\lambda)^{(1)}$

Branches of Periodic-Solutions

Similar to the fold for branches of fixed-points, the predictor-direction parameter-component p_λ is used as the cyclic fold test function. The number of unstable Floquet multipliers changes by one if a cyclic fold is passed.

A secondary Hopf bifurcation is characterized by a pair of complex conjugated Floquet multipliers on the unit circle. Therefore, the difference between the magnitude of the Floquet multiplier with positive imaginary part that crosses the unit circle and one is used as the secondary Hopf bifurcation test function. The number of unstable Floquet multipliers changes by two if a secondary Hopf bifurcation is passed.

At a flip bifurcation, one of the Floquet multiplier crosses the unit circle at -1. The flip bifurcation test function that is generally used is given by $\det(\boldsymbol{M}+\boldsymbol{I})$ and can be easily computed by adding one to all the Floquet multipliers and calculating the product of these values.

To determine a predictor direction for the branch of double-period solutions emanating from the flip bifurcation, the eigenvector $\boldsymbol{v}$ associated with the eigenvalue -1 is needed. This eigenvector can be calculated from

$$\begin{pmatrix} \boldsymbol{M}+\boldsymbol{I} & \boldsymbol{w} \\ \boldsymbol{w}^{\mathsf{T}} & 0 \end{pmatrix} \begin{pmatrix} \boldsymbol{v} \\ \phi \end{pmatrix} = \begin{pmatrix} \boldsymbol{0} \\ 1 \end{pmatrix}$$

where $\boldsymbol{w}$ is a random vector and the solution must have $\phi = 0$. The eigenvector is normalized according to $\boldsymbol{v} \leftarrow \boldsymbol{v}/\|\boldsymbol{v}\|$.

At the flip bifurcation, the double-period solution coincides with the single-period solution and has a period that is equal to twice the period of the single-period solution. For the shooting method, the predictor direction is given by $(\boldsymbol{p}_{\boldsymbol{u}_0}, p_T, p_\lambda)^{(1)} = (\boldsymbol{v}, 0, 0)$. For the multiple-shooting and finite-difference methods, the predictor direction is calculated from

1. $\begin{cases} \boldsymbol{p}_{\boldsymbol{u}_i}^{(1)} = \boldsymbol{v}\cos(2\pi i/m) \qquad i = 0, \ldots, m-1 \\ p_T^{(1)} = 0 \\ p_\lambda^{(1)} = 0 \end{cases}$
2. normalize $(\boldsymbol{p}_{\boldsymbol{u}_0}, \boldsymbol{p}_{\boldsymbol{u}_1}, \ldots, \boldsymbol{p}_{\boldsymbol{u}_{m-1}}, p_T, p_\lambda)^{(1)}$

3.5 Comparison of Periodic-Solution Solvers

In this section, the efficiency of the different periodic-solution solvers is compared by carrying out a so-called homotopy calculation. In such a calculation, the path-following method is started from a known solution and continued until the bifurcation parameter reaches a desired value.

The calculations will be carried out on the symmetric rotor-bearing system with a rigid rotor schematically depicted in figure 2.1 of the previous chapter, using the compliant short journal-bearing model of the next chapter to calculate the bearing reaction force components in the x- and y-directions. The compliant short journal-bearing model adds a nonlinear partial differential equation to the equations of motion of the rotor. This partial differential equation is spatially discretized using finite differences, dividing the circumferential direction into 50 intervals of equal length. The resulting autonomous state-space form of the rotor-bearing system has a dimension of 56 and is given by

$$\begin{cases} u_1' = u_2 \\ u_2' = 2F_x^*/F_0^* + \mathit{\Omega}^{*2} a^* u_{56} \\ u_3' = u_4 \\ u_4' = 2F_y^*/F_0^* + \mathit{\Omega}^{*2} a^* u_{55} \\ \dfrac{\partial h}{\partial \tau} = -\frac{1}{2}\left(\dfrac{3h^3 \bar{p}^*}{(L/D)^2} + \mathit{\Omega}^* \dfrac{\partial h}{\partial \theta}\right) \\ u_{55}' = u_{55} + \mathit{\Omega}^* u_{56} - u_{55}(u_{55}^2 + u_{56}^2) \\ u_{56}' = -\mathit{\Omega}^* u_{55} + u_{56} - u_{56}(u_{55}^2 + u_{56}^2) \end{cases}$$

where $u_1 = \epsilon_x$, $u_2 = \epsilon_x'$, $u_3 = \epsilon_y$, $u_4 = \epsilon_y'$, $\bar{p}^* = (h - 1 - \epsilon_x \sin\theta + \epsilon_y \cos\theta)/B$ and u_{55} and u_{56} are the extra state variables of the nonlinear oscillator. The spatial

	Total time [s]	Number of pf-points	Time per pf-point [s]
Shooting	319.	4	79.8
Finite-difference	158.	4	39.5
Shooting-based NPGS	85.7	4	21.4
Finite-difference-based NPGS	16.3	4	4.08

Table 3.1: Results of the different path-following methods

discretization of the partial differential equation will yield the expressions for u_5 to u_{54}. Note that the term -1 in the fourth equation, which results from the constant load F_0, is put equal to zero to be able to start from a known solution. By means of another homotopy calculation with an extra parameter, this term can be decreased to -1 again.

Here, the nondimensional unbalance a^* is used as the homotopy parameter. For $a^* = 0$, the known fixed point of the rotor-bearing system is given by $(u_1, u_2, u_3, u_4, h, u_{55}, u_{56}) = (0, 0, 0, 0, 1, \sin(\Omega^* \tau), \cos(\Omega^* \tau))$. Using the different path-following methods for periodic solutions, the nondimensional unbalance is increased from 0 to 0.2.

The results of the shooting method, the finite-difference method, the shooting-based NPGS method, and the finite-difference-based NPGS method are given in table 3.1. For the homotopy calculation of the rotor-bearing system, the shooting-based NPGS method turns out to be almost four times faster than the shooting method. The finite-difference-based NPGS method is even almost ten times faster than the finite-difference method. Because of the fact that the finite-difference method is already about two times more efficient than the shooting method, the finite-difference-based NPGS method turns out to be more than five times faster than the shooting-based NPGS method. However, the finite-difference-based NPGS method has the same disadvantages as the standard finite-difference method, such as numerical instability for stiff systems and inaccuracy for complicated periodic solutions containing higher harmonics. The rotor-bearing systems dealt with in this thesis appear to be not stiff and their periodic solutions to be relatively simple.

Chapter 4

Journal-Bearing Models

In this chapter, compliant journal-bearing models for rotordynamic applications will be developed. First, the classical analytical rigid short (Ocvirk and DuBois, 1953) and long (Sommerfeld, 1904) journal-bearing models, on which the compliant bearing models are based, will be described. In this description, new exact results will be presented for the rigid long bearing. Also an analytical approximate finite-length model from literature and a numerical exact finite-length model for the rigid journal bearing will be treated. Subsequently, new compliant short and long plain journal-bearing models will be developed.

4.1 Rigid Journal-Bearing Models

Figure 4.1 schematically shows the geometry of a rigid plain journal bearing. The origin of the the stationary x, y, z-coordinate system is located at the center of the bearing. The angular coordinate ϕ is measured from the maximum film thickness. The journal with radius R rotates with a constant angular speed $\mathit{\Omega}$ about the z-axis. The position of its center is given by the eccentricity vector $\boldsymbol{e}$ with attitude angle γ. The radial clearance is given by C and the film thickness by H. The film thickness can be found using the cosine rule of triangles:

$$(R+H)^2 = (R+C)^2 + e^2 + 2(R+C)e\cos\phi$$

where $e = \|\boldsymbol{e}\|$. Expanding this equation, dividing by R^2, and discarding second-order terms in H/R, C/R, and e/R yields

$$H = C + e\cos\phi$$

With the nondimensional quantities $h = H/C$ and $\boldsymbol{\epsilon} = \boldsymbol{e}/C$, this equation can be rewritten as

$$h = 1 + \epsilon\cos\phi \tag{4.1}$$

where $\epsilon = \|\boldsymbol{\epsilon}\|$.

The pressure p in the lubricant film of a journal bearing is governed by the Reynolds equation (see appendix A), given by

$$\frac{1}{R^2}\frac{\partial}{\partial\phi}\left(H^3\frac{\partial p}{\partial\phi}\right) + H^3\frac{\partial^2 p}{\partial z^2} = 6\mu\left(\mathit{\Omega}\frac{\partial H}{\partial\phi} + 2\frac{\partial H}{\partial t}\right)$$

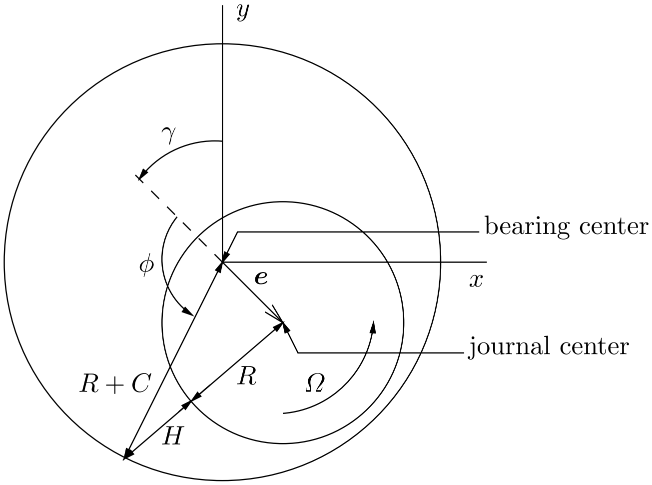

Figure 4.1: Geometry of a rigid plain journal bearing

where μ is the lubricant viscosity. For rigid journal bearings, the Reynolds equation is a linear partial differential equation in p. With the nondimensional quantities $\Omega^* = \Omega/\Omega_0$ (Ω_0 is a constant angular frequency which will be defined in the next chapter, $p^* = (C/R)^2 p/6\mu\Omega_0$, $z^* = z/L$ (L is the bearing length), and $\tau = \Omega_0 t$, the Reynolds equation becomes

$$\frac{\partial}{\partial\phi}\left(h^3\frac{\partial p^*}{\partial\phi}\right) + \frac{h^3}{4(L/D)^2}\frac{\partial^2 p^*}{\partial z^{*2}} = \Omega^*\frac{\partial h}{\partial\phi} + 2\frac{\partial h}{\partial\tau} \tag{4.2}$$

where D is the journal diameter. In literature, Ω is normally applied to scale the equations; in this thesis, Ω_0 is taken for that purpose because of the fact that Ω (actually Ω^*) will be used as the bifurcation parameter. The boundary conditions for p^* are periodicity with respect to ϕ, symmetry at $z^* = 0$, and $p^* = 0$ at $z^* = -\frac{1}{2}$ and at $z^* = \frac{1}{2}$. To model cavitation, negative values of the pressure are put equal to zero. Although this approach causes discontinuities in the flow of the lubricant, it is easy to implement as compared to the more realistic approach in which continuity is imposed at the boundaries of the (unknown) cavitation area. With the latter approach, the nondimensional pressure p^* cannot be solved directly from the Reynolds equation (4.2) because of the fact that the cavitation area needs to be found by iteration.

After substitution of (4.1), the right-hand side of (4.2) becomes

$$2\{\epsilon'\cos\phi + \epsilon(\gamma' - \tfrac{1}{2}\Omega^*)\sin\phi\} \tag{4.3}$$

where a prime denotes the total derivative with respect to τ. This expression can be restated as

$$2v_{\mathrm{s}}^*\cos(\alpha + \phi) \tag{4.4}$$

(Childs *et al.*, 1977), where $v_{\mathrm{s}}^* = \|\boldsymbol{v}_{\mathrm{s}}^*\|$ and $\boldsymbol{v}_{\mathrm{s}}^* = \boldsymbol{v}_{\mathrm{s}}/C\Omega_0$. To see this, the so-called pure-squeeze velocity vector $\boldsymbol{v}_{\mathrm{s}}$ is introduced and defined by the journal

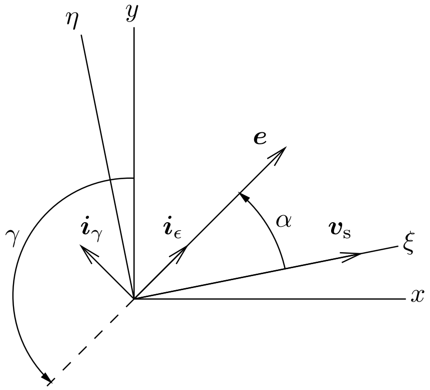

Figure 4.2: Angle between the pure-squeeze velocity vector and the eccentricity vector

velocity relative to a coordinate system rotating with an angular speed of $\frac{1}{2}\mathit{\Omega}$ about the z-axis:

$$\boldsymbol{v}_\mathrm{s} = \dot{\boldsymbol{e}} - (0, 0, \tfrac{1}{2}\mathit{\Omega}) \times \boldsymbol{e}$$

The angle between $\boldsymbol{v}_\mathrm{s}$ and $\boldsymbol{e}$ is denoted by α as shown in figure 4.2. The ξ-axis and the η-axis of the ξ, η-coordinate system depicted in this figure are chosen parallel and normal to the pure-squeeze velocity vector, respectively. The unit vectors $\boldsymbol{i}_\epsilon$ and $\boldsymbol{i}_\gamma$ are chosen parallel and normal to the eccentricity vector, respectively. The nondimensional pure-squeeze velocity vector $\boldsymbol{v}_\mathrm{s}^*$ is given by

$$\boldsymbol{v}_\mathrm{s}^* = \boldsymbol{\epsilon}' - (0, 0, \tfrac{1}{2}\mathit{\Omega}^*) \times \boldsymbol{\epsilon} = (\epsilon_x' + \tfrac{1}{2}\mathit{\Omega}^*\epsilon_y, \epsilon_y' - \tfrac{1}{2}\mathit{\Omega}^*\epsilon_x, 0) \tag{4.5}$$

Because the components of $\boldsymbol{\epsilon}'$ parallel and normal to the eccentricity vector are equal to ϵ' and $\epsilon\gamma'$, respectively, according to (4.5) the components of $\boldsymbol{v}_\mathrm{s}^*$ parallel and normal to the eccentricity vector are given by ϵ' and $\epsilon(\gamma' - \frac{1}{2}\mathit{\Omega}^*)$, respectively. The latter components can be written as $v_\mathrm{s}^* \cos\alpha$ and $-v_\mathrm{s}^* \sin\alpha$, respectively, and substitution into (4.3) yields (4.4).

The bearing reaction force components F_ϵ and F_γ parallel and normal to the eccentricity vector, respectively, are found by integration of the pressure according to

$$F_\epsilon = LR \int_0^{2\pi} \bar{p} \cos\phi \,\mathrm{d}\phi \quad \text{and} \quad F_\gamma = LR \int_0^{2\pi} \bar{p} \sin\phi \,\mathrm{d}\phi$$

where $\bar{p}$ is the pressure averaged in the axial direction:

$$\bar{p} = \frac{1}{L} \int_{-\frac{1}{2}L}^{\frac{1}{2}L} p \,\mathrm{d}z \tag{4.6}$$

With the nondimensional quantity $F_i^* = (C/R)^2 F_i / \mu \mathit{\Omega}_0 LD$ $(i = \epsilon, \gamma)$, the equations for F_ϵ and F_γ can be rewritten as

$$F_\epsilon^* = 3 \int_0^{2\pi} \bar{p}^* \cos\phi \,\mathrm{d}\phi \quad \text{and} \quad F_\gamma^* = 3 \int_0^{2\pi} \bar{p}^* \sin\phi \,\mathrm{d}\phi \tag{4.7}$$

where $\bar{p}^*$ is given by

$$\bar{p}^* = \int_{-\frac{1}{2}}^{\frac{1}{2}} p^* \, \mathrm{d}z^* \tag{4.8}$$

To eliminate the dependence on v_s^*, the rigid journal-bearing models are defined in terms of the so-called impedance vector, whose components W_i in some coordinate system are related to the nondimensional bearing reaction force components F_i^* according to

$$F_i^* = -v_\mathrm{s}^* W_i \tag{4.9}$$

In the following subsections, analytical expressions will be derived for the impedance components of the short, long, and approximate finite-length plain journal-bearing models. An exact finite-length journal-bearing model is obtained by discretization of the Reynolds equation by finite differences.

Short Bearing

For bearings with a length-diameter ratio L/D less than about $\frac{1}{2}$, the pressure gradient in the circumferential direction can be neglected in comparison to the pressure gradient in the axial direction, so that the first term on the left-hand side of the Reynolds equation (4.2) can be discarded. Integration with respect to z^* using the boundary conditions $p^* = 0$ at $z^* = -\frac{1}{2}$ and at $z^* = \frac{1}{2}$ yields

$$p^* = -(1 - 4z^{*2}) v_\mathrm{s}^* \cos(\alpha + \phi)(L/D)^2/h^3$$

and

$$\bar{p}^* = -\tfrac{2}{3} v_\mathrm{s}^* \cos(\alpha + \phi)(L/D)^2/h^3 \tag{4.10}$$

which is positive between the angles $\phi_1 = \frac{1}{2}\pi - \alpha$ and $\phi_2 = \frac{3}{2}\pi - \alpha$.

The impedance components W_ϵ and W_γ parallel and normal to the eccentricity vector, respectively, can be found from substitution of (4.10) into (4.7) using (4.9) and are given by

$$\begin{aligned} W_\epsilon &= 2(I_3^{02} \cos\alpha - I_3^{11} \sin\alpha)(L/D)^2 \\ W_\gamma &= 2(I_3^{11} \cos\alpha - I_3^{20} \sin\alpha)(L/D)^2 \end{aligned} \tag{4.11}$$

where

$$I_m^{jk} = \int_{\phi_1}^{\phi_2} \sin^j\phi \cos^k\phi h^{-m} \, \mathrm{d}\phi$$

is the so-called journal-bearing integral. A recursive table of the journal-bearing integral is given by Booker (1965b). Evaluation of the integrals yields

$$\begin{aligned} I_3^{02} &= \frac{1}{2(1-\epsilon^2)^2}\left[(1+2\epsilon^2)I_1^{00} + \frac{2\epsilon\cos\alpha\{3 + (2 - 5\epsilon^2)\sin^2\alpha\}}{(1-\epsilon^2\sin^2\alpha)^2}\right] \\ I_3^{11} &= -\frac{2\epsilon\sin^3\alpha}{(1-\epsilon^2\sin^2\alpha)^2} \\ I_3^{20} &= \frac{1}{2(1-\epsilon^2)}\left[I_1^{00} + \frac{2\epsilon\cos\alpha\{1 - (2-\epsilon^2)\sin^2\alpha\}}{(1-\epsilon^2\sin^2\alpha)^2}\right] \end{aligned}$$

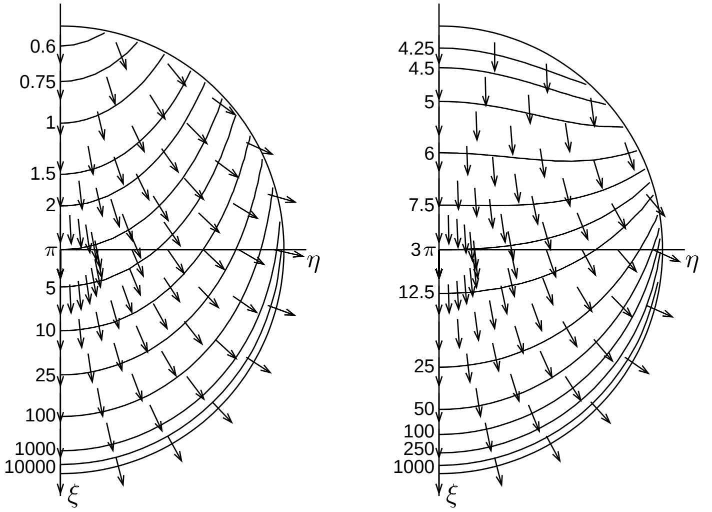

Figure 4.3: Short ($L/D = 1$) and long plain journal-bearing impedance plots

where

$$I_1^{00} = \frac{\arccos(-\delta A) + \arccos(-\delta B)}{\sqrt{1-\epsilon^2}} \tag{4.12}$$

and

$$A = \frac{\epsilon + \sin\alpha}{1 + \epsilon \sin\alpha} \qquad B = \frac{\epsilon - \sin\alpha}{1 - \epsilon \sin\alpha} \qquad \delta = \begin{array}{rl} 1, & \cos\alpha \geq 0 \\ -1, & \cos\alpha < 0 \end{array}$$

The impedance components W_ξ and W_η parallel and normal to the pure-squeeze velocity vector, respectively, can be found from

$$\begin{aligned} W_\xi &= W_\epsilon \cos\alpha - W_\gamma \sin\alpha \\ W_\eta &= W_\epsilon \sin\alpha + W_\gamma \cos\alpha \end{aligned} \tag{4.13}$$

Like W_ϵ and W_γ, these components are functions of ϵ, α, and L/D, but W_η is symmetric about the ξ-axis. The left panel of figure 4.3 shows the short plain journal-bearing impedance plot for $L/D = 1$ in the ξ, η-coordinate system, where the magnitude and the direction of the impedance vector are indicated by contour lines and arrows, respectively. Because of symmetry about the ξ-axis, only half the impedance plot is shown.

The components in the x, y-coordinate system can be found from

$$\begin{aligned} W_x &= W_\epsilon \sin\gamma + W_\gamma \cos\gamma \\ W_y &= -W_\epsilon \cos\gamma + W_\gamma \sin\gamma \end{aligned} \tag{4.14}$$

which are functions of ϵ, α, L/D, and γ. The nondimensional bearing reaction force components F_x^* and F_y^* in the x-direction and in the y-direction, respectively, can be found from (4.9).

Moes and Bosma (1981) give simplified expressions for the impedance components of the short plain journal bearing parallel and normal to the pure-squeeze velocity vector.

Long Bearing

For bearings with a length-diameter ratio greater than about 2 and bearings that are perfectly sealed, the pressure can be assumed constant in the axial direction, so that the second term on the left-hand side of the Reynolds equation (4.2) can be discarded. Integration with respect to ϕ yields

$$p^* = \bar{p}^* = -v_s^*(\cos\alpha\cos\phi - b\sin\alpha\sin\phi)(2+\epsilon\cos\phi)/h^2 \tag{4.15}$$

(Childs *et al.*, 1977), where $b = 2/(2+\epsilon^2)$. The boundary conditions used to obtain (4.15) are periodicity with respect to ϕ and the requirement that p^* is positive over π radians. The positive pressure sector is located between the angles ϕ_1 and ϕ_2, defined by

$$b\tan\phi_1 = 1/\tan\alpha \quad \text{and} \quad \phi_2 = \phi_1 + \pi$$

Solving ϕ_1 from the first equation yields

$$\phi_1 = \tfrac{1}{2}\pi - \alpha + \arctan\frac{\epsilon^2\sin(2\alpha)}{4+\epsilon^2(1+\cos(2\alpha))}$$

The impedance components parallel and normal to the eccentricity vector can be found from substitution of (4.15) into (4.7) using (4.9) and are given by

$$\begin{aligned} W_\epsilon &= 3\{(2I_2^{02}+\epsilon I_2^{03})\cos\alpha - b(2I_2^{11}+\epsilon I_2^{12})\sin\alpha\} \\ W_\gamma &= 3\{(2I_2^{11}+\epsilon I_2^{12})\cos\alpha - b(2I_2^{20}+\epsilon I_2^{21})\sin\alpha\} \end{aligned} \tag{4.16}$$

Evaluation of the integrals yields the following new exact expressions:

$$2I_2^{02}+\epsilon I_2^{03} = \frac{1}{1-\epsilon^2}\left[I_1^{00} + \frac{2\epsilon\sin\phi_1\{1+(1-\epsilon^2)\cos^2\phi_1\}}{1-\epsilon^2\cos^2\phi_1}\right]$$

$$2I_2^{11}+\epsilon I_2^{12} = -\frac{2\epsilon\cos^3\phi_1}{1-\epsilon^2\cos^2\phi_1}$$

$$2I_2^{20}+\epsilon I_2^{21} = I_1^{00} - \frac{2\epsilon\sin\phi_1\cos^2\phi_1}{1-\epsilon^2\cos^2\phi_1}$$

where I_1^{00} is given by (4.12) and

$$A = \frac{\epsilon+\cos\phi_1}{1+\epsilon\cos\phi_1} \qquad B = \frac{\epsilon-\cos\phi_1}{1-\epsilon\cos\phi_1} \qquad \delta = \begin{array}{rl} 1, & \sin\phi_1 \geq 0 \\ -1, & \sin\phi_1 < 0 \end{array}$$

The right panel of figure 4.3 shows the long plain journal-bearing impedance plot.

Moes and Bosma (1981) give approximate expressions for the impedance components of the long plain journal bearing, which exhibit considerable deviations for moderate to large ϵ and $\alpha > \frac{1}{2}\pi$ from the exact impedance components given here.

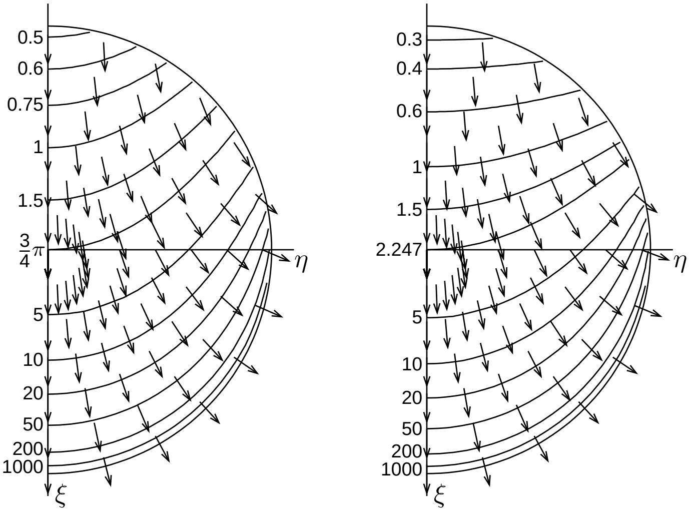

Figure 4.4: Approximate and exact finite-length plain journal-bearing impedance plots ($L/D = 1$)

Approximate Finite-Length Bearing

For small values of ϵ the short-bearing impedance components correspond well to the exact finite-length solution of the Reynolds equation, while the long bearing impedance components are too large. On the other hand, for large values of ϵ the long-bearing impedance components correspond well to the exact finite-length solution, while the short-bearing impedance components are too large. Using these facts, Moes and Bosma (1981) proposed an approximate finite-length bearing model by combining the short and long journal-bearing impedance components as follows:

$$\begin{aligned} 1/W_\epsilon &= 1/W_\epsilon^{\text{short}} + 1/W_\epsilon^{\text{long}} \\ 1/W_\gamma &= 1/W_\gamma^{\text{short}} + 1/W_\gamma^{\text{long}} \end{aligned} \tag{4.17}$$

The left panel of figure 4.4 shows the approximate finite-length plain journal-bearing impedance plot for $L/D = 1$.

Exact Finite-Length Bearing

Exact finite-length-bearing impedance components can be found numerically by solving $q^* = p^*/v_\text{s}^*$ from the rewritten Reynolds equation

$$\frac{\partial}{\partial \phi}\left(h^3 \frac{\partial q^*}{\partial \phi}\right) + \frac{h^3}{4(L/D)^2}\frac{\partial^2 q^*}{\partial z^{*2}} = 2\cos(\alpha + \phi) \tag{4.18}$$

using discretization with finite differences. Because of symmetry, only half the bearing ($0 \leq \phi < 2\pi$, $0 \leq z^* < \frac{1}{2}$) needs to be modeled. This area is discretized using a uniform mesh with intervals $\Delta\phi = 2\pi/n_\phi$ and $\Delta z^* = 1/2n_z$, where n_ϕ

and n_z are the number of intervals in the ϕ-direction and in the z^*-direction, respectively. The derivatives are approximated by the finite-difference schemes

$$\begin{aligned}
\frac{\partial}{\partial\phi}\left(h^3\frac{\partial q^*}{\partial\phi}\right) &\approx \frac{h^3_{i+\frac{1}{2}}q^*_{i+1,j} - (h^3_{i+\frac{1}{2}} + h^3_{i-\frac{1}{2}})q^*_{i,j} + h^3_{i-\frac{1}{2}}q^*_{i-1,j}}{\varDelta\phi^2} \\
\frac{\partial^2 q^*}{\partial z^{*2}} &\approx \frac{q^*_{i,j+1} - 2q^*_{i,j} + q^*_{i,j-1}}{\varDelta z^{*2}}
\end{aligned} \tag{4.19}$$

where $q^*_{i,j}$ and h_i represent q^* and h at $(\phi, z^*) = (\phi_i, z^*_j) = (i\varDelta\phi, j\varDelta z^*)$, respectively. The boundary conditions for q^* are periodicity with respect to ϕ and $q^* = 0$ at $z^* = -\frac{1}{2}$ and at $z^* = \frac{1}{2}$. Because of symmetry, it follows that $\partial q^*/\partial z^* = 0$ at $z^* = 0$, and the central-difference scheme yields $q^*_{i,-1} = q^*_{i,1}$. Negative values of $q^*_{i,j}$ are put equal to zero.

The impedance components parallel and normal to the eccentricity vector are given by

$$W_\epsilon = -3\int_0^{2\pi} \bar{q}^* \cos\phi \,\mathrm{d}\phi \quad \text{and} \quad W_\gamma = -3\int_0^{2\pi} \bar{q}^* \sin\phi \,\mathrm{d}\phi \tag{4.20}$$

where

$$\bar{q}^* = 2\int_0^{\frac{1}{2}} q^* \,\mathrm{d}z^*$$

The integrals are approximated using Simpson's rule. The right panel of figure 4.4 shows the exact finite-length plain journal-bearing impedance plot for $L/D = 1$ with $n_\phi = 200$ and $n_z = 16$.

4.2 Compliant Journal-Bearing Models

Figure 4.5 schematically shows the geometry of a compliant plain journal bearing with an elastically deformed bearing liner, where the dashed circle represents the undeformed situation. The origin of the stationary x, y, z-coordinate system is located at the center of the undeformed bearing. For the compliant journal-bearing models, the angular coordinate θ is used which is measured from the positive y-axis. The journal with radius R is assumed to be rigid and rotates with a constant angular speed $\varOmega$ about the z-axis. The position of its center is given by the eccentricity vector $\boldsymbol{e}$ with attitude angle γ. The radial clearance of the undeformed bearing is given by C, the film thickness by H, and the bearing-liner deformation is measured by U. Because of the necessity of two boundary conditions, for the long-bearing solution a lubricant inlet at the top of the bearing is assumed.

The film thickness can be found using the cosine rule of triangles:

$$(R + H)^2 = (R + C + U)^2 + e^2 + 2(R + C + U)e\cos(\theta - \gamma)$$

Expanding this equation, dividing by R^2, and discarding second-order terms in H/R, C/R, e/R, and U/R yields

$$H = C + e\cos(\theta - \gamma) + U = C + e_x \sin\theta - e_y \cos\theta + U$$

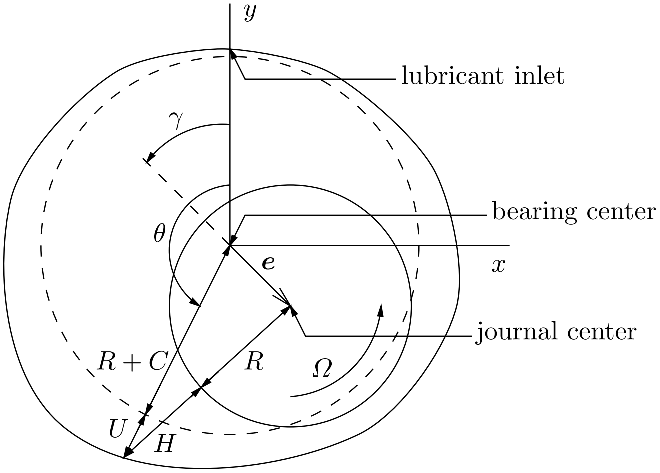

Figure 4.5: Geometry of a compliant plain journal bearing

where e_x and e_y are the eccentricity components in the x-direction and in the y-direction, respectively. With the nondimensional quantity $u = U/C$ this equation can be rewritten as

$$h = 1 + \epsilon_x \sin\theta - \epsilon_y \cos\theta + u \tag{4.21}$$

In the Reynolds equation (4.2), θ is substituted for ϕ. For compliant journal bearings, the Reynolds equation is a nonlinear partial differential equation because of the fact that the film thickness is coupled to the pressure by way of the the bearing liner elasticity. Choosing the nondimensional film thickness h as the degree of freedom in the model, (4.2) becomes a nonlinear partial differential equation in h and can be rewriting as

$$\frac{\partial h}{\partial \tau} = \tfrac{1}{2}\left\{\frac{\partial}{\partial\theta}\left(h^3\frac{\partial p^*}{\partial\theta}\right) + \frac{h^3}{4(L/D)^2}\frac{\partial^2 p^*}{\partial {z^*}^2} - \Omega^*\frac{\partial h}{\partial\theta}\right\} \tag{4.22}$$

where p^* can be expressed in terms of ϵ_x, ϵ_y, and h using the elasticity equation given below.

Assuming plain strain and Poisson's ratio not close to 0.5, the deformation of a thin elastic liner on a rigid backing can be approximated by

$$U = \frac{pd(1+\nu)(1-2\nu)}{E(1-\nu)}$$

(Hlaváček and Vokoun, 1993; Armstrong, 1986; Higginson, 1966), where d, E, and ν are the thickness, Young's modulus, and Poisson's ratio of the bearing liner, respectively. This equation can be rewritten as

$$u = Bp^* \tag{4.23}$$

(Higginson, 1966), where B is the nondimensional relative bearing-liner compliance, given by

$$B = \frac{6\mu\Omega_0 d(1+\nu)(1-2\nu)}{(C/R)^2 CE(1-\nu)}$$

which can be regarded as the ratio of lubricant-film to bearing-liner stiffness or as the ratio of bearing-liner to lubricant-film deformation. For rigid bearings, B is equal to zero. Note that for simplicity damping of the bearing liner has been neglected. The nondimensional pressure p^* can be expressed in terms of ϵ_x, ϵ_y, and h by substitution of (4.23) into (4.21) and solving for p^*:

$$p^* = (h - 1 - \epsilon_x \sin\theta + \epsilon_y \cos\theta)/B \tag{4.24}$$

To include the compliant journal-bearing model in the model of a rotor-bearing system, the nonlinear partial differential equation (4.22) in the film thickness is added to the equations of motion of the system. By means of spatial discretization with finite differences, the partial differential equation is transformed into a (large) set of ordinary differential equations in the discretized film thicknesses.

The bearing reaction force components F_x and F_y in the x-direction and in the y-direction, respectively, are found by integration of the pressure according to

$$F_x = LR \int_0^{2\pi} \bar{p} \sin\theta \, \mathrm{d}\theta \quad \text{and} \quad F_y = -LR \int_0^{2\pi} \bar{p} \cos\theta \, \mathrm{d}\theta$$

where $\bar{p}$ is the pressure averaged in the axial direction according to (4.6). The nondimensional bearing reaction force components F_x^* and F_y^* in the x-direction and in the y-direction, respectively, are given by

$$F_x^* = 3 \int_0^{2\pi} \bar{p}^* \sin\theta \, \mathrm{d}\theta \quad \text{and} \quad F_y^* = -3 \int_0^{2\pi} \bar{p}^* \cos\theta \, \mathrm{d}\theta \tag{4.25}$$

where $\bar{p}^*$ is given by (4.8). As an approximate cavitation model negative pressures are put equal to zero in the evaluation of these integrals, whereas in the nonlinear partial differential equation (4.22) negative values are allowed. This approach provides a smooth approximation to the more accurate discontinuous cavitation model, in which constraints are used to prevent the discretized film thicknesses from causing negative pressures. The nonlinear dynamics of discontinuous systems that are not approximated by smoothing are treated by Leine *et al.* (2000). This work is based on previous research on dry friction models by van de Vrande *et al.* (1999, 1997).

Spatial discretization of the two-dimensional nonlinear partial differential equation (4.22) yields a compliant exact finite-length journal-bearing model. This model will not be treated in this thesis because of the fact that the resulting system of ordinary differential equations is very large. In the following subsections, the partial differential equation will be simplified for the short- and long-bearing approximations.

Short Bearing

Neglecting the first term on the left-hand side of the Reynolds equation (4.2), integration of this equation with respect to z^*, and using the boundary conditions $p^* = 0$ at $z^* = -\frac{1}{2}$ and at $z^* = \frac{1}{2}$ yields

$$p^* = -\frac{(1 - 4z^{*2})}{2h^3} \left(\Omega^* \frac{\partial h}{\partial \theta} + 2 \frac{\partial h}{\partial \tau} \right) \left(\frac{L}{D} \right)^2$$

so that

$$\bar{p}^* = -\frac{1}{3h^3}\left(\Omega^*\frac{\partial h}{\partial \theta} + 2\frac{\partial h}{\partial \tau}\right)\left(\frac{L}{D}\right)^2 \tag{4.26}$$

Rearranging the terms in this equation yields the following nonlinear partial differential equation in the film thickness:

$$\frac{\partial h}{\partial \tau} = -\tfrac{1}{2}\left(\frac{3h^3\bar{p}^*}{(L/D)^2} + \Omega^*\frac{\partial h}{\partial \theta}\right) \tag{4.27}$$

Assuming that the bearing-liner deformation is a function of the average pressure ($u = B\bar{p}^*$), it is not a function of z but only of θ and it follows that

$$\bar{p}^* = (h - 1 - \epsilon_x \sin\theta + \epsilon_y \cos\theta)/B$$

and the partial differential equation (4.27) becomes one-dimensional. The derivative of the nondimensional film thickness with respect to the angular coordinate is discretized by the second-order backward-difference scheme

$$\left.\frac{\partial h}{\partial \theta}\right|_i \approx \frac{3h_i - 4h_{i-1} + h_{i-2}}{2\Delta\theta} \tag{4.28}$$

using periodicity as the boundary condition. This finite-difference scheme is used because of its numerical stability.

Long Bearing

Neglecting the term with the derivative with respect to z^* in (4.22) yields

$$\frac{\partial h}{\partial \tau} = \tfrac{1}{2}\left(\frac{\partial}{\partial \theta}\left(h^3\frac{\partial p^*}{\partial \theta}\right) - \Omega^*\frac{\partial h}{\partial \theta}\right) \tag{4.29}$$

where p^* is given by (4.24). For the long bearing, by definition p^* is a function only of θ, so that (4.29) is one-dimensional. The first derivative in the right-hand side of (4.29) is discretized by the finite-difference scheme

$$\left.\frac{\partial}{\partial \theta}\left(h^3\frac{\partial p^*}{\partial \theta}\right)\right|_i \approx \frac{h^3_{i+\frac{1}{2}}p^*_{i+1} - (h^3_{i+\frac{1}{2}} + h^3_{i-\frac{1}{2}})p^*_i + h^3_{i-\frac{1}{2}}p_{i-1}}{\Delta\theta^2}$$

where $h_{i+\frac{1}{2}}$ is approximated by $-\frac{1}{8}h_{i-1} + \frac{3}{4}h_i + \frac{3}{8}h_{i+1}$. The derivative of h with respect to θ is discretized by (4.28). Because of the fact that the boundary conditions used for the rigid long journal-bearing model cannot be used for the compliant long journal-bearing model, a lubricant inlet at the top of the bearing is assumed. In this case the two boundary conditions, necessary for the second-order partial differential equation (4.29), are periodicity with respect to θ and $p^* = 0$ at $\theta = 0$.

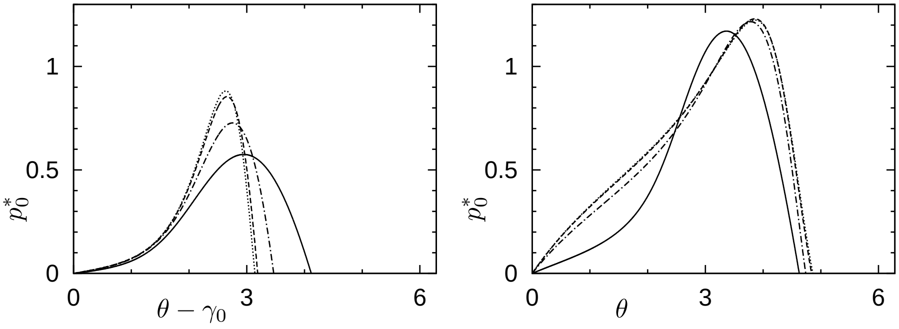

Figure 4.6: Compliant short-bearing ($L/D = 1$, $S = 2.5$, right panel) and long-bearing ($S = 5.0$, left panel) pressure distributions, respectively (dotted line: $B = 0$, dashed line: $B = 0.01$, dash-dotted line: $B = 0.1$, solid line: $B = 1$)

Pressure Distributions

The influence of the nondimensional relative bearing-liner compliance B on the nondimensional pressure distribution p_0^* evaluated at the equilibrium position is depicted in the left and right panels of figure 4.6 for the compliant short and long plain journal-bearing models, respectively. In this figure, p_0^* is plotted as a function of the circumferential coordinate for the Sommerfeld numbers $S = 2.5$ and $S = 5.0$ for the short- and long-bearing models, respectively, and for different values of B. The dotted lines in the figure represent the results of the corresponding rigid journal bearings, for which B is equal to zero. For the calculations, Ω^* is put equal to 1. For the short bearing, the influence of the bearing-liner compliance on the peak pressure is considerable.

4.3 Rigid Bearing Stiffness and Damping Coefficients

In linear rotordynamics, stiffness and damping coefficients are used to model the journal bearings. With these coefficients, small-amplitude synchronous vibrations about an equilibrium position can be calculated and the stability of the equilibrium position can be analyzed (to determine the stability threshold). In this section, these coefficients will be derived for the rigid journal-bearing models.

It is assumed (without loss of generality) that a constant load of magnitude F_0 is applied to the bearing in the negative y-direction. Furthermore, Ω_0 is chosen equal to Ω, so that $\Omega^* = 1$. The equilibrium position of the journal is given by $\boldsymbol{\epsilon} = \epsilon_0(\sin\gamma_0, -\cos\gamma_0)$, whereas by definition $\boldsymbol{\epsilon}' = \mathbf{0}$. From (4.5) it follows that $\boldsymbol{v}^*_{\mathrm{s},0} = \frac{1}{2}(-\cos\gamma_0, -\sin\gamma_0, 0)$, so that $\alpha_0 = \frac{1}{2}\pi$. The stiffness and damping coefficients are defined by

$$k_{ij} = -\frac{\partial F_i}{\partial e_j} \quad \text{and} \quad b_{ij} = -\frac{\partial F_i}{\partial \dot{e}_j} \tag{4.30}$$

where $i, j = x, y$ and the derivatives are evaluated at the equilibrium position.

With the nondimensional quantities

$$k^* = \frac{(C/R)^2 C}{\mu \varOmega L D} k \quad \text{and} \quad b^* = \frac{(C/R)^2 C}{\mu L D} b$$

(4.30) can be rewritten as

$$k^*_{ij} = -\frac{\partial F^*_i}{\partial \epsilon_j} \quad \text{and} \quad b^*_{ij} = -\frac{\partial F^*_i}{\partial \epsilon'_j} \tag{4.31}$$

To express the nondimensional stiffness and damping coefficients in terms of the impedance components, (4.9) is used to expand (4.31) according to

$$k^*_{ij} = \left(\frac{\partial v^*_\mathrm{s}}{\partial \epsilon_j} W_{i,0} + v^*_{\mathrm{s},0} \frac{\partial W_i}{\partial \epsilon_j} \right) \quad \text{and} \quad b^*_{ij} = \frac{\partial v^*_\mathrm{s}}{\partial \epsilon'_j} W_{i,0} + v^*_{\mathrm{s},0} \frac{\partial W_i}{\partial \epsilon'_j} \tag{4.32}$$

Using the definition $v^{*2}_\mathrm{s} = (\epsilon'_x + \frac{1}{2}\epsilon_y)^2 + (\epsilon'_y - \frac{1}{2}\epsilon_x)^2$, it follows that $v^*_{\mathrm{s},0} = \frac{1}{2}\epsilon_0$ and the derivatives of v^*_s evaluated at the equilibrium position are given by

$$\begin{aligned} \frac{\partial v^*_\mathrm{s}}{\partial \epsilon_x} &= \tfrac{1}{2}\sin\gamma_0 & \qquad \frac{\partial v^*_\mathrm{s}}{\partial \epsilon'_x} &= -\cos\gamma_0 \\ \frac{\partial v^*_\mathrm{s}}{\partial \epsilon_y} &= -\tfrac{1}{2}\cos\gamma_0 & \qquad \frac{\partial v^*_\mathrm{s}}{\partial \epsilon'_y} &= -\sin\gamma_0 \end{aligned}$$

From (4.14) it follows that

$$\begin{aligned} W_{x,0} &= W_{\epsilon,0}\sin\gamma_0 + W_{\gamma,0}\cos\gamma_0 \\ W_{y,0} &= -W_{\epsilon,0}\cos\gamma_0 + W_{\gamma,0}\sin\gamma_0 \end{aligned}$$

so that the derivatives of W_x and W_y with respect to ϵ_i and ϵ'_i are given by

$$\begin{aligned} \frac{\partial W_x}{\partial \epsilon_i} &= \left(\frac{\partial W_\epsilon}{\partial \epsilon}\sin\gamma_0 + \frac{\partial W_\gamma}{\partial \epsilon}\cos\gamma_0 \right) \frac{\partial \epsilon}{\partial \epsilon_i} + \left(W_{\epsilon,0}\cos\gamma_0 - W_{\gamma,0}\sin\gamma_0 \right) \frac{\partial \gamma}{\partial \epsilon_i} \\ \frac{\partial W_y}{\partial \epsilon_i} &= \left(-\frac{\partial W_\epsilon}{\partial \epsilon}\cos\gamma_0 + \frac{\partial W_\gamma}{\partial \epsilon}\sin\gamma_0 \right) \frac{\partial \epsilon}{\partial \epsilon_i} + \left(W_{\epsilon,0}\sin\gamma_0 + W_{\gamma,0}\cos\gamma_0 \right) \frac{\partial \gamma}{\partial \epsilon_i} \\ \frac{\partial W_x}{\partial \epsilon'_i} &= \left(\frac{\partial W_\epsilon}{\partial \alpha}\sin\gamma_0 + \frac{\partial W_\gamma}{\partial \alpha}\cos\gamma_0 \right) \frac{\partial \alpha}{\partial \epsilon'_i} \\ \frac{\partial W_y}{\partial \epsilon'_i} &= \left(-\frac{\partial W_\epsilon}{\partial \alpha}\cos\gamma_0 + \frac{\partial W_\gamma}{\partial \alpha}\sin\gamma_0 \right) \frac{\partial \alpha}{\partial \epsilon'_i} \end{aligned}$$

where $i = x, y$. Using the definitions

$$\epsilon = \sqrt{\epsilon_x^2 + \epsilon_y^2} \qquad \gamma = -\arctan\frac{\epsilon_x}{\epsilon_y} \qquad \alpha = \arctan\frac{\epsilon_y}{\epsilon_x} - \arctan\frac{\epsilon'_y - \frac{1}{2}\epsilon_x}{\epsilon'_x + \frac{1}{2}\epsilon_y}$$

it follows that the derivatives of ϵ, γ, and α with respect to ϵ_i and ϵ'_i are given by

$$\begin{aligned} \frac{\partial \epsilon}{\partial \epsilon_x} &= \sin\gamma_0 & \qquad \frac{\partial \gamma}{\partial \epsilon_x} &= \frac{1}{\epsilon_0}\cos\gamma_0 & \qquad \frac{\partial \alpha}{\partial \epsilon'_x} &= -\frac{2}{\epsilon_0}\sin\gamma_0 \\ \frac{\partial \epsilon}{\partial \epsilon_y} &= -\cos\gamma_0 & \qquad \frac{\partial \gamma}{\partial \epsilon_y} &= \frac{1}{\epsilon_0}\sin\gamma_0 & \qquad \frac{\partial \alpha}{\partial \epsilon'_y} &= \frac{2}{\epsilon_0}\cos\gamma_0 \end{aligned}$$

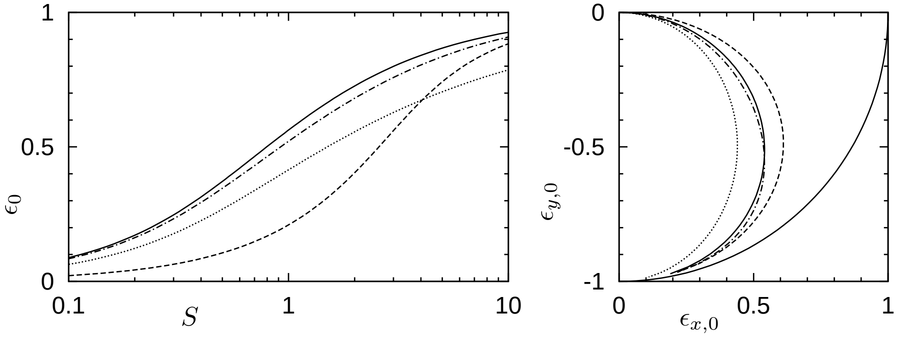

Figure 4.7: Rigid bearing nondimensional eccentricity versus Sommerfeld number and equilibrium locus for $L/D = 1$ (dotted line: short, dashed line: long, dash-dotted line: approximate finite-length, solid line: exact finite-length)

The attitude angle at the equilibrium position can be found from

$$\gamma_0 = -\arctan \frac{W_{\gamma,0}}{W_{\epsilon,0}}$$

In the following subsections, analytical expressions will be derived for the stiffness and damping coefficients of the short, long, and approximate finite-length plain journal-bearing models. The stiffness and damping coefficients of the exact finite-length plain journal-bearing model will also be given.

Short Bearing

The impedance components of the short journal bearing parallel and normal to the eccentricity vector evaluated at the equilibrium position ($\epsilon = \epsilon_0$ and $\alpha = \frac{1}{2}\pi$) are given by

$$W_{\epsilon,0} = \frac{4\epsilon_0}{(1-\epsilon_0^2)^2}\left(\frac{L}{D}\right)^2 \quad \text{and} \quad W_{\gamma,0} = -\frac{\pi}{(1-\epsilon_0^2)^{3/2}}\left(\frac{L}{D}\right)^2 \tag{4.33}$$

Using these expressions, the Sommerfeld number $S = F_0^* = \frac{1}{2}\epsilon_0 W_0$ and the attitude angle evaluated at the equilibrium position are given by

$$S = \frac{\epsilon_0\sqrt{16\epsilon_0^2 + \pi^2(1-\epsilon_0^2)}}{2(1-\epsilon_0^2)^2}\left(\frac{L}{D}\right)^2 \quad \text{and} \quad \gamma_0 = \arctan \frac{\pi\sqrt{1-\epsilon_0^2}}{4\epsilon_0} \tag{4.34}$$

The dotted lines in the left and right panels of figure 4.7 show the nondimensional eccentricity versus the Sommerfeld number and the equilibrium locus of the short journal bearing for $L/D = 1$, respectively.

Taking the derivatives of W_ϵ and W_γ given by (4.11) with respect to ϵ and α and evaluation at the equilibrium position yields

$$\begin{aligned} \frac{\partial W_\epsilon}{\partial \epsilon} &= \frac{4(1+3\epsilon_0^2)}{(1-\epsilon_0^2)^3}\left(\frac{L}{D}\right)^2 & \frac{\partial W_\epsilon}{\partial \alpha} &= -\frac{\pi(1+2\epsilon_0^2)}{(1-\epsilon_0^2)^{5/2}}\left(\frac{L}{D}\right)^2 \\ \frac{\partial W_\gamma}{\partial \epsilon} &= -\frac{3\pi\epsilon_0}{(1-\epsilon_0^2)^{5/2}}\left(\frac{L}{D}\right)^2 & \frac{\partial W_\gamma}{\partial \alpha} &= \frac{4\epsilon_0}{(1-\epsilon_0^2)^2}\left(\frac{L}{D}\right)^2 \end{aligned} \tag{4.35}$$

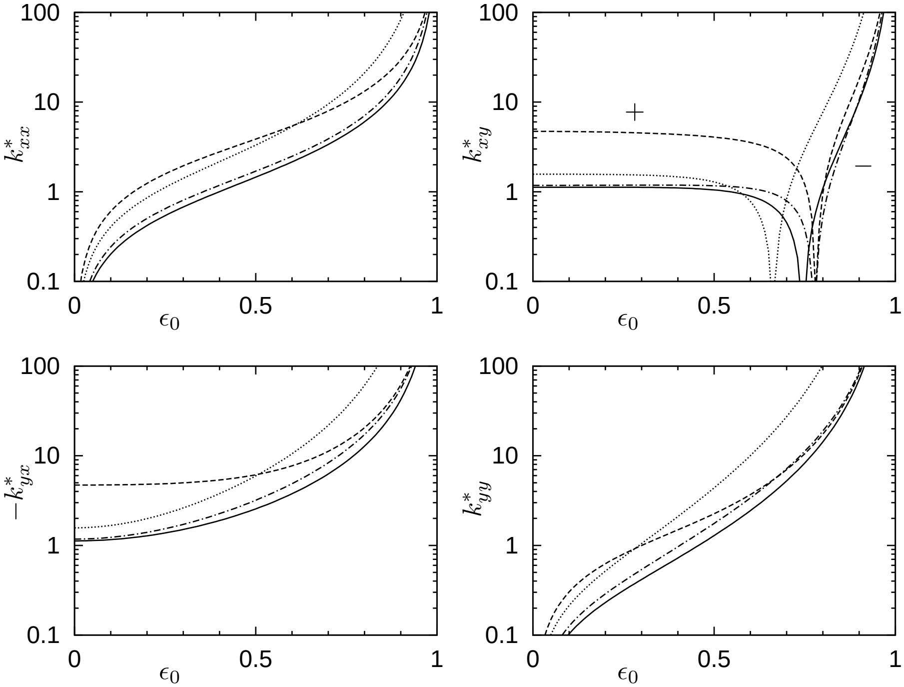

Figure 4.8: Rigid bearing stiffness coefficients for $L/D = 1$ (dotted line: short, dashed line: long, dash-dotted line: approximate finite-length, solid line: exact finite-length)

Substitution of (4.33) and (4.35) into (4.31) and using (4.34) yields the nondimensional stiffness and damping coefficients given in appendix B. The dotted lines in figures 4.8 and 4.9 show the stiffness and damping coefficients of the short journal bearing as functions of the eccentricity, respectively. As known, the cross stiffness and damping coefficients are mostly negative.

Long Bearing

The impedance components of the long journal bearing parallel and normal to the eccentricity vector evaluated at the equilibrium position are given by

$$W_{\epsilon,0} = \frac{12\epsilon_0}{(2+\epsilon_0^2)(1-\epsilon_0^2)} \quad \text{and} \quad W_{\gamma,0} = -\frac{6\pi}{(2+\epsilon_0^2)\sqrt{1-\epsilon_0^2}}$$

The Sommerfeld number and the attitude angle evaluated at the equilibrium position are given by

$$S = \frac{3\epsilon_0\sqrt{4\epsilon_0^2+\pi^2(1-\epsilon_0^2)}}{(2+\epsilon_0^2)(1-\epsilon_0^2)} \quad \text{and} \quad \gamma_0 = \arctan\frac{\pi\sqrt{1-\epsilon_0^2}}{2\epsilon_0}$$

The dashed lines in the left and right panels of figure 4.7 show the nondimensional eccentricity versus the Sommerfeld number and the equilibrium locus of the long

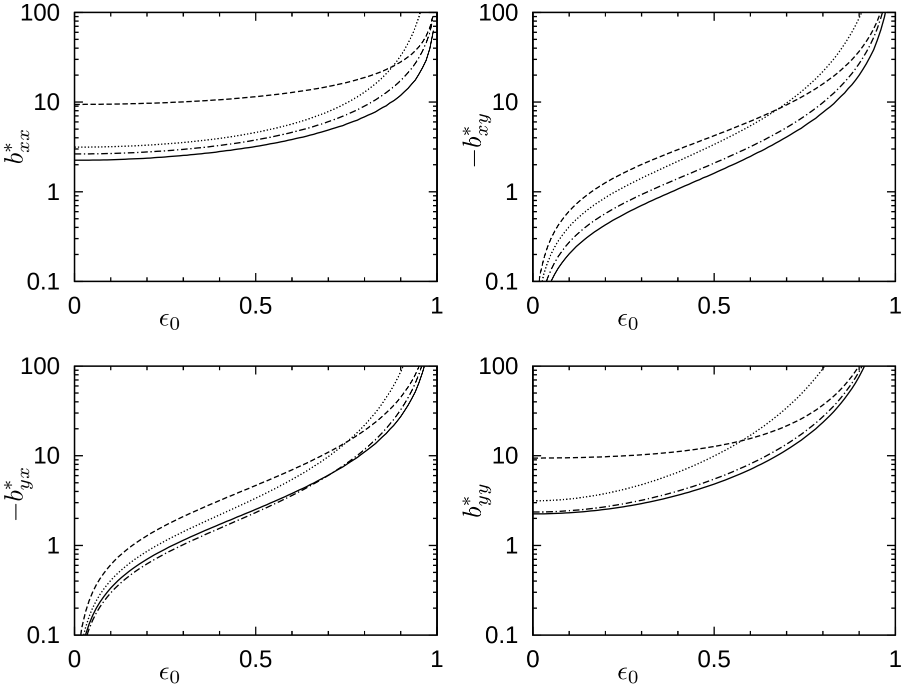

Figure 4.9: Rigid bearing damping coefficients for $L/D = 1$ (dotted line: short, dashed line: long, dash-dotted line: approximate finite-length, solid line: exact finite-length)

journal bearing, respectively.

Taking the derivatives of W_ϵ and W_γ given by (4.16) with respect to ϵ and α and evaluation at the equilibrium position yields

$$\frac{\partial W_\epsilon}{\partial \epsilon} = \frac{12(2+\epsilon_0^2+3\epsilon_0^4)}{(2+\epsilon_0^2)^2(1-\epsilon_0^2)^2} \qquad \frac{\partial W_\epsilon}{\partial \alpha} = -\frac{3\pi}{(1-\epsilon_0^2)^{3/2}}$$
$$\frac{\partial W_\gamma}{\partial \epsilon} = -\frac{18\pi\epsilon_0^3}{(2+\epsilon_0^2)^2(1-\epsilon_0^2)^{3/2}} \qquad \frac{\partial W_\gamma}{\partial \alpha} = \frac{6\epsilon_0}{1-\epsilon_0^2}$$

The resulting nondimensional stiffness and damping coefficients are given in appendix B. The dashed lines in figures 4.8 and 4.9 show the stiffness and damping coefficients of the long journal bearing as functions of the eccentricity, respectively.

Approximate Finite-Length Bearing

The impedance components of the approximate finite-length journal bearing parallel and normal to the eccentricity vector evaluated at the equilibrium position are given by

$$W_{\epsilon,0} = \frac{12\Lambda^2\epsilon_0}{A(1-\epsilon_0^2)} \quad \text{and} \quad W_{\gamma,0} = -\frac{6\pi\Lambda^2}{B\sqrt{1-\epsilon_0^2}}$$

where $A = 2\Lambda^2 + 3 + (\Lambda^2 - 3)\epsilon_0^2$, $B = 2(\Lambda^2 + 3) + (\Lambda^2 - 6)\epsilon_0^2$, and $\Lambda = L/D$. The Sommerfeld number and the attitude angle evaluated at the equilibrium position are given by

$$S = \frac{3\Lambda^2\epsilon_0\sqrt{4B^2\epsilon_0^2 + \pi^2 A^2(1-\epsilon_0^2)}}{AB(1-\epsilon_0^2)} \quad \text{and} \quad \gamma_0 = \arctan\frac{\pi A\sqrt{1-\epsilon_0^2}}{2B\epsilon}$$

The dash-dotted lines in the left and right panels of figure 4.7 show the nondimensional eccentricity versus the Sommerfeld number and the equilibrium locus of the finite-length journal bearing for $L/D = 1$, respectively.

Taking the derivatives of W_ϵ and W_γ given by (4.17) with respect to ϵ and α and evaluation at the equilibrium position yields

$$\begin{aligned}
\frac{\partial W_\epsilon}{\partial \epsilon} &= \frac{12\Lambda^2\{2\Lambda^2 + 3 + (\Lambda^2+6)\epsilon_0^2 + 3(\Lambda^2-3)\epsilon_0^4\}}{A^2(1-\epsilon_0^2)^2}\\
\frac{\partial W_\gamma}{\partial \epsilon} &= -\frac{18\pi\Lambda^2\epsilon\{6 + (\Lambda^2-6)\epsilon_0^2\}}{B^2(1-\epsilon_0^2)^{3/2}}\\
\frac{\partial W_\epsilon}{\partial \alpha} &= -\frac{3\pi\Lambda^2\{(4\Lambda^2+3)(1+\epsilon_0^2) + (\Lambda^2-6)\epsilon_0^4\}}{A^2(1-\epsilon_0^2)^{3/2}}\\
\frac{\partial W_\gamma}{\partial \alpha} &= \frac{6\Lambda^2\epsilon_0\{4(\Lambda^2+6) + 4(\Lambda^2-6)\epsilon_0^2 + \Lambda^2\epsilon_0^4\}}{B^2(1-\epsilon_0^2)}
\end{aligned}$$

The stiffness and damping coefficients can be obtained by substitution of these terms into (4.32). Because of the fact that the resulting expressions for the stiffness and damping coefficients cannot be easily simplified, they are not explicitly given here. The dash-dotted lines in figures 4.8 and 4.9 show the stiffness and damping coefficients of the approximate finite-length journal bearing as functions of the eccentricity, respectively.

Exact Finite-Length Bearing

The impedance components of the exact finite-length journal bearing parallel and normal to the eccentricity vector evaluated at the equilibrium position are given by

$$W_{\epsilon,0} = -3\int_0^{2\pi} \bar{q}_0^* \cos\phi \,\mathrm{d}\phi \quad \text{and} \quad W_{\gamma,0} = -3\int_0^{2\pi} \bar{q}_0^* \sin\phi \,\mathrm{d}\phi \tag{4.36}$$

where

$$\bar{q}_0^* = 2\int_0^{\frac{1}{2}} q_0^* \,\mathrm{d}z^*$$

The quantity q_0^* is solved numerically from the rewritten Reynolds equation evaluated at the equilibrium position

$$\frac{\partial}{\partial\phi}\left(h^3\frac{\partial q_0^*}{\partial\phi}\right) + \frac{h^3}{4(L/D)^2}\frac{\partial^2 q_0^*}{\partial z^{*2}} = -2\sin\phi \tag{4.37}$$

using the finite-difference schemes given by (4.19). The solid lines in the left and right panels of figure 4.7 show the nondimensional eccentricity versus the

Sommerfeld number and the equilibrium locus of the exact finite-length journal bearing for $L/D = 1$, respectively.

Taking the derivatives of W_ϵ and W_γ given by (4.20) with respect to ϵ and α yields

$$\begin{aligned}
\frac{\partial W_\epsilon}{\partial \epsilon} &= -3\int_0^{2\pi} \frac{\partial \bar{q}^*}{\partial \epsilon}\cos\phi\,\mathrm{d}\phi &\qquad \frac{\partial W_\gamma}{\partial \epsilon} &= -3\int_0^{2\pi} \frac{\partial \bar{q}^*}{\partial \epsilon}\sin\phi\,\mathrm{d}\phi \\
\frac{\partial W_\epsilon}{\partial \alpha} &= -3\int_0^{2\pi} \frac{\partial \bar{q}^*}{\partial \alpha}\cos\phi\,\mathrm{d}\phi &\qquad \frac{\partial W_\gamma}{\partial \alpha} &= -3\int_0^{2\pi} \frac{\partial \bar{q}^*}{\partial \alpha}\sin\phi\,\mathrm{d}\phi
\end{aligned}$$

where

$$\frac{\partial \bar{q}^*}{\partial \epsilon} = 2\int_0^{\frac{1}{2}} \frac{\partial q^*}{\partial \epsilon}\,\mathrm{d}z^* \quad \text{and} \quad \frac{\partial \bar{q}^*}{\partial \alpha} = 2\int_0^{\frac{1}{2}} \frac{\partial q^*}{\partial \alpha}\,\mathrm{d}z^*$$

Taking the derivatives of the rewritten Reynolds equation (4.18), the following equations are found for $\partial q^*/\partial\epsilon$ and $\partial q^*/\partial\alpha$ evaluated at the equilibrium position:

$$\begin{aligned}
&\frac{\partial}{\partial\theta}\left(h^3\frac{\partial}{\partial\theta}\left(\frac{\partial q^*}{\partial\epsilon}\right)\right) + \frac{h^3}{4(L/D)^2}\frac{\partial^2}{\partial z^{*2}}\left(\frac{\partial q^*}{\partial\epsilon}\right) = 3\sin\theta\left(\frac{12\cos\theta}{h} + h\frac{\partial q_0^*}{\partial\theta}\right) \\
&\frac{\partial}{\partial\theta}\left(h^3\frac{\partial}{\partial\theta}\left(\frac{\partial q^*}{\partial\alpha}\right)\right) + \frac{h^3}{4(L/D)^2}\frac{\partial^2}{\partial z^{*2}}\left(\frac{\partial q^*}{\partial\alpha}\right) = -2\cos\theta
\end{aligned} \tag{4.38}$$

These equations are discretized by the finite-difference schemes given by (4.19). Because of the fact that the left-hand sides of these equations are similar to the left-hand side of (4.37), $\partial q^*/\partial\epsilon$ and $\partial q^*/\partial\alpha$ can be found by back-substitution. The derivative $\partial q_0^*/\partial\theta$ in the right-hand side of the first equation in (4.38) is approximated using the central-difference scheme. The solid lines in figures 4.8 and 4.9 show the stiffness and damping coefficients of the exact finite-length journal bearing as functions of the eccentricity, respectively.

4.4 Compliant Bearing Stiffness and Damping Coefficients

In this section, the stiffness and damping coefficients of the compliant journal-bearing models will be derived. A constant load of magnitude F_0 is applied to the bearing in the negative y-direction and Ω_0 is chosen equal to Ω, so that $\Omega^* = 1$. Harmonic perturbations with excitation frequency ω are imposed on the nondimensional eccentricity and the attitude angle at the equilibrium position according to

$$\begin{aligned}
\epsilon &= \epsilon_0 + \delta\epsilon \\
\gamma &= \gamma_0 + \delta\gamma
\end{aligned} \tag{4.39}$$

The second total derivatives of these perturbations with respect to τ are given by $\delta\epsilon'' = -(\omega/\Omega)^2\delta\epsilon$ and $\delta\gamma'' = -(\omega/\Omega)^2\delta\gamma$. The nondimensional film thickness reacts to the perturbations according to

$$h = h_0 + \frac{\partial h}{\partial\epsilon}\delta\epsilon + \frac{\partial h}{\partial\gamma}\delta\gamma + \frac{\partial h}{\partial\epsilon'}\delta\epsilon' + \frac{\partial h}{\partial\gamma'}\delta\gamma' \tag{4.40}$$

Substitution of this equation into (4.22) yields a set of ordinary differential equations in h_0 and in the derivatives of h. The stiffness and damping coefficients can be expressed in terms of these derivatives and depend on the angular excitation frequency to angular rotor speed ratio ω/Ω.

Short Bearing

For the short journal bearing, the angular coordinate $\phi = \theta - \gamma$ is used instead of θ and the stiffness and damping coefficients are derived in the ϵ, γ-coordinate system. The coefficients in the x, y-coordinate system can be determined from these coefficients by means of a rotation. Equation (4.27) becomes

$$\frac{\partial h}{\partial \phi} = -\frac{3h^3 \bar{p}^*}{(L/D)^2} - 2\frac{\partial h}{\partial \tau}$$

where $\bar{p}^* = (h - 1 - \epsilon \cos\phi)/B$. Substitution of (4.39) and (4.40) into this equation yields the following boundary-value problem:

$$\begin{aligned}
\frac{\partial h_0}{\partial \phi} &= -\frac{3h_0^3 \bar{p}_0^*}{(L/D)^2} \\
\frac{\partial}{\partial \phi}\left(\frac{\partial h}{\partial \epsilon}\right) &= -\frac{3}{(L/D)^2}\left\{\frac{h_0^3}{B}\left(\frac{\partial h}{\partial \epsilon} - \cos\phi\right) + 3h_0^2 \bar{p}_0^* \frac{\partial h}{\partial \epsilon}\right\} + 2\left(\frac{\omega}{\Omega}\right)^2 \frac{\partial h}{\partial \epsilon'} \\
\frac{\partial}{\partial \phi}\left(\frac{\partial h}{\partial \gamma}\right) &= -\frac{3}{(L/D)^2}\left\{\frac{h_0^3}{B}\left(\frac{\partial h}{\partial \gamma} - \epsilon \sin\phi\right) + 3h_0^2 \bar{p}_0^* \frac{\partial h}{\partial \gamma}\right\} + 2\left(\frac{\omega}{\Omega}\right)^2 \frac{\partial h}{\partial \gamma'} \\
\frac{\partial}{\partial \phi}\left(\frac{\partial h}{\partial \epsilon'}\right) &= -\frac{3}{(L/D)^2}\left(\frac{h_0^3}{B} + 3h_0^2 \bar{p}_0^*\right)\frac{\partial h}{\partial \epsilon'} - 2\frac{\partial h}{\partial \epsilon} \\
\frac{\partial}{\partial \phi}\left(\frac{\partial h}{\partial \gamma'}\right) &= -\frac{3}{(L/D)^2}\left(\frac{h_0^3}{B} + 3h_0^2 \bar{p}_0^*\right)\frac{\partial h}{\partial \gamma'} - 2\frac{\partial h}{\partial \gamma}
\end{aligned}$$

where $\bar{p}_0^* = (h_0 - 1 - \epsilon_0 \cos\phi)/B$ and the boundary condition for h_0 and the derivatives of h is periodicity with respect to ϕ. This boundary-value problem can be solved by the shooting method.

The nondimensional bearing reaction force components parallel and normal to the eccentricity vector evaluated at the equilibrium position are given by

$$F_{\epsilon,0}^* = 3\int_0^{2\pi} \bar{p}_0^* \cos\phi \, \mathrm{d}\phi \quad \text{and} \quad F_{\gamma,0}^* = 3\int_0^{2\pi} \bar{p}_0^* \sin\phi \, \mathrm{d}\phi$$

The Sommerfeld number and the attitude angle evaluated at the equilibrium position are given by

$$S = \sqrt{F_{\epsilon,0}^{*2} + F_{\gamma,0}^{*2}} \quad \text{and} \quad \gamma_0 = -\arctan\frac{F_{\gamma,0}^*}{F_{\epsilon,0}^*}$$

The left and right panels of figure 4.10 show the nondimensional eccentricity versus the Sommerfeld number and the equilibrium locus of the compliant short journal bearing, respectively, for $L/D = 1$ and different values of B. The dotted lines in this figure represent the results of the rigid short journal bearing, for which B is equal to zero. Higginson (1966) shows that the range of B for metal bearings is 0.001–0.1 and for plastic bearings is 0.1–100.

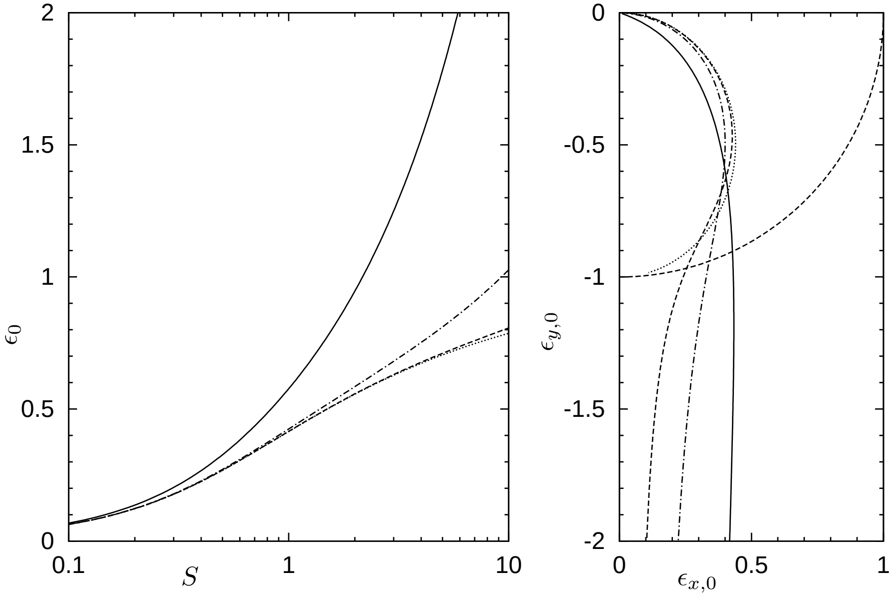

Figure 4.10: Compliant short-bearing nondimensional eccentricity versus Sommerfeld number and equilibrium locus for $L/D = 1$ (dotted line: $B = 0$, dashed line: $B = 0.01$, dash-dotted line: $B = 0.1$, solid line: $B = 1$)

The stiffness and damping coefficients in the ϵ, γ-coordinate system are defined by

$$k^*_{\epsilon\epsilon} = -3\int_0^{2\pi} \frac{\partial \bar{p}^*}{\partial \epsilon} \cos\phi \, \mathrm{d}\phi \qquad k^*_{\epsilon\gamma} = -\frac{3}{\epsilon_0}\int_0^{2\pi} \frac{\partial \bar{p}^*}{\partial \gamma} \cos\phi \, \mathrm{d}\phi$$
$$k^*_{\gamma\epsilon} = -3\int_0^{2\pi} \frac{\partial \bar{p}^*}{\partial \epsilon} \sin\phi \, \mathrm{d}\phi \qquad k^*_{\gamma\gamma} = -\frac{3}{\epsilon_0}\int_0^{2\pi} \frac{\partial \bar{p}^*}{\partial \gamma} \sin\phi \, \mathrm{d}\phi$$

and

$$b^*_{\epsilon\epsilon} = -3\int_0^{2\pi} \frac{\partial \bar{p}^*}{\partial \epsilon'} \cos\phi \, \mathrm{d}\phi \qquad b^*_{\epsilon\gamma} = -\frac{3}{\epsilon_0}\int_0^{2\pi} \frac{\partial \bar{p}^*}{\partial \gamma'} \cos\phi \, \mathrm{d}\phi$$
$$b^*_{\gamma\epsilon} = -3\int_0^{2\pi} \frac{\partial \bar{p}^*}{\partial \epsilon'} \sin\phi \, \mathrm{d}\phi \qquad b^*_{\gamma\gamma} = -\frac{3}{\epsilon_0}\int_0^{2\pi} \frac{\partial \bar{p}^*}{\partial \gamma'} \sin\phi \, \mathrm{d}\phi$$

where

$$\frac{\partial \bar{p}^*}{\partial \epsilon} = \frac{1}{B}\left(\frac{\partial h}{\partial \epsilon} - \cos\phi\right) \qquad \frac{\partial \bar{p}^*}{\partial \gamma} = \frac{1}{B}\left(\frac{\partial h}{\partial \gamma} - \epsilon_0 \sin\phi\right)$$
$$\frac{\partial \bar{p}^*}{\partial \epsilon'} = \frac{1}{B}\frac{\partial h}{\partial \epsilon'} \qquad \frac{\partial \bar{p}^*}{\partial \gamma'} = \frac{1}{B}\frac{\partial h}{\partial \gamma'}$$

The derivatives of $\bar{p}^*$ are put equal to zero at negative values of $\bar{p}^*_0$. The stiffness and damping coefficients in the x, y-coordinate system can be calculated from

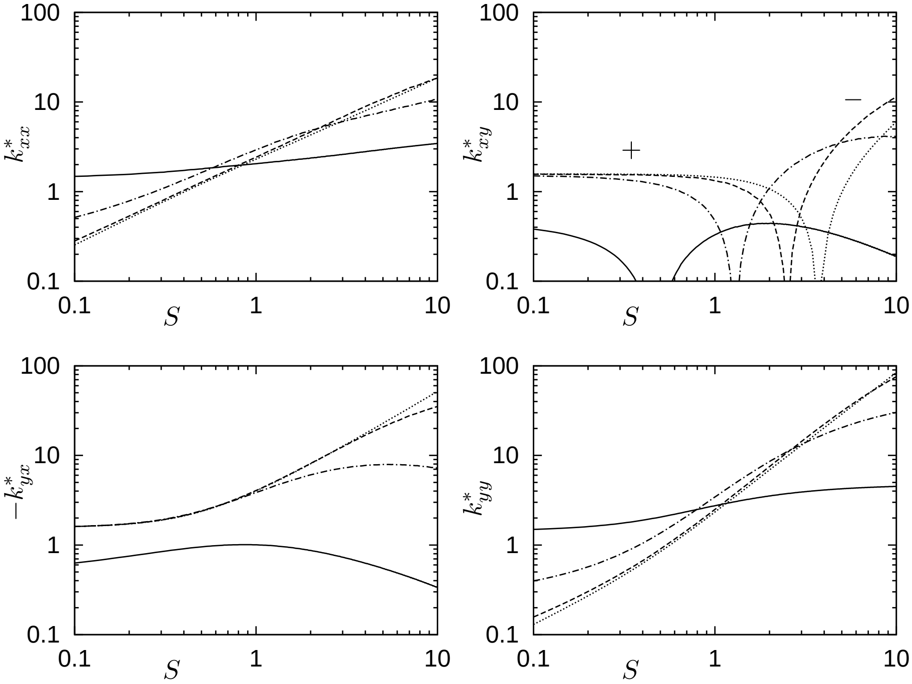

Figure 4.11: Compliant short-bearing stiffness coefficients for $L/D = 1$ and $\omega/\Omega = 1$ (dotted line: $B = 0$, dashed line: $B = 0.01$, dash-dotted line: $B = 0.1$, solid line: $B = 1$)

the stiffness and damping coefficients in the ϵ, γ-coordinate system according to

$$\begin{pmatrix} k^*_{xx} & k^*_{xy} \\ k^*_{yx} & k^*_{yy} \end{pmatrix} = \boldsymbol{R}^{\mathsf{T}} \begin{pmatrix} k^*_{\epsilon\epsilon} & k^*_{\epsilon\gamma} \\ k^*_{\gamma\epsilon} & k^*_{\gamma\gamma} \end{pmatrix} \boldsymbol{R}$$

$$\begin{pmatrix} b^*_{xx} & b^*_{xy} \\ b^*_{yx} & b^*_{yy} \end{pmatrix} = \boldsymbol{R}^{\mathsf{T}} \begin{pmatrix} b^*_{\epsilon\epsilon} & b^*_{\epsilon\gamma} \\ b^*_{\gamma\epsilon} & b^*_{\gamma\gamma} \end{pmatrix} \boldsymbol{R}$$

where the rotation matrix $\boldsymbol{R}$ is defined by

$$\boldsymbol{R} = \begin{pmatrix} \sin\gamma_0 & -\cos\gamma_0 \\ \cos\gamma_0 & \sin\gamma_0 \end{pmatrix}$$

Figures 4.11 and 4.12 show the stiffness and damping coefficients of the compliant short journal bearing for $L/D = 1$, $\omega/\Omega = 1$, and different values of B. The dotted lines in these figures represent the coefficients of the rigid short journal bearing.

If the nondimensional relative bearing-liner compliance is increased, the direct stiffness coefficients do not decrease for all values of the Sommerfeld number. For Sommerfeld numbers less than about one, these coefficients increase. This can be explained by the fact that the direct stiffness coefficients of a rigid journal bearing approach zero if the Sommerfeld number is decreased, whereas a

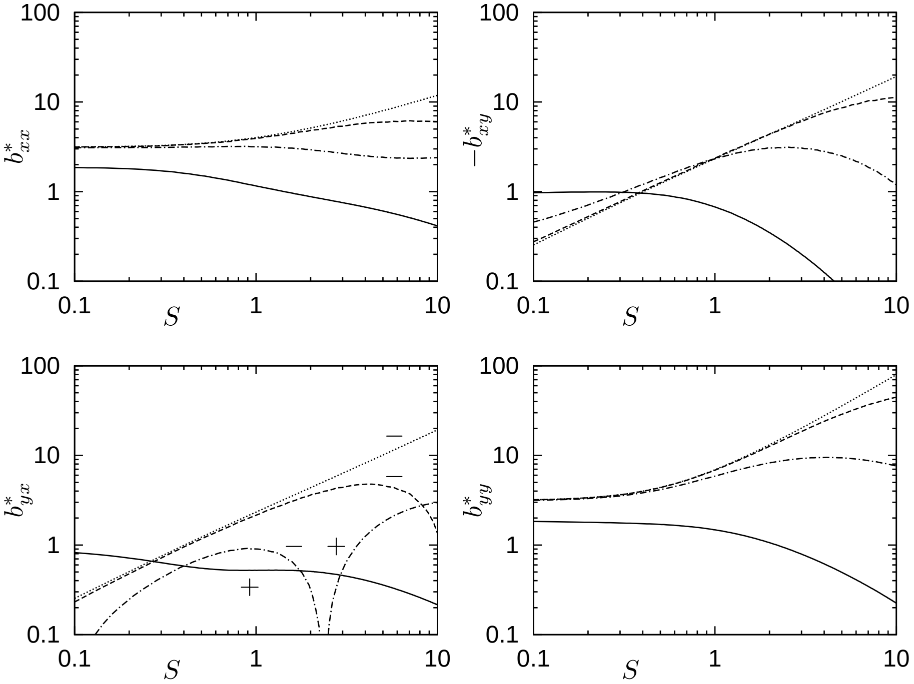

Figure 4.12: Compliant short-bearing damping coefficients for $L/D = 1$ and $\omega/\Omega = 1$ (dotted line: $B = 0$, dashed line: $B = 0.01$, dash-dotted line: $B = 0.1$, solid line: $B = 1$)

compliant bearing liner adds extra stiffness to the bearing. Therefore, if the Sommerfeld number is small the direct stiffness coefficients can increase when the nondimensional relative bearing-liner compliance is increased.

Long Bearing

For the long journal bearing, (4.29) is rewritten as

$$\frac{\partial}{\partial\theta}\left(h^3\frac{\partial p^*}{\partial\theta}\right) - \frac{\partial h}{\partial\theta} - 2\frac{\partial h}{\partial\tau} = 0 \tag{4.41}$$

where $p^* = (h - 1 - \epsilon\cos(\theta - \gamma))/B$. First, h_0 is solved from the stationary part of this equation given by

$$\frac{\partial}{\partial\theta}\left(h_0^3\frac{\partial p_0^*}{\partial\theta}\right) - \frac{\partial h_0}{\partial\theta} = 0$$

where $p_0^* = (h_0 - 1 - \epsilon_0\cos(\theta - \gamma_0))/B$, using the finite-difference method. The boundary conditions for p_0^* are periodicity with respect to θ and $p_0^* = 0$ at $\theta = 0$. The attitude angle γ_0 evaluated at the equilibrium position must be determined by iteration. The nondimensional bearing reaction force components in the x-

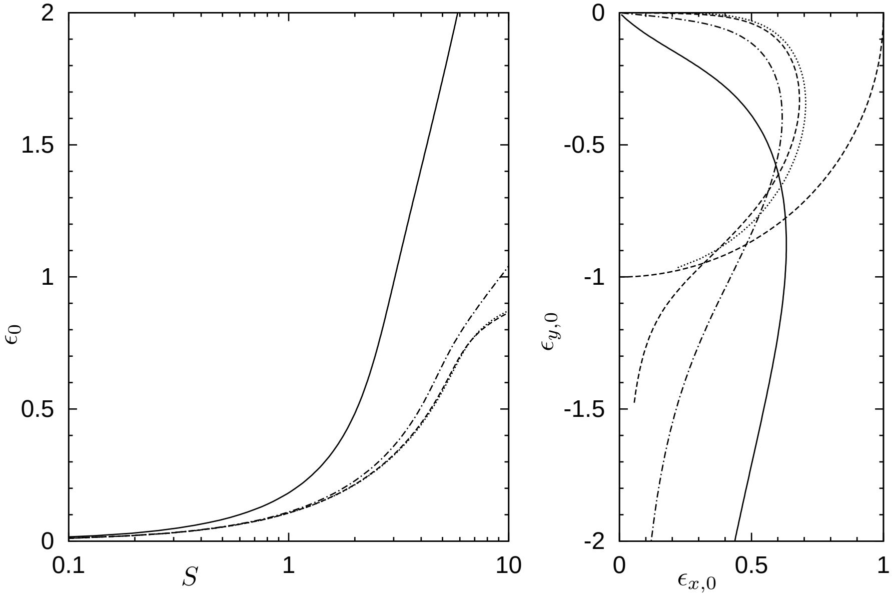

Figure 4.13: Compliant long-bearing nondimensional eccentricity versus Sommerfeld number and equilibrium locus (dotted line: $B = 0$, dashed line: $B = 0.01$, dash-dotted line: $B = 0.1$, solid line: $B = 1$)

and y-directions evaluated at the equilibrium position are given by

$$F^*_{x,0} = 3\int_0^{2\pi} p^*_0 \sin\theta \,\mathrm{d}\theta \quad \text{and} \quad F^*_{y,0} = -3\int_0^{2\pi} p^*_0 \cos\theta \,\mathrm{d}\theta$$

The Sommerfeld number evaluated at the equilibrium position is given by

$$S = \sqrt{F^{*2}_{x,0} + F^{*2}_{y,0}}$$

The left and right panels of figure 4.13 show the nondimensional eccentricity versus the Sommerfeld number and the equilibrium locus of the compliant long journal bearing, respectively, for different values of B. The dotted lines in this figure represent the results of the rigid long journal bearing model with a lubricant inlet at the top of the bearing, for which B is equal to zero. This bearing will be described later.

The remaining set of second-order ordinary differential equations in the derivatives of h, which follows from the substitution of (4.39) and (4.40) into (4.41), is given by

$$\frac{\partial}{\partial\theta}\left(3h_0^2\frac{\partial h}{\partial\epsilon}\frac{\partial p^*_0}{\partial\theta} + h_0^3\frac{\partial}{\partial\theta}\left(\frac{\partial p^*}{\partial\epsilon}\right)\right) - \frac{\partial}{\partial\theta}\left(\frac{\partial h}{\partial\epsilon}\right) + 2\left(\frac{\omega}{\Omega}\right)^2\frac{\partial h}{\partial\epsilon'} = 0$$
$$\frac{\partial}{\partial\theta}\left(3h_0^2\frac{\partial h}{\partial\gamma}\frac{\partial p^*_0}{\partial\theta} + h_0^3\frac{\partial}{\partial\theta}\left(\frac{\partial p^*}{\partial\gamma}\right)\right) - \frac{\partial}{\partial\theta}\left(\frac{\partial h}{\partial\gamma}\right) + 2\left(\frac{\omega}{\Omega}\right)^2\frac{\partial h}{\partial\gamma'} = 0$$

$$\frac{\partial}{\partial\theta}\left(3h_0^2\frac{\partial h}{\partial\epsilon'}\frac{\partial p_0^*}{\partial\theta}+h_0^3\frac{\partial}{\partial\theta}\left(\frac{\partial p^*}{\partial\epsilon'}\right)\right)-\frac{\partial}{\partial\theta}\left(\frac{\partial h}{\partial\epsilon'}\right)-2\frac{\partial h}{\partial\epsilon}=0$$
$$\frac{\partial}{\partial\theta}\left(3h_0^2\frac{\partial h}{\partial\gamma'}\frac{\partial p_0^*}{\partial\theta}+h_0^3\frac{\partial}{\partial\theta}\left(\frac{\partial p^*}{\partial\gamma'}\right)\right)-\frac{\partial}{\partial\theta}\left(\frac{\partial h}{\partial\gamma'}\right)-2\frac{\partial h}{\partial\gamma}=0$$

where

$$\frac{\partial p^*}{\partial\epsilon}=\frac{1}{B}\left(\frac{\partial h}{\partial\epsilon}-\cos(\theta-\gamma_0)\right)\qquad\frac{\partial p^*}{\partial\gamma}=\frac{1}{B}\left(\frac{\partial h}{\partial\gamma}-\epsilon_0\sin(\theta-\gamma_0)\right)$$
$$\frac{\partial p^*}{\partial\epsilon'}=\frac{1}{B}\frac{\partial h}{\partial\epsilon'}\qquad\frac{\partial p^*}{\partial\gamma'}=\frac{1}{B}\frac{\partial h}{\partial\gamma'}$$

This set of equations is solved by means of the finite-difference method, using the boundary conditions periodicity with respect to θ and the derivatives of p^* are equal to zero at $\theta = 0$.

The stiffness and damping coefficients are defined by

$$k_{xj}^*=-3\int_0^{2\pi}\frac{\partial p^*}{\partial\epsilon_j}\sin\theta\,\mathrm{d}\theta\qquad\qquad b_{xj}^*=-3\int_0^{2\pi}\frac{\partial p^*}{\partial\epsilon_j'}\sin\theta\,\mathrm{d}\theta$$
$$\text{and}$$
$$k_{yj}^*=3\int_0^{2\pi}\frac{\partial p^*}{\partial\epsilon_j}\cos\theta\,\mathrm{d}\theta\qquad\qquad b_{yj}^*=3\int_0^{2\pi}\frac{\partial p^*}{\partial\epsilon_j'}\cos\theta\,\mathrm{d}\theta$$

where $j = x, y$ and

$$\frac{\partial p^*}{\partial\epsilon_x}=\sin\gamma_0\frac{\partial p^*}{\partial\epsilon}+\frac{1}{\epsilon_0}\cos\gamma_0\frac{\partial p^*}{\partial\gamma}\qquad\frac{\partial p^*}{\partial\epsilon_y}=-\cos\gamma_0\frac{\partial p^*}{\partial\epsilon}+\frac{1}{\epsilon_0}\sin\gamma_0\frac{\partial p^*}{\partial\gamma}$$
$$\frac{\partial p^*}{\partial\epsilon_x'}=\sin\gamma_0\frac{\partial p^*}{\partial\epsilon'}+\frac{1}{\epsilon_0}\cos\gamma_0\frac{\partial p^*}{\partial\gamma'}\qquad\frac{\partial p^*}{\partial\epsilon_y'}=-\cos\gamma_0\frac{\partial p^*}{\partial\epsilon'}+\frac{1}{\epsilon_0}\sin\gamma_0\frac{\partial p^*}{\partial\gamma'}$$

The derivatives of p^* are put equal to zero at negative values of p_0^*. Figures 4.14 and 4.15 show the stiffness and damping coefficients of the compliant long journal bearing for $\omega/\Omega = 1$ and different values of B. The dotted lines in these figures represent the coefficients of the rigid long journal-bearing model with a lubricant inlet at the top of the bearing.

In case of a lubricant inlet at the top of the bearing, the boundary conditions are periodicity with respect to θ and $p^* = 0$ at $\theta = 0$. Using the long-bearing solution given by Gross (1962), the nondimensional pressure distribution in the lubricant film of the rigid long journal bearing with an inlet at the top can be expressed as

$$p^*=\frac{1}{(1+\epsilon\cos\gamma)^2}\left[\frac{(1-2\gamma')\epsilon\sin\gamma(2+\epsilon\cos\gamma)}{2+\epsilon^2}-\frac{\epsilon'}{\epsilon}\right]+\frac{1}{(1+\epsilon\cos(\theta-\gamma))^2}\left[\frac{(1-2\gamma')\epsilon\sin(\theta-\gamma)(2+\epsilon\cos(\theta-\gamma))}{2+\epsilon^2}+\frac{\epsilon'}{\epsilon}\right]\tag{4.42}$$

From this equation, the nondimensional pressure and its derivatives evaluated

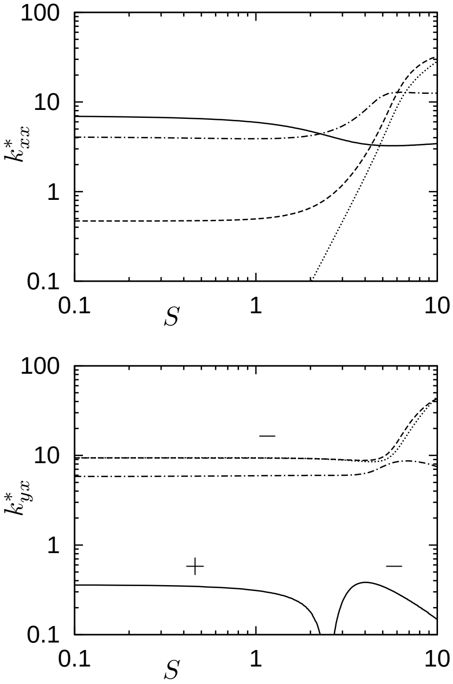

Figure 4.14: Compliant long-bearing stiffness coefficients for $\omega/\Omega = 1$ (dotted line: $B = 0$, dashed line: $B = 0.01$, dash-dotted line: $B = 0.1$, and solid line: $B = 1$)

at the equilibrium position can be calculated and are given by

$$
\begin{aligned}
p_0^* &= \frac{\epsilon_0}{2+\epsilon_0^2}\left[\frac{\sin\gamma_0(2+\epsilon_0\cos\gamma_0)}{(1+\epsilon_0\cos\gamma_0)^2}+\frac{\sin(\theta-\gamma_0)(2+\epsilon_0\cos(\theta-\gamma_0))}{(1+\epsilon_0\cos(\theta-\gamma_0))^2}\right]\\
\frac{\partial p^*}{\partial\epsilon} &= \frac{2-\epsilon_0^2}{(2+\epsilon_0^2)^2}\left[\frac{\sin\gamma_0(2+\epsilon_0\cos\gamma_0)}{(1+\epsilon_0\cos\gamma_0)^2}+\frac{\sin(\theta-\gamma_0)(2+\epsilon_0\cos(\theta-\gamma_0))}{(1+\epsilon_0\cos(\theta-\gamma_0))^2}\right]-\\
&\qquad \frac{\epsilon_0}{2+\epsilon_0^2}\left[\frac{\sin\gamma_0\cos\gamma_0(3+\epsilon_0\cos\gamma_0)}{(1+\epsilon_0\cos\gamma_0)^3}+\right.\\
&\qquad\qquad \left.\frac{\sin(\theta-\gamma_0)\cos(\theta-\gamma_0)(3+\epsilon_0\cos(\theta-\gamma_0))}{(1+\epsilon_0\cos(\theta-\gamma_0))^3}\right]\\
\frac{\partial p^*}{\partial\gamma} &= \frac{\epsilon_0}{2+\epsilon_0^2}\left[\frac{3\epsilon_0+(2+\epsilon_0^2)\cos\gamma_0}{(1+\epsilon_0\cos\gamma_0)^3}-\frac{3\epsilon_0+(2+\epsilon_0^2)\cos(\theta-\gamma_0)}{(1+\epsilon_0\cos(\theta-\gamma_0))^3}\right]\\
\frac{\partial p^*}{\partial\epsilon'} &= \frac{1}{\epsilon_0}\left[\frac{1}{(1+\epsilon_0\cos(\theta-\gamma_0))^2}-\frac{1}{(1+\epsilon_0\cos\gamma_0)^2}\right]\\
\frac{\partial p^*}{\partial\gamma'} &= -\frac{2\epsilon_0}{2+\epsilon_0^2}\left[\frac{\sin\gamma_0(2+\epsilon_0\cos\gamma_0)}{(1+\epsilon_0\sin\gamma_0)^2}+\frac{\sin(\theta-\gamma_0)(2+\epsilon_0\cos(\theta-\gamma_0))}{(1+\epsilon_0\cos(\theta-\gamma_0))^2}\right]
\end{aligned}
$$

The influence of the nondimensional relative bearing-liner compliance on the direct stiffness coefficients of the compliant long journal bearing is more com-

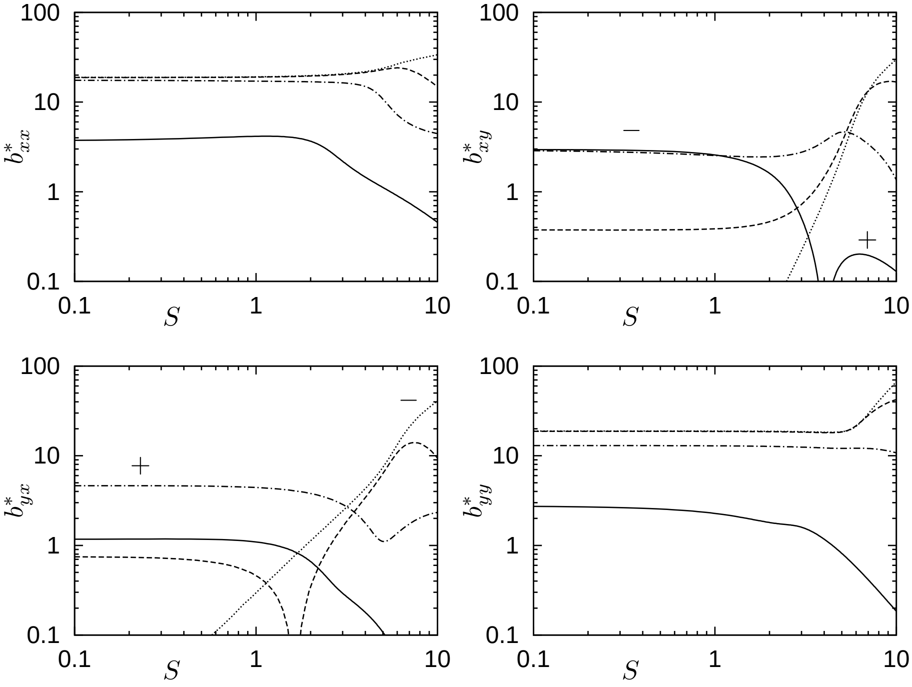

Figure 4.15: Compliant long-bearing damping coefficients for $\omega/\Omega = 1$ (dotted line: $B = 0$, dashed line: $B = 0.01$, dash-dotted line: $B = 0.1$, solid line: $B = 1$)

plicated than for the compliant short journal bearing, but for most values of the Sommerfeld number less than about six, these coefficients increase if the nondimensional relative bearing-liner compliance is increased. However, if the nondimensional relative bearing-liner compliance is increased to one, the direct stiffness coefficient in the vertical direction decreases again.

Chapter 5

Nonlinear Rotordynamic Analysis

In this chapter, the compliant journal-bearing models developed in the previous chapter will be applied in the model of a symmetric rotor-bearing system with a rigid rotor in two plain journal bearings. First, the nonlinear dynamics of the rigid rotor in rigid journal bearings will be investigated for different values of the unbalance. The results of this investigation will be used as the basis for the subsequent study of the nonlinear dynamics of the compliant journal-bearing models. The influence of the relative bearing-liner compliance on the nonlinear dynamics of both a balanced and an unbalanced rotor will be investigated. Some preliminary experiments were done on a rotor-bearing system with a flexible shaft in a water-lubricated rubber-lined journal bearing. A nonlinear phenomenon observed during these experiments will be briefly described.

5.1 Rotor-Bearing System

Figure 5.1 schematically shows a cross-section of one of the bearings of a symmetric rotor-bearing system with a rigid rotor. The rotor with mass m and unbalance a is supported by two plain journal bearings. The rotor rotates with a constant angular speed $\varOmega$ about the z-axis and a constant load F_0 is applied to the rotor in the negative y-direction. The equations of motion of the rotor are given by

$$\begin{cases} m\ddot{e}_x = 2F_x + m\varOmega^2 a\cos(\varOmega t) \\ m\ddot{e}_y = 2F_y + m\varOmega^2 a\sin(\varOmega t) - F_0 \end{cases}$$

where e_x and e_y are the displacement components of the rotor in the x- and y-directions, respectively, F_x and F_y are the nonlinear bearing reaction force components in the x- and y-directions, respectively, t is time, and an overdot denotes the total derivative with respect to t. With the nondimensional quantities $\epsilon_i = e_i/C$ ($i = x, y$ and C is the radial clearance), $F_i^* = (C/R)^2 F_i/\mu\varOmega_0 LD$ ($i = x, y, 0$, R is the journal radius, μ is the lubricant viscosity, L is the bearing length, and D is the journal diameter), $\varOmega^* = \varOmega/\varOmega_0$, $a^* = a/C$, and $\tau = \varOmega_0 t$, these equations can be rewritten as

$$\begin{cases} \epsilon_x'' = 2F_x^*/F_0^* + \varOmega^{*2} a^* \cos(\varOmega^* \tau) \\ \epsilon_y'' = 2F_y^*/F_0^* + \varOmega^{*2} a^* \sin(\varOmega^* \tau) - 1 \end{cases} \tag{5.1}$$

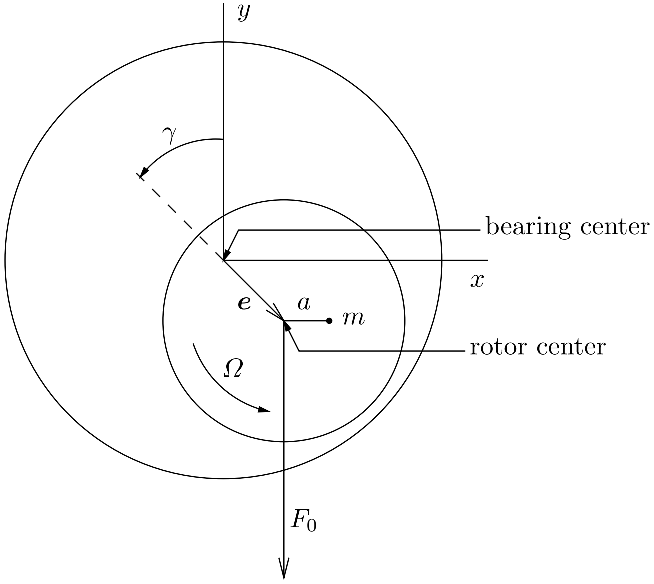

Figure 5.1: Cross-section of one of the bearings of a symmetric rigid rotor in two plain journal bearings

where a prime denotes the total derivative with respect to τ. The constant quantity Ω_0 is defined by $\sqrt{F_0/mC}$.

5.2 Rigid Bearings

First, the nonlinear dynamics of the rigid rotor in rigid journal bearings is studied for different values of the nondimensional unbalance. Two journal-bearing models will be considered: the short journal-bearing model and the long journal-bearing model. The bearing reaction force components can be found from the impedance components given by (4.11) for the short bearing and by (4.16) for the long bearing, respectively. As demonstrated in chapter 2, the autonomous state-space form of (5.1) has a dimension of six and is given by

$$\left\{\begin{aligned} u_1' &= u_2 \\ u_2' &= 2F_x^*/F_0^* + \Omega^{*2}a^*u_6 \\ u_3' &= u_4 \\ u_4' &= 2F_y^*/F_0^* + \Omega^{*2}a^*u_5 - 1 \\ u_5' &= u_5 + \Omega^*u_6 - u_5(u_5^2 + u_6^2) \\ u_6' &= -\Omega^*u_5 + u_6 - u_6(u_5^2 + u_6^2) \end{aligned}\right.$$

where $u_1 = \epsilon_x$, $u_2 = \epsilon_x'$, $u_3 = \epsilon_y$, $u_4 = \epsilon_y'$, and u_5 and u_6 are the extra state variables of the nonlinear oscillator. If the rotor is balanced, so that $a^* = 0$, the last two equations of the autonomous state-space form can be removed.

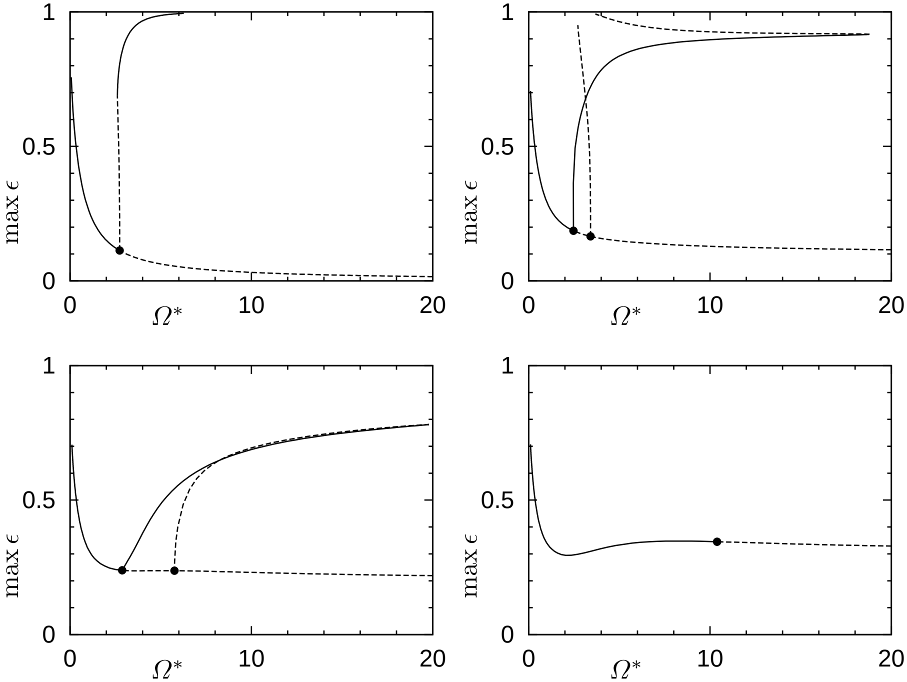

Figure 5.2: Bifurcation diagrams of rigid rotor with $a^* = 0$ (balanced), 0.1, 0.2, and 0.3 in rigid short journal bearings ($L/D = 1$, $F_0^* = 1$)

Short Bearings

Figure 5.2 shows the bifurcation diagrams of the rigid rotor with different values of the nondimensional unbalance a^* in rigid short journal bearings with $L/D = 1$ and $F_0^* = 1$. In the bifurcation diagrams, solid lines represent branches of stable solutions, dashed lines represent branches of unstable solutions, and dots represent bifurcation points. The nondimensional angular rotor speed Ω^* is used as the bifurcation parameter and the maximum nondimensional eccentricity $\max\epsilon$ is chosen as the scalar measure of the solutions that is plotted on the vertical axis.

The diagram for the balanced rotor with $a^* = 0$ in the upper-left panel of figure 5.2 contains a branch of fixed-points that becomes unstable at a primary Hopf bifurcation near $\Omega^* = 2.74$, known as the stability threshold.

This point can also be found by linearizing about the equilibrium position $\boldsymbol{\epsilon} = \epsilon_0(\sin\gamma_0, -\cos\gamma_0)$ and determining the stability of the resulting system. The linearized system is given by

$$\delta\boldsymbol{u}' = \begin{pmatrix} 0 & 1 & 0 & 0 \\ -k_{xx}^*/S & -2b_{xx}^*/F_0^* & -k_{xy}^*/S & -2b_{xy}^*/F_0^* \\ 0 & 0 & 0 & 1 \\ -k_{yx}^*/S & -2b_{yx}^*/F_0^* & -k_{yy}^*/S & -2b_{yy}^*/F_0^* \end{pmatrix} \delta\boldsymbol{u}$$

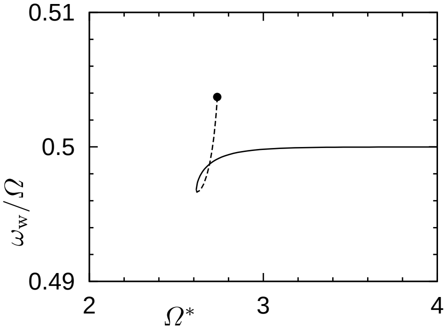

Figure 5.3: Angular whirl frequency to angular rotor speed ratio for balanced rigid rotor in rigid short journal bearings ($L/D = 1$, $F_0^* = 1$)

where $\Omega^* = F_0^*/2S$ was used, since the bearing load F_b is equal to $\frac{1}{2}F_0$, so that $S = F_0^*/2\Omega^*$. The characteristic equation of the linearized system is given by $s^4 + a_3s^3 + a_2s^2 + a_1s + a_0 = 0$, where

$$\begin{aligned}
a_0 &= (k_{xx}^* k_{yy}^* - k_{xy}^* k_{yx}^*)/S^2 \\
a_1 &= 2(k_{xx}^* b_{yy}^* - k_{xy}^* b_{yx}^* - k_{yx}^* b_{xy}^* + k_{yy}^* b_{xx}^*)/SF_0^* \\
a_2 &= (k_{xx}^* + k_{yy}^*)/S + 4(b_{xx}^* b_{yy}^* - b_{xy}^* b_{yx}^*)/F_0^{*2} \\
a_3 &= 2(b_{xx}^* + b_{yy}^*)/F_0^*
\end{aligned}$$

The equilibrium position is stable if the roots of the characteristic equation have negative real parts. According to the Routh criterion, this holds if the coefficients of the characteristic equation satisfy the following conditions:

1. $a_i > 0$
2. $a_1a_2a_3 - a_0a_3^2 - a_1^2 > 0$

The first condition is satisfied for all equilibrium positions. For $L/D = 1$ and $F_0^* = 1$, the second condition is satisfied for $\epsilon_0 < 0.11297$, so that the stability threshold is given by $\Omega^* = 2.7353$, which validates the previously found value.

From the primary Hopf bifurcation, an unstable branch of periodic solutions emanates, which becomes stable at a cyclic fold near $\Omega^* = 2.61$. The periodic solutions are known as $\frac{1}{2}\Omega$-whirl because of the fact that the angular whirl frequency ω_w of these vibrations is approximately equal to half the angular rotor speed Ω. Figure 5.3 demonstrates this by showing the angular whirl frequency to angular rotor speed ratio for a part of the branch of periodic solutions. To avoid large amplitude vibrations and the possibility of contact between the journal and the bearing, in practice the maximum angular rotor speed is limited by the stability threshold, or more precisely by the cyclic fold in the branch of $\frac{1}{2}\Omega$-whirl solutions if it is located below the stability threshold.

The diagrams of the unbalanced rotors with $a^* = 0.1$ and with $a^* = 0.2$ in the upper-right and lower-left panels of figure 5.2, respectively, contain a branch of period-1 solutions which contains two flip bifurcations. For $a^* = 0.1$, these flip bifurcations are located near $\Omega^* = 2.47$ and near $\Omega^* = 3.41$. From the left flip bifurcation, a stable branch of period-2 solutions emanates, which becomes unstable at a cyclic fold near $\Omega^* = 18.8$. From the right flip bifurcation, an unstable branch of period-2 solutions emanates and seems to be connected to the first branch of period-2 solutions at a point with $\max \epsilon \approx 1$. The branches of period-2 solutions cannot be continued to this point because of convergence problems caused by the singularity in the impedance components at $\epsilon = 1$. At the right flip bifurcation, the branch of period-1 solutions remains unstable because of the fact that one Floquet multiplier has a magnitude greater than 1, while another multiplier crosses the unit circle at -1. The branch of period-2 solutions that emanates from this flip bifurcation is also unstable, so that three unstable branches meet at this point. For $a^* = 0.2$, the two flip bifurcations are located near $\Omega^* = 2.87$ and near $\Omega^* = 5.76$, as shown in the lower-left panel of figure 5.2. A branch of period-2 solutions connects these flip bifurcations and contains a cyclic fold near $\Omega^* = 19.8$.

The diagram for the unbalanced rotor with $a^* = 0.3$ in the lower-right panel of the figure contains a branch of period-1 solutions, which becomes unstable at a secondary Hopf bifurcation near $\Omega^* = 10.4$. This secondary Hopf bifurcation results from the two flip bifurcations, present for smaller values of the unbalance, which coincide if the nondimensional unbalance is increased. The point at which the two flip bifurcations coincide is a so-called co-dimension two bifurcation at which two Floquet multipliers are equal to -1.

In the regions where no stable periodic solutions are found, the rotor-bearing system shows stable quasi-periodic behavior. A part of the quasi-periodic solution for the unbalanced rotor with $a^* = 0.3$ at $\Omega^* = 12$ is given in the lower-left panel of figure 2.2 in chapter 2.

Influence of Load

The influence of the nondimensional constant load F_0^* on the nonlinear dynamics of the rotor-bearing system is investigated by repeating the calculations for $F_0^* = 0.5$ and for $F_0^* = 2$. The bifurcation diagrams for $F_0^* = 0.5$ and $F_0^* = 2$ are shown in figures 5.4 and 5.5, respectively.

For the balanced rotor, the primary Hopf bifurcation is located near $\Omega^* = 2.76$ for $F_0^* = 0.5$ and near $\Omega^* = 2.67$ for $F_0^* = 2$. The stability threshold found using the linearized system is given by $\Omega^* = 2.7563$ for $F_0^* = 0.5$ and by $\Omega^* = 2.6712$ for $F_0^* = 2$. For the unbalanced rotor with $a^* = 0.1$, the two flip bifurcations in the branch of period-1 solutions are located near $\Omega^* = 2.47$ and near $\Omega^* = 3.81$ for $F_0^* = 0.5$, and near $\Omega^* = 2.49$ and near $\Omega^* = 3.11$ for $F_0^* = 2$. For $F_0^* = 0.5$, the branch of period-2 solutions emanating from the left flip bifurcation contains a cyclic fold near $\Omega^* = 23.2$ (not visible in the figure). For $F_0^* = 2$, the branch of period-2 solutions emanating from the left flip bifurcation starts unstable and contains two cyclic folds, one near $\Omega^* = 2.45$ and one near $\Omega^* = 15.6$, and the branch of period-2 solutions that emanates from the right flip bifurcation remains unstable at a cyclic fold near $\Omega^* = 3.14$ because one Floquet multiplier has a magnitude greater than 1, while another multiplier crosses the unit circle at $+1$. For $a^* = 0.2$, the two flip bifurcations in the branch of period-1 solutions are located near $\Omega^* = 8.88$ and near $\Omega^* = 10.1$ for $F_0^* = 0.5$, and near $\Omega^* = 2.40$ and near $\Omega^* = 3.96$ for $F_0^* = 2$. The branch of period-2 solutions connecting these flip bifurcations contains a cyclic fold near

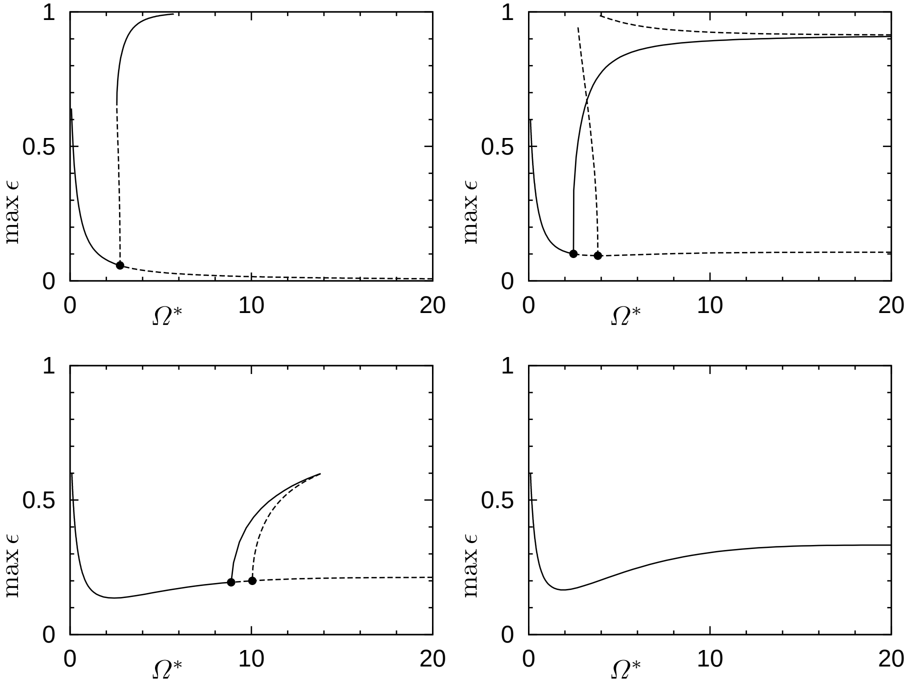

Figure 5.4: Bifurcation diagrams of rigid rotor with $a^* = 0$ (balanced), 0.1, 0.2, and 0.3 in rigid short journal bearings ($L/D = 1$, $F_0^* = 0.5$)

$\Omega^* = 13.8$ for both $F_0^* = 0.5$ and $F_0^* = 2$. For $a^* = 0.3$, the branch of period-1 solutions becomes unstable at a secondary Hopf bifurcation near $\Omega^* = 20.7$ (not visible in the figure) for $F_0^* = 0.5$. For $F_0^* = 2$, the branch of period-1 solutions contains two flip bifurcations, located near $\Omega^* = 4.70$ and near $\Omega^* = 6.37$. The branch of period-2 solutions connecting these flip bifurcations contains a cyclic fold near $\Omega^* = 9.63$.

For the balanced rotor and the unbalanced rotor with $a^* = 0.1$, the influence of F_0^* on the bifurcation diagrams is small. For $a^* = 0.2$, the angular rotor speed, at which the branch of period-1 solutions becomes unstable, seems to decrease if the load is increased. This contradicts with the expectation that increasing the load increases the stability, as for balanced rotors. But because of the scaling, the angular rotor speed Ω is proportional to $\Omega^* F_0^*$, so that indeed the angular rotor speed, at which the branch of period-1 solutions becomes unstable, increases when the load is increased. However, for $a^* = 0.3$ the angular rotor speed, at which the branch of period-1 solutions becomes unstable, is not monotonically increasing if the load is increased. It increases slightly from $F_0^* = 0.5$ to $F_0^* = 1$, but then decreases for $F_0^* = 2$, where the instability is caused by a flip bifurcation instead of a secondary Hopf bifurcation. Therefore, for an unbalanced rotor in rigid short journal bearing, the angular rotor speed, at which the branch of period-1 solutions becomes unstable, does not necessarily increase if the load is increased.

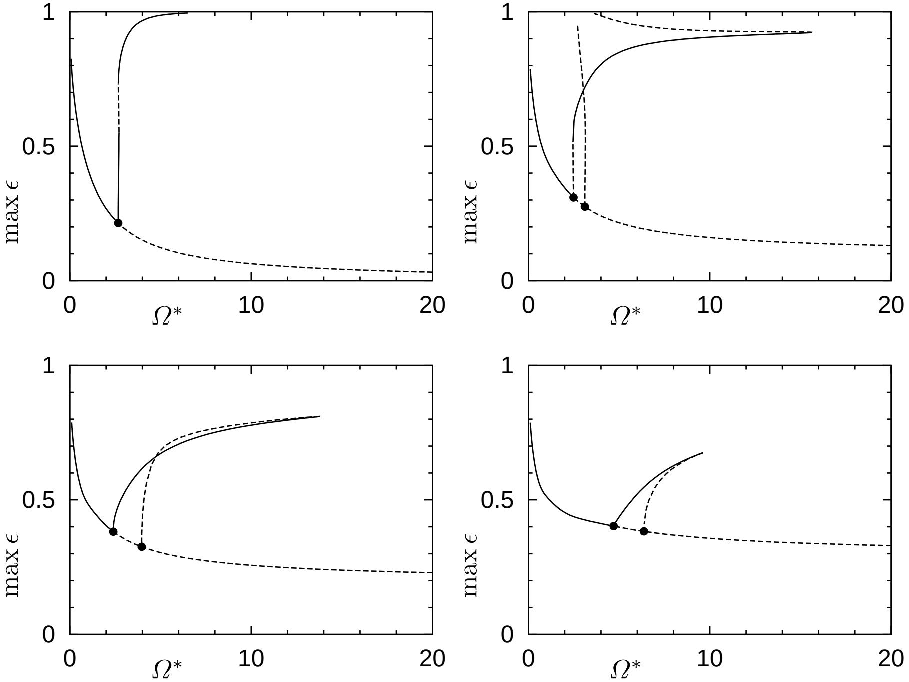

Figure 5.5: Bifurcation diagrams of rigid rotor with $a^* = 0$ (balanced), 0.1, 0.2, and 0.3 in rigid short journal bearings ($L/D = 1$, $F_0^* = 2$)

Long Bearings

Figure 5.6 shows the bifurcation diagrams of the rigid rotor with different values of the nondimensional unbalance a^* in rigid long journal bearings for $F_0^* = 2$. The diagram for the balanced rotor in the upper-left panel of this figure contains a branch of fixed-points, which becomes unstable at a primary Hopf bifurcation near $\Omega^* = 1.97$. The stability threshold found using the linearized system is given by $\Omega^* = 1.9594$. The branch of periodic solutions that emanates from the primary Hopf bifurcation is stable. The diagrams of the unbalanced rotors contain a branch of period-1 solutions which contains two flip bifurcations. For $a^* = 0.1$, the two flip bifurcations are located near $\Omega^* = 1.84$ and near $\Omega^* = 2.20$, as shown in the upper-right panel of figure 5.6. From the left flip bifurcation, a stable branch of period-2 solutions emanates, which becomes unstable at a cyclic fold near $\Omega^* = 16.3$ (not visible in the figure). From the right flip bifurcation, an unstable branch of period-2 solutions emanates and seems to be connected to the first branch of period-2 solutions at a point with $\max \epsilon \approx 1$. This point could not be found because of the same convergence problems as those encountered with the rotor in rigid short journal bearings. For $a^* = 0.2$, the two flip bifurcations are located near $\Omega^* = 1.76$ and near $\Omega^* = 2.76$, as shown in the lower-left panel of figure 5.6. A branch of period-2 solutions connects these flip bifurcations and contains a cyclic fold, which is located near $\Omega^* = 9.08$. The

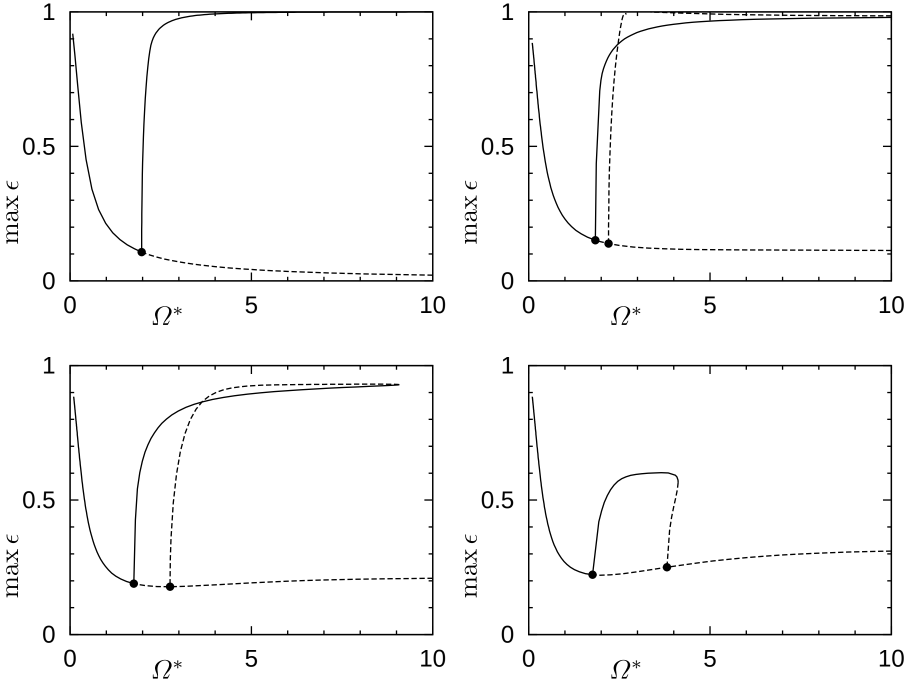

Figure 5.6: Bifurcation diagrams of rigid rotor with $a^* = 0$ (balanced), 0.1, 0.2, and 0.3 in rigid long journal bearings ($F_0^* = 2$)

diagram for the unbalanced rotor with $a^* = 0.3$ in the lower-right panel of figure 5.6 contains two flip bifurcations, which are located near $\Omega^* = 1.76$ and near $\Omega^* = 3.81$. The cyclic fold in the branch of period-2 solutions that connects these flip bifurcations is located near $\Omega^* = 4.12$.

As for the rotor in rigid short journal bearings, in the regions where no stable periodic solutions are found, the rotor-bearing system exhibits stable quasi-periodic behavior.

5.3 Compliant Bearings

In this section, the nonlinear dynamics of a rigid rotor in compliant journal bearings is studied. The influence of the nondimensional relative bearing-liner compliance B on the nonlinear dynamics of both the balanced and an unbalanced rotor with $a^* = 0.2$ is investigated. Both the compliant short journal-bearing model and the compliant long journal-bearing model developed in the previous chapter are considered. The nonlinear partial differential equations that need to be added to the equations of motion of the rotor are given by (4.27) for the short journal bearing and by (4.29) for the long journal bearing, respectively. These partial differential equations are spatially discretized using finite differences with 50 mesh intervals in the circumferential direction of the bearings.

The autonomous state-space form of the rotor in compliant short journal bearings has a dimension of 56 and is given by

$$\begin{cases} u_1' = u_2 \\ u_2' = 2F_x^*/F_0^* + \Omega^{*2} a^* u_{56} \\ u_3' = u_4 \\ u_4' = 2F_y^*/F_0^* + \Omega^{*2} a^* u_{55} - 1 \\ \dfrac{\partial h}{\partial \tau} = -\frac{1}{2}\left(\dfrac{3h^3 \bar{p}^*}{(L/D)^2} + \Omega^* \dfrac{\partial h}{\partial \theta}\right) \\ u_{55}' = u_{55} + \Omega^* u_{56} - u_{55}(u_{55}^2 + u_{56}^2) \\ u_{56}' = -\Omega^* u_{55} + u_{56} - u_{56}(u_{55}^2 + u_{56}^2) \end{cases}$$

where $u_1 = \epsilon_x$, $u_2 = \epsilon_x'$, $u_3 = \epsilon_y$, $u_4 = \epsilon_y'$, $\bar{p}^* = (h - 1 - \epsilon_x \sin\theta + \epsilon_y \cos\theta)/B$ and u_{55} and u_{56} are the extra state variables of the nonlinear oscillator. Spatial discretization of the partial differential equation yields the expressions for u_5 to u_{54}. For the balanced rotor, the rotor-bearing system is autonomous and the nonlinear oscillator given by the last two equations of the autonomous state-space form can be removed, so that the dimension of the system becomes 54.

The autonomous state-space form of the rotor in compliant long journal bearings has a dimension of 55 because of the fact that the long journal-bearing model needs one boundary condition more than the short journal-bearing model and is given by

$$\begin{cases} u_1' = u_2 \\ u_2' = 2F_x^*/F_0^* + \Omega^{*2} a^* u_{55} \\ u_3' = u_4 \\ u_4' = 2F_y^*/F_0^* + \Omega^{*2} a^* u_{54} - 1 \\ \dfrac{\partial h}{\partial \tau} = \frac{1}{2}\left(\dfrac{\partial}{\partial \theta}\left(h^3 \dfrac{\partial p^*}{\partial \theta}\right) - \Omega^* \dfrac{\partial h}{\partial \theta}\right) \\ u_{54}' = u_{54} + \Omega^* u_{55} - u_{54}(u_{54}^2 + u_{55}^2) \\ u_{55}' = -\Omega^* u_{54} + u_{55} - u_{55}(u_{54}^2 + u_{55}^2) \end{cases}$$

where $u_1 = \epsilon_x$, $u_2 = \epsilon_x'$, $u_3 = \epsilon_y$, $u_4 = \epsilon_y'$, $p^* = (h - 1 - \epsilon_x \sin\theta + \epsilon_y \cos\theta)/B$ and u_{54} and u_{55} are the extra state variables of the nonlinear oscillator. Spatial discretization of the partial differential equation yields the expressions for u_5 to u_{53}. For the balanced rotor, the nonlinear oscillator can be removed and the dimension of the system becomes 53.

Short Bearings

Figure 5.7 shows the bifurcation diagrams of the balanced rotor in compliant short journal bearings with different values of B and with $L/D = 1$ and $F_0^* = 1$. The branch of fixed-points becomes unstable at a primary Hopf bifurcation near $\Omega^* = 2.74$, 2.72, 2.71, and 2.22, for $B = 0$, 0.01, 0.1, and 1, respectively. Therefore, the stability threshold decreases when the relative bearing-liner compliance is increased. As a practical example, consider a rigid rotor with $m = 1$ [kg] in two water-lubricated compliant plain journal bearings, with

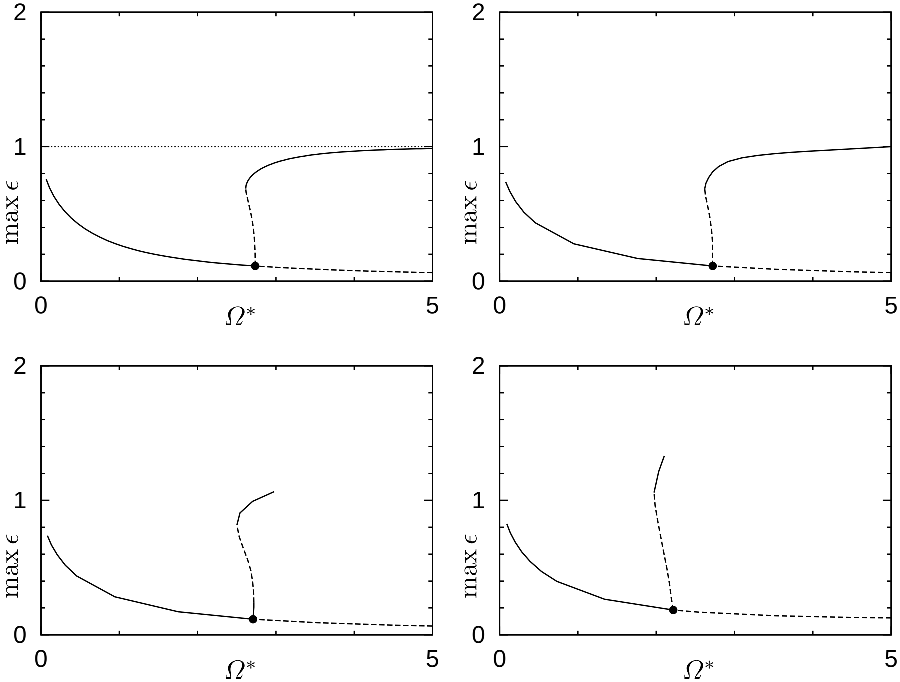

Figure 5.7: Bifurcation diagrams of balanced rigid rotor in compliant short journal bearings with $B = 0$ (rigid bearings), 0.01, 0.1, and 1 ($L/D = 1$, $F_0^* = 1$)

$L = D = 0.01$ [m], $C/R = 0.005$, and $\mu = 0.001$ [Ns/m^2]. Solving F_0 from the definition of F_0^*, substituting into the definition of Ω_0, and solving for Ω_0 yields $\Omega_0 = \mu LDF_0^*/mC(C/R)^2$. For this example, $\Omega_0 = 160$ [rad/s], so that the stability threshold decreases according to $\Omega = 438$, 435, 434, and 355 [rad/s], for $B = 0$, 0.01, 0.1, and 1, respectively. The unstable branches of periodic solutions emanating from the primary Hopf bifurcations become stable at cyclic folds near $\Omega^* = 2.61$, 2.62, 2.50, and 1.97, for $B = 0$, 0.01, 0.1, and 1, respectively. For $B = 0.1$, the branch of periodic solutions starts stable and becomes unstable at another cyclic fold near $\Omega^* = 2.72$.

For $B = 0.1$ and $B = 1$, the branch of periodic solutions is not continued because of the fact that at a certain point the minimum film thickness becomes negative. The fact that the minimum film thickness can become zero and even negative suggests that the compliant journal-bearing models predict the possibility of contact between the journal and the bearing. To exclude numerical inaccuracies, the path-following calculations are repeated with both a refined mesh in the circumferential direction and a refined mesh in time. Because these calculations yield the same result, it is concluded that, in contrast to rigid journal-bearing models, for the compliant journal-bearing models contact between the journal and the bearing is possible. For rigid journal-bearing models, contact cannot occur because of the fact that either an infinitely large load or an infinitely long time would be needed. Since contact is not included in the

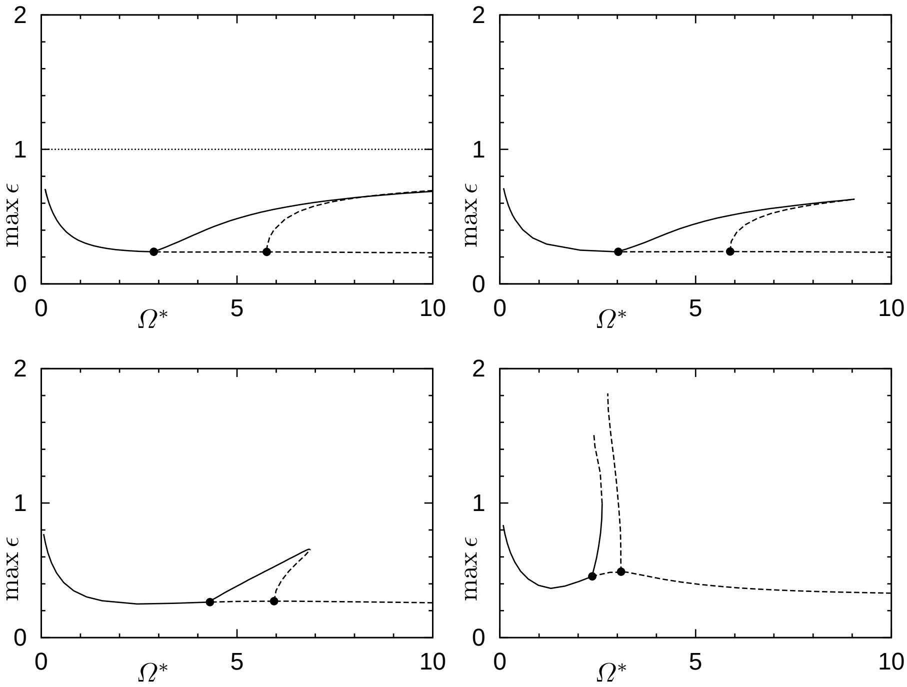

Figure 5.8: Bifurcation diagrams of unbalanced rigid rotor ($a^* = 0.2$) in compliant short journal bearings with $B = 0$ (rigid bearings), 0.01, 0.1, and 1 ($L/D = 1$, $F_0^* = 1$)

compliant journal-bearing models, physically impossible periodic solutions with negative film thicknesses can be found. Because of the fact that the minimum film thickness does not become positive again if the branch of periodic solutions is continued, the path-following calculations are stopped when the minimum film thickness becomes negative. Past the point at which the minimum film thickness becomes zero, contact between the journal and the bearing will occur. This contact causes increased bearing friction and wear of the journal and bearing surfaces, which must be avoided in practice.

Figure 5.8 shows the bifurcation diagrams of the unbalanced rotor with $a^* = 0.2$ in compliant short journal bearings with different values of B and with $L/D = 1$ and $F_0^* = 1$. The branch of period-1 solutions contains two flip bifurcations. The left flip bifurcation is located near $\Omega^* = 2.87$, 3.02, 4.31, and 2.36, for $B = 0$, 0.01, 0.1, and 1, respectively; the right flip bifurcation is located near $\Omega^* = 5.76$, 5.88, 5.95, and 3.10, for $B = 0$, 0.01, 0.1, and 1, respectively. It turns out that the nondimensional angular rotor speed, at which the branch of period-1 solutions becomes unstable, first increases and then decreases below the value for $B = 0$, when the nondimensional relative bearing-liner compliance is increased. For the practical example mentioned before, the point of instability changes according to $\Omega = 459$, 483, 690, and 378 [rad/s] for $B = 0$, 0.01, 0.1, and 1, respectively. The cyclic fold in the branch of period-2 solutions is located

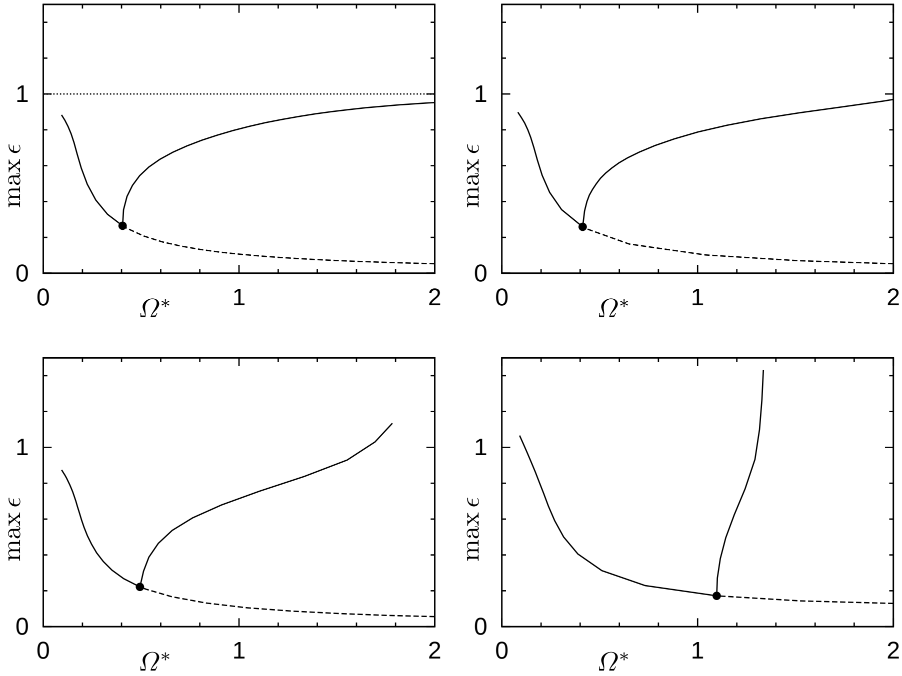

Figure 5.9: Bifurcation diagrams of balanced rigid rotor in compliant long journal bearings with $B = 0$ (rigid bearings), 0.01, 0.1, and 1 ($F_0^* = 2$)

near $\Omega^* = 19.8$, 9.06, and 6.87, for $B = 0$, 0.01, and 0.1, respectively. For $B = 1$, there are the two branches of period-2 solutions which are not continued because of the fact that the minimum film thickness becomes negative. The left branch of period-2 solutions contains a cyclic fold near $\Omega^* = 2.61$.

Long Bearings

Figure 5.9 shows the bifurcation diagrams of the balanced rotor in compliant long journal bearings with different values of B and with $F_0^* = 2$. The diagram for $B = 0$ is obtained using the rigid long journal-bearing model with a lubricant inlet at the top of the bearing, described in the previous chapter. The reaction force components of this bearing are calculated by integration of the pressure distribution given by (4.42). The branch of fixed-points becomes unstable at a primary Hopf bifurcation near $\Omega^* = 0.405$, 0.413, 0.494, and 1.10, for $B = 0$, 0.01, 0.1, and $B = 1$, respectively. Therefore, in contrast to the compliant short journal bearing, the stability threshold increases if the relative bearing-liner compliance is increased. For the practical example mentioned before, $\Omega_0 = 320$ [rad/s], so that the stability threshold increases according to $\Omega = 130$, 132, 158, and 352 [rad/s], for $B = 0$, 0.01, 0.1, and $B = 1$, respectively. The branch of periodic solution emanating from the primary Hopf bifurcation is stable. For $B = 0.1$ and $B = 1$, the branch of periodic solutions is not continued because of

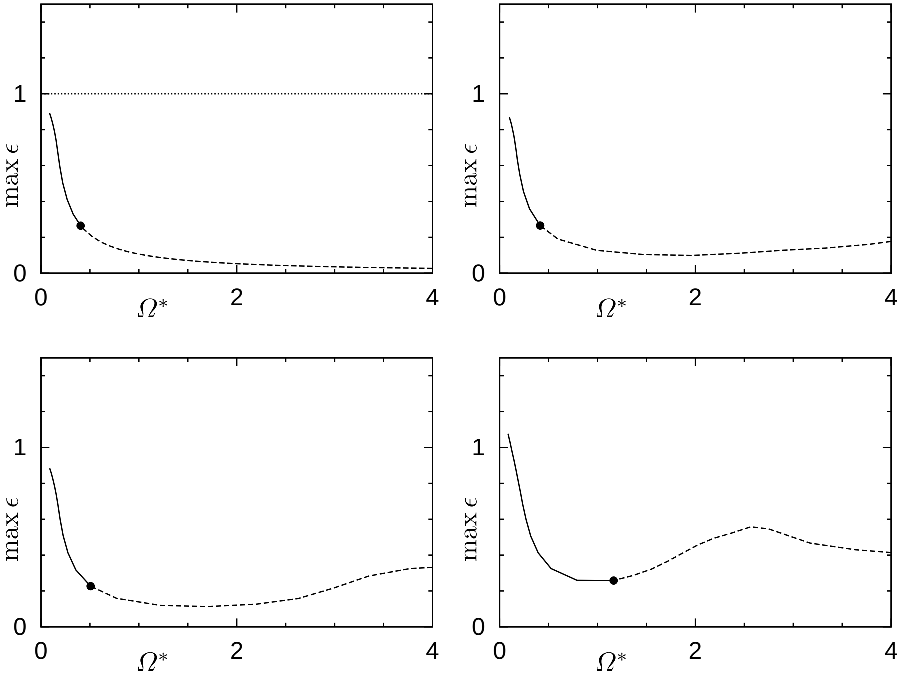

Figure 5.10: Bifurcation diagrams of unbalanced rigid rotor ($a^* = 0.2$) in compliant long journal bearings with $B = 0$ (rigid bearings), 0.01, 0.1, and 1 ($F_0^* = 2$)

the fact that the minimum film thickness becomes negative.

Figure 5.10 shows the bifurcation diagrams of the unbalanced rotor with $a^* = 0.2$ in compliant long journal bearings with different values of B and with $F_0^* = 2$. The branch of period-1 solutions becomes unstable at a secondary Hopf bifurcation near $\Omega^* = 0.405$, 0.414, 0.507, and 1.16, for $B = 0$, 0.01, 0.1, and 1, respectively. Therefore, the nondimensional angular rotor speed, at which the branch of period-1 solutions becomes unstable, increases if the nondimensional relative bearing-liner compliance is increased. For the practical example mentioned before, the point of instability increases according to $\Omega =$ 130, 132, 162, and 371 [rad/s], for $B = 0$, 0.01, 0.1, and 1, respectively.

For both the compliant short journal-bearing model and the compliant long journal-bearing model, in the regions where no stable periodic solutions are found using the path-following method, the minimum film thickness becomes negative if the system is integrated numerically.

5.4 Experiments

Some preliminary experiments were done on a rotor-bearing system with a flexible shaft in a water-lubricated rubber-lined journal bearing (Bongers, 2000). During these experiments a nonlinear phenomenon was observed, which is briefly described here.

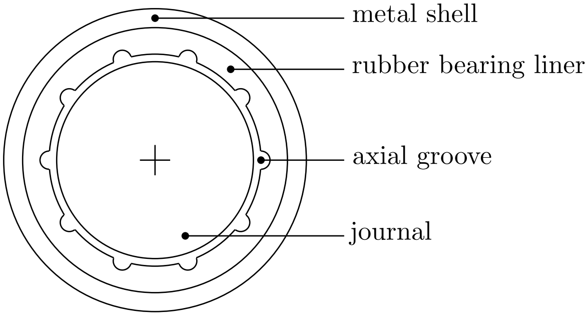

Figure 5.11: Water-lubricated rubber-lined journal bearing

The experiments were carried out on a commercially available test rig, containing a flexible steel shaft, with a diameter of 0.625" and a length of about 0.551 m, and two disks of about 0.525 kg each. The shaft is driven by an electric motor by way of a rubber coupling and the amount of unbalance can be adjusted by screwing small bolts into threaded holes in the disks. In the original test rig, the shaft is supported by two ball bearings. For the experiments, one of the ball bearings is replaced by a water-lubricated rubber-lined journal bearing with a diameter of 1", a length of 2", and a radial bearing clearance of about 0.04 mm. Figure 5.11 shows a schematic cross section of this bearing, which consists of a metal shell to which a rubber bearing liner is attached containing a number of axial grooves. This bearing is mounted into an aluminum bearing house, in which four proximity probes are positioned to measure the whirl of the shaft at both sides of the bearing. The rotor-bearing test rig is placed vertically to minimize the stabilizing effect of a constant load in the radial direction of the journal bearing by gravity. Figure 5.12 schematically shows the modified test rig.

During the experiments, a nonlinear phenomenon was observed. No extra unbalance was added to the disks, so that the rotor was excited by the initial amount of unbalance present in the system. The rotor speed was both slowly increased and slowly decreased between 55 and 75 Hz. The results of these measurements are depicted in figure 5.13, where the amplitude of the shaft whirl measured below the water-lubricated rubber-lined journal bearing is plotted against the rotor speed. The figure shows the resonance peak near 65 Hz, which is the first critical rotor speed. Between about 62 and 66.5 Hz, a nonlinear phenomenon can be observed. If the rotor speed is increased, the system jumps from large-amplitude vibrations to small-amplitude vibrations between about 65 and 66.5 Hz. If the rotor speed is decreased, the system jumps from small-amplitude vibrations to large-amplitude vibrations between about 64 and 62 Hz. This behavior is caused by two cyclic folds in the branch of periodic solutions, one near 66 Hz and one near 63 Hz. Between these cyclic folds, the branch of periodic solutions is unstable and can therefore not be found in the experiments. If the rotor speed is increased past the first cyclic fold or decreased past the second cyclic fold, there is locally no periodic solution, so that the system jumps to a remote part of the branch of periodic solutions.

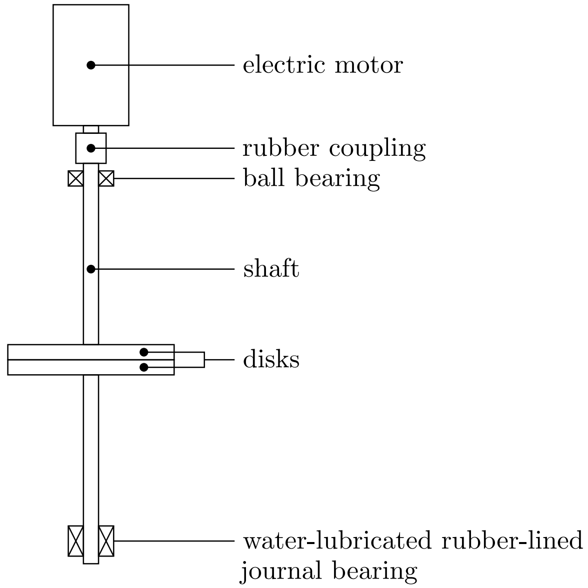

Figure 5.12: Rotor-bearing test rig

This nonlinear phenomenon is known from the so-called Duffing equation and is caused by a nonlinear stiffening spring. In the water-lubricated rubber-lined journal bearing, the stiffening behavior is probably caused by the rubber bearing liner. The maximum amplitude of the shaft whirl is about four times greater than the radial clearance of the bearing, so that the deformation of the rubber bearing liner is considerable. Because of the fact that for large compressions the stiffness of rubber increases, the bearing liner can behave as a stiffening spring.

The compliant journal-bearing models developed in this thesis use linear elasticity for the bearing liner, so that they cannot describe the experimentally observed nonlinear phenomenon. To correctly model the water-lubricated rubber-lined journal bearing for large bearing-liner deformations, the bearing-liner model needs to be extended to nonlinear elastic behavior.

5.5 Conclusions

The path-following calculations show that increasing the relative bearing-liner compliance decreases the stability threshold of the balanced rotor in compliant short journal bearings, while it increases the stability threshold of the same rotor in compliant long journal bearings. For the unbalanced rotor with $a^* = 0.2$ in compliant short journal bearings, the relative bearing-liner compliance has a significant influence on the location of the flip bifurcations at which the branch of period-1 solutions changes stability and on the branches of period-2 solutions that emanate from these flip bifurcations. For the same rotor in compliant long journal bearings, increasing the relative bearing-liner compliance increases the rotor speed of the secondary Hopf bifurcation, at which the branch of period-1 solutions becomes unstable.

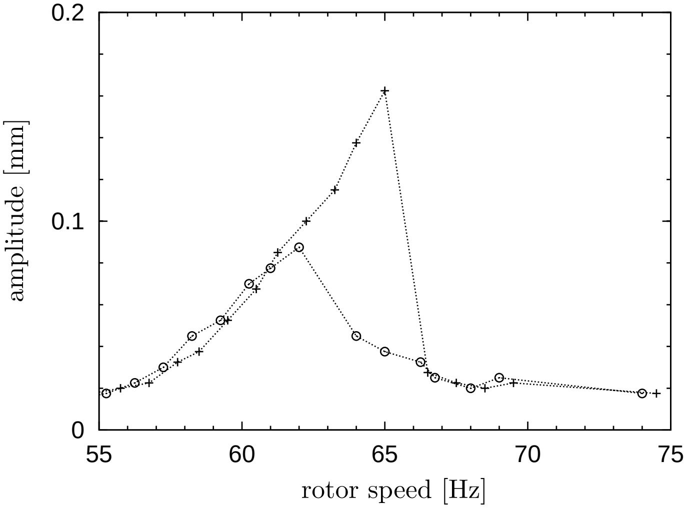

Figure 5.13: Nonlinear phenomenon (+: rotor speed increased, ⊙: rotor speed decreased)

In contrast to rigid journal-bearing models, during the path-following calculations with the compliant journal-bearing models, the minimum film thickness can become zero and even negative for certain branches of periodic solutions. In other words, the compliant journal-bearing models developed in this thesis predict the possibility of contact between the journal and the bearing. However, because contact is not included in the models, the calculations are stopped when the minimum film thickness becomes negative.

Experiments on a rotor-bearing system with a flexible shaft in a water-lubricated rubber-lined journal bearing demonstrate a nonlinear phenomenon, which is known from the Duffing equation. This nonlinear phenomenon cannot be described using the compliant journal-bearing models developed in this thesis because of the fact that linear elasticity is used for the bearing liner, whereas the observed phenomenon is probably caused by the nonlinear stiffening behavior of the rubber.

Chapter 6

Conclusions and Recommendations

In this chapter, the conclusions of this thesis will be drawn and a number of recommendations for further research will be given.

6.1 Conclusions

Compliant short and long plain journal-bearing models for rotordynamic applications have been developed. These models consist of spatially discretized nonlinear partial differential equations, which are in fact large systems of nonlinear ordinary differential equations. Because of the fact that the standard periodic solution solvers for nonlinear dynamic systems are developed for relatively small systems of ordinary differential equations, they are too inefficient for spatially discretized partial differential equations. Therefore, an efficient numerical method to calculate periodic solutions of general spatially discretized nonlinear partial differential equations has been developed by extending the finite-difference method using the NPGS approach. The finite-difference-based NPGS method proves to be more efficient than both the standard methods and the shooting-based NPGS method. However, the finite-difference-based NPGS method has the same disadvantages as the standard finite-difference method, such as numerical instability for stiff systems and inaccuracy for complicated periodic solutions containing higher harmonics. The rotor-bearing systems dealt with in this thesis appear to be not stiff and their periodic solutions to be relatively simple.

The compliant short and long plain journal-bearing models are based on the classical rigid short journal-bearing model and on a rigid long journal-bearing model with a lubricant inlet at the top, respectively. The stiffness and damping coefficients of the compliant journal-bearing models are calculated for different values of the relative bearing-liner compliance. It turns out that if the relative bearing-liner compliance is increased, the direct stiffness coefficients do not decrease for all values of the Sommerfeld number. The direct stiffness coefficients of the compliant short journal-bearing model increase for Sommerfeld numbers less than about one. For the complaint long journal-bearing model, the influence of the relative bearing-liner compliance on the direct stiffness coefficients is more complicated but for most values of the Sommerfeld number less than about six, these coefficients also increase. However, if the relative bearing-liner compliance is increased to one, the direct stiffness coefficient in the vertical direction of the compliant long journal-bearing model decreases again. The phenomenon that the direct stiffness coefficients increase when the relative bearing-liner compliance is increased can be explained by the fact that the direct stiffness coefficients of a rigid journal bearing approach zero if the Sommerfeld number is decreased, whereas a compliant bearing liner adds extra stiffness to the bearing. Therefore, if the Sommerfeld number is small the direct stiffness coefficients can increase when the relative bearing-liner compliance is increased.

The compliant journal-bearing models developed in this thesis have been applied in the model of a symmetric rotor-bearing system with a rigid rotor in two plain journal bearings. The nonlinear dynamics of this system have been studied for different values of the relative bearing-liner compliance. It turns out that increasing the relative bearing-liner compliance decreases the stability threshold of a balanced rotor in compliant short journal bearings, while it increases the stability threshold of the same rotor in compliant long journal bearings. For an unbalanced rotor in compliant short journal bearings, the relative bearing-liner compliance has a significant influence on the rotor speeds at which the branch of synchronous vibrations changes stability and on the shape of the branch of subsynchronous vibrations. For the same rotor in compliant long journal bearings, increasing the relative bearing-liner compliance causes an increase in the rotor speed, at which the branch of synchronous vibrations becomes unstable.

In contrast to rigid journal-bearing models, during the path-following calculations with the compliant journal-bearing models the minimum film thickness can become zero and even negative for certain branches of vibrations. In other words, the compliant plain journal-bearing models developed in this thesis predict the possibility of contact between the journal and the bearing. However, because contact is not included in the models, the calculations are stopped when the minimum film thickness becomes negative.

Experiments on a rotor-bearing system with a flexible shaft in a water-lubricated rubber-lined journal bearing demonstrate a nonlinear phenomenon. The branch of synchronous vibrations contains two so-called cyclic folds, at which the branch changes its direction. If the rotor speed is varied past one of these cyclic folds, the system jumps to a remote part of the branch of synchronous vibrations. This phenomenon is probably caused by the nonlinear elasticity of the rubber bearing liner of the water-lubricated rubber-lined journal bearing.

6.2 Recommendations

In the compliant plain journal-bearing models developed in this thesis, a simplified linear elasticity description for a thin liner on a rigid backing is used to describe the behavior of the elastic bearing liner. This can be improved by applying a more accurate linear elasticity description with for example finite elements. From the experiments on a rotor-bearing system with a flexible rotor in a water-lubricated rubber-lined journal bearing, it turned out that the rubber bearing liner exhibits nonlinear elastic behavior because of large compressions.

Therefore, to correctly model the water-lubricated rubber-lined journal bearing for large bearing-liner deformations, the bearing-liner model needs to be extended to nonlinear elasticity. Another possible extension of the bearing-liner model is to include damping.

The compliant plain journal-bearing models can be extended to journal bearings with more complicated geometries such as journal bearings with axial grooves and of finite length, so that more journal bearings that are used in practice can be modeled. From calculations on a rigid rotor in compliant plain journal bearings, it follows that in contrast to rigid journal-bearing models the film thickness of compliant journal-bearing models can become zero. Therefore, contact must be included in the compliant journal-bearing models, so that the path-following calculations can be continued past the points at which the minimum film thickness becomes zero.

For a verification of the numerical results presented in this thesis, experiments must be done on a rigid rotor in compliant plain journal bearings. Experiments, in which the film thickness of the journal bearings is measured, can be done to verify the numerical observation that the film thickness of compliant journal-bearings can become zero.

Appendix A

Derivation of the Reynolds Equation

Figure A.1 shows two projections of an infinitesimally small volume in the lubricant film of a journal bearing. In this figure, τ_ϕ and τ_z are the shear stresses in the ϕ- and z-directions, respectively, and the radial coordinate r is measured from the bearing surface. Neglecting inertial forces, the force balances for the infinitesimally small volume in the ϕ- and z-directions are given by

$$\delta p \delta r = \delta \tau_\phi R \delta \phi \quad \text{and} \quad \delta p \delta r = \delta \tau_z \delta z$$

The differential forms of these equations are given by

$$\frac{1}{R}\frac{\partial p}{\partial \phi} = \frac{\partial \tau_\phi}{\partial r} \quad \text{and} \quad \frac{\partial p}{\partial z} = \frac{\partial \tau_z}{\partial r} \tag{A.1}$$

Assuming a Newtonian fluid for the lubricant, it follows that

$$\tau_\phi = \mu \frac{\partial v_\phi}{\partial r} \quad \text{and} \quad \tau_z = \mu \frac{\partial v_z}{\partial r}$$

where v_ϕ and v_z are the velocities in the ϕ- and z-directions, respectively. Substitution of these expressions into (A.1) yields

$$\frac{1}{R}\frac{\partial p}{\partial \phi} = \mu \frac{\partial^2 v_\phi}{\partial r^2} \quad \text{and} \quad \frac{\partial p}{\partial z} = \mu \frac{\partial^2 v_z}{\partial r^2}$$

Solving v_ϕ and v_z from these equations, using the boundary conditions $v_\phi = 0$ at $r = 0$ and $v_\phi = \Omega R$ at $r = H$, and $v_z = 0$ at $r = 0$ and at $r = H$, yields

$$v_\phi = \frac{1}{2\mu R}\frac{\partial p}{\partial \phi} r(r - H) + \frac{\Omega R}{H} r \quad \text{and} \quad v_z = \frac{1}{2\mu}\frac{\partial p}{\partial z} r(r - H)$$

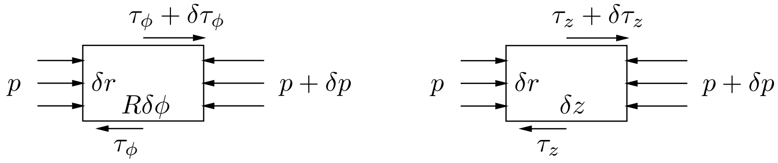

Figure A.1: Infinitesimally small volume

The volume transports in the ϕ- and z-directions are given by

$$q_\phi = \int_0^H v_\phi \,\mathrm{d}r = -\frac{H^3}{12\mu R}\frac{\partial p}{\partial \phi} + \tfrac{1}{2}\Omega R H \quad \text{and} \quad q_z = \int_0^H v_z \,\mathrm{d}r = -\frac{H^3}{12\mu}\frac{\partial p}{\partial z}$$

Substitution of these expressions into the equation of mass conservation, given by

$$\frac{1}{R}\frac{\partial q_\phi}{\partial \phi} + \frac{\partial q_z}{\partial z} + \frac{\partial H}{\partial t} = 0$$

yields the Reynolds equation:

$$\frac{1}{R^2}\frac{\partial}{\partial \phi}\left(H^3\frac{\partial p}{\partial \phi}\right) + H^3\frac{\partial^2 p}{\partial z^2} = 6\mu\left(\Omega\frac{\partial H}{\partial \phi} + 2\frac{\partial H}{\partial t}\right)$$

Appendix B

Rigid Bearing Stiffness and Damping Coefficients

In this appendix the analytical nondimensional stiffness and damping coefficients of the rigid short and long plain journal-bearing models will be listed.

B.1 Short Bearing

The nondimensional stiffness coefficients of the rigid short plain journal-bearing model are given by

$$
\begin{aligned}
k^*_{xx} &= \frac{2\epsilon_0\{16\epsilon_0^2 + \pi^2(2-\epsilon_0^2)\}}{(1-\epsilon_0^2)^2\{16\epsilon_0^2 + \pi^2(1-\epsilon_0^2)\}}\left(\frac{L}{D}\right)^2 \\
k^*_{xy} &= -\frac{\pi\{16\epsilon_0^4 - \pi^2(1-\epsilon_0^2)^2\}}{2(1-\epsilon_0^2)^{5/2}\{16\epsilon_0^2 + \pi^2(1-\epsilon_0^2)\}}\left(\frac{L}{D}\right)^2 \\
k^*_{yx} &= -\frac{\pi\{32\epsilon_0^2(1+\epsilon_0^2) + \pi^2(1-\epsilon_0^2)(1+2\epsilon_0^2)\}}{2(1-\epsilon_0^2)^{5/2}\{16\epsilon_0^2 + \pi^2(1-\epsilon_0^2)\}}\left(\frac{L}{D}\right)^2 \\
k^*_{yy} &= \frac{2\epsilon_0\{32\epsilon_0^2(1+\epsilon_0^2) + \pi^2(1-\epsilon_0^2)(1+2\epsilon_0^2)\}}{(1-\epsilon_0^2)^3\{16\epsilon_0^2 + \pi^2(1-\epsilon_0^2)\}}\left(\frac{L}{D}\right)^2
\end{aligned}
$$

The nondimensional damping coefficients of the rigid short plain journal-bearing model are given by

$$
\begin{aligned}
b^*_{xx} &= \frac{\pi\{\pi^2(1+2\epsilon_0^2) - 16\epsilon_0^2\}}{(1-\epsilon_0^2)^{3/2}\{16\epsilon_0^2 + \pi^2(1-\epsilon_0^2)\}}\left(\frac{L}{D}\right)^2 \\
b^*_{xy} &= b^*_{yx} = -\frac{4\epsilon_0\{\pi^2(1+2\epsilon_0^2) - 16\epsilon_0^2\}}{(1-\epsilon_0^2)^2\{16\epsilon_0^2 + \pi^2(1-\epsilon_0^2)\}}\left(\frac{L}{D}\right)^2 \\
b^*_{yy} &= \frac{\pi\{48\epsilon_0^2 + \pi^2(1-\epsilon_0^2)^2\}}{(1-\epsilon_0^2)^{5/2}\{16\epsilon_0^2 + \pi^2(1-\epsilon_0^2)\}}\left(\frac{L}{D}\right)^2
\end{aligned}
$$

B.2 Long Bearing

The nondimensional stiffness coefficients of the rigid long plain journal-bearing model are given by

$$
\begin{aligned}
k_{xx}^{*} &= \frac{6\epsilon_0\{4\epsilon_0^2 + \pi^2(2-\epsilon_0^2)\}}{(2+\epsilon_0^2)(1-\epsilon_0^2)\{4\epsilon_0^2 + \pi^2(1-\epsilon_0^2)\}} \\
k_{xy}^{*} &= -\frac{3\pi\{4\epsilon_0^4 - \pi^2(1-\epsilon_0^2)^2\}}{(2+\epsilon_0^2)(1-\epsilon_0^2)^{3/2}\{4\epsilon_0^2 + \pi^2(1-\epsilon_0^2)\}} \\
k_{yx}^{*} &= -\frac{3\pi\{8\epsilon_0^2(2+\epsilon_0^4) + \pi^2(1-\epsilon_0^2)(2-\epsilon_0^2+2\epsilon_0^4)\}}{(2+\epsilon_0^2)^2(1-\epsilon_0^2)^{3/2}\{4\epsilon_0^2 + \pi^2(1-\epsilon_0^2)\}} \\
k_{yy}^{*} &= \frac{6\epsilon_0\{8\epsilon_0^2(2+\epsilon_0^4) + \pi^2(1-\epsilon_0^2)(2-\epsilon_0^2+2\epsilon_0^4)\}}{(2+\epsilon_0^2)^2(1-\epsilon_0^2)^2\{4\epsilon_0^2 + \pi^2(1-\epsilon_0^2)\}}
\end{aligned}
$$

The nondimensional damping coefficients of the rigid long plain journal-bearing model are given by

$$
\begin{aligned}
b_{xx}^{*} &= \frac{3\pi(\pi^2 - 4\epsilon_0^2)}{\sqrt{1-\epsilon_0^2}\{4\epsilon_0^2 + \pi^2(1-\epsilon_0^2)\}} \\
b_{xy}^{*} &= -\frac{6\epsilon_0(\pi^2 - 4\epsilon_0^2)}{(1-\epsilon_0^2)\{4\epsilon_0^2 + \pi^2(1-\epsilon_0^2)\}} \\
b_{yx}^{*} &= -\frac{6\epsilon_0\{\pi^2(2+2\epsilon_0^2-\epsilon_0^4) - 8\epsilon_0^2\}}{(2+\epsilon_0^2)(1-\epsilon_0^2)\{4\epsilon_0^2 + \pi^2(1-\epsilon_0^2)\}} \\
b_{yy}^{*} &= \frac{6\pi\{2\epsilon_0^2(6-2\epsilon_0^2-\epsilon_0^4) + \pi^2(1-\epsilon_0^2)^2\}}{(2+\epsilon_0^2)(1-\epsilon_0^2)^{3/2}\{4\epsilon_0^2 + \pi^2(1-\epsilon_0^2)\}}
\end{aligned}
$$

References

Adiletta, G., Guido, A.R., and Rossi, C. (1996), "Chaotic Motions of a Rigid Rotor in Short Journal Bearings," *Nonlinear Dynamics* **10**(3), 251–269.

Adiletta, G., Guido, A.R., and Rossi, C. (1997a), "Nonlinear Dynamics of a Rigid Unbalanced Rotor in Journal Bearings. Part I: Theoretical Analysis," *Nonlinear Dynamics* **14**(1), 57–87.

Adiletta, G., Guido, A.R., and Rossi, C. (1997b), "Nonlinear Dynamics of a Rigid Unbalanced Rotor in Journal Bearings. Part II: Experimental Analysis," *Nonlinear Dynamics* **14**(2), 157–189.

Armstrong, C.G. (1986), "An Analysis of the Stresses in a Thin Layer of Articular Cartilage in a Synovial Joint," *Engineering in Medicine* **15**(2), 55–61.

Ascher, U.M., Mattheij, R.M.M., and Russell, R.D. (1995), *Numerical Solution of Boundary Value Problems for Ordinary Differential Equations*, Society for Industrial and Applied Mathematics, Philadelphia.

Blok, H. (1975), "Full Journal Bearings under Dynamic Duty: Impulse Method of Solution and Flapping Action," *Journal of Lubrication Technology* **97**(2), 168–178.

Bongers, H. (2000), *The Dynamics of a Rubber Bearing*, Report WFW 2000.14, Eindhoven University of Technology, Eindhoven, The Netherlands.

Booker, J.F. (1965a), "Dynamically Loaded Journal Bearings: Mobility Method of Solution," *Journal of Basic Engineering* **87**(3), 537–546.

Booker, J.F. (1965b), "A Table of the Journal Bearing Integral," *Journal of Basic Engineering* **87**(2), 533–535.

Booker, J.F. (1969), "Dynamically Loaded Journal Bearings: Maximum Film Pressure," *Journal of Lubrication Technology* **91**(3), 534–537.

Booker, J.F. (1971), "Dynamically Loaded Journal Bearings: Numerical Application of the Mobility Method," *Journal of Lubrication Technology* **93**(1), 168–174.

Childs, D.W. (1993), *Turbomachinery Rotordynamics: Phenomena, Modeling and Analysis*, Wiley-Interscience, Chichester.

Childs, D.W., Moes, H., and van Leeuwen, H.J. (1977), “Journal Bearing Impedance Descriptions for Rotordynamic Applications,” *Journal of Lubrication Technology* **99**(2), 198–210.

Conway, H.D. and Lee, H.C. (1975), “The Analysis of the Lubrication of a Flexible Journal Bearing,” *Journal of Lubrication Technology* **97**(4), 599–604.

Conway, H.D. and Lee, H.C. (1977), “The Lubrication of Short, Flexible Journal Bearings,” *Journal of Lubrication Technology* **99**(3), 376–378.

Doedel, E.J., Champneys, A.R., Fairgrieve, T.F., Kuznetsov, Y.A., Sandstede, B., and Wang, X. (1998), *AUTO 97: Continuation and Bifurcation Software for Ordinary Differential Equations*, Concordia University, Montreal, Canada.

Doedel, E., Keller, H.B., and Kernevez, J.P. (1991), “Numerical Analysis and Control of Bifurcation Problems: (I) Bifurcation in Finite Dimensions,” *International Journal of Bifurcation and Chaos* **1**(3), 493–520.

Dowson, D. and Higginson, G.R. (1959), “A Numerical Solution to the Elasto-Hydrodynamic Problem,” *Journal of Mechanical Engineering Science* **1**(1), 6–15.

Dowson, D. and Higginson, G.R. (1977), *Elasto-Hydrodynamic Lubrication, SI Edition*, Pergamon Press, Oxford.

Ehrich, F.F., ed. (1992), *Handbook of Rotordynamics*, McGraw-Hill, London.

Fantino, B. and Frene, J. (1985), “Comparison of Dynamic Behavior of Elastic Connecting-Rod Bearing in Both Petrol and Diesel Engines,” *Journal of Tribology* **107**(1), 87–91.

Fey, R.H.B. (1992), *Steady-State Behaviour of Reduced Dynamic Systems with Local Nonlinearities*, Ph.D. thesis, Eindhoven University of Technology, Eindhoven, The Netherlands.

Fey, R.H.B., van Campen, D.H., and de Kraker, A. (1996), “Long Term Structural Dynamics of Mechanical Systems with Local Nonlinearities,” *Journal of Vibration and Acoustics* **118**(2), 147–153.

Fuller, D.D. (1984), *Theory and Practice of Lubrication for Engineers*, 2nd edn., Wiley-Interscience, Chichester.

Glienicke, J. and Walter, J. (1980), “Schnelle Abschätzung der Biegekritischen Drehzahlen und Stabilitätsgrenzen Gleitgelagerter Wellen (Fast Estimation of Bending Critical Speeds and Stability Boundaries of Shafts in Journal Bearings),” *Antriebstechnik* **19**(1–2), 23–26, in German.

Goenka, P.K. and Oh, K.P. (1986), “An Optimum Short Bearing Theory for the Elastohydrodynamic Solution of Journal Bearings,” *Journal of Tribology* **108**(2), 294–299.

Gohar, R. (1988), *Elastohydrodynamics*, Ellis Horwood, Chichester.

Gross, W.A. (1962), *Gas Film Lubrication*, Wiley, New York.

Higginson, G.R. (1966), "The Theoretical Effects of Elastic Deformation of the Bearing Liner on Journal Bearing Performance," *Proceedings of the Institution of Mechanical Engineers (Elastohydrodynamic Lubrication Symposium, Leeds, England)* **180**(3B), 31–38.

Hlaváček, M. and Vokoun, D. (1993), "Lubrication of a Cylindrical Synovial Joint Considering Rolling Motion and Elastic Incompressible Cartilage," *Wear* **165**(1), 1–7.

Holodniok, M., Knedlik, P., and Kubíček, M. (1987), "Continuation of Periodic Solutions in Parabolic Differential Equations," in Küpper, T. *et al.*, eds., *Bifurcation: Analysis, Algorithms, Applications (Proceedings of the Conference at the University of Dortmund)*, Dortmund, Germany, vol. INSM 79, 122–130.

Jansen, W. (1995), *CANDYS/QA: Algorithms, Programs, and User's Manual*, Universität Potsdam, Potsdam, Germany.

Kirk, R.G. and Gunter, E.J. (1976a), "Short Bearing Analysis Applied to Rotor Dynamics, Part 1: Theory," *Journal of Lubrication Technology* **98**(1), 47–56.

Kirk, R.G. and Gunter, E.J. (1976b), "Short Bearing Analysis Applied to Rotor Dynamics, Part 2: Results of Journal Bearing Response," *Journal of Lubrication Technology* **98**(2), 319–329.

LaBouff, G.A. and Booker, J.F. (1985), "Dynamically Loaded Journal Bearings: A Finite Element Treatment for Rigid and Elastic Surfaces," *Journal of Tribology* **107**(4), 505–513.

Leine, R.I., van Campen, D.H., and van de Vrande, B.L. (2000), "Bifurcations in Nonlinear Discontinuous Systems," *Nonlinear Dynamics* **23**(2), 105–164.

Lund, J.W. (1987), "Review of the Concept of Dynamic Coefficients for Fluid Film Journal Bearings," *Journal of Tribology* **109**(1), 37–41.

Lust, K. (1997), *Numerical bifurcation analysis of periodic solutions of partial differential equations*, Ph.D. thesis, Katholieke Universiteit Leuven, Leuven, Belgium.

Moes, H. and Bosma, R. (1981), "Mobility and Impedance Definitions for Plain Journal Bearings," *Journal of Lubrication Technology* **103**(3), 468–470.

Muijderman, E.A. (1967), "Analysis and Design of Spiral-Groove Bearings," *Journal of Lubrication Technology* **89**(3), 291–306.

Muijderman, E.A. (1986), "Algebraic Formulas for the Threshold and Mode of Instability and the First Critical Speed of a Simple Flexibly Supported (Overhung) Rotor-Bearing System," in *Proceedings of the International Conference on Rotordynamics*, Tokyo, Japan, 201–210.

Nilsson, L.R.K. (1979), "The Influence of Bearing Flexibility on the Dynamic Performance of Radial Oil Film Bearings," in Dowson, D. *et al.*, eds., *Elastohydrodynamics and Related Topics (Proceedings of the 5th Leeds-Lyon Symposium on Tribology)*, Leeds, England, 311–319.

Ocvirk, F.W. and DuBois, G.B. (1953), *Analytical Derivation and Experimental Evaluation of Short Bearing Approximations of Full Journal Bearings*, Report 1157, NACA.

Oh, K.P. and Goenka, P.K. (1985), "The Elastohydrodynamic Solution of Journal Bearings under Dynamic Loading," *Journal of Tribology* **107**(3), 389–394.

Parker, T.S. and Chua, L.O. (1989), *Practical Numerical Algorithms for Chaotic Systems*, Springer, Berlin.

Reinhoudt, J.P. (1972), *On the Stability of Rotor-and-Bearing Systems and on the Calculation of Sliding Bearings*, Ph.D. thesis, Eindhoven University of Technology, Eindhoven, The Netherlands.

Reynolds, O. (1886), "On the Theory of Lubrication and its Application to Mr. Beauchamp Tower's Experiments, Including an Experimental Determination of the Viscosity of Olive Oil," *Philosophical Transactions of the Royal Society of London* **177**, 157–234.

Seydel, R. (1988), *From Equilibrium to Chaos: Practical Bifurcation and Stability Analysis*, Elsevier, New York.

Seydel, R. (1999), *BIFPACK: A Program Package for Continuation, Bifurcation, and Stability Analysis*, Universität Ulm, Ulm, Germany.

Someya, T., ed. (1989), *Journal-Bearing Databook*, Springer, Berlin.

Sommerfeld, A. (1904), "Zur Hydrodynamischen Theorie der Schmiermittelreibung," *Zeitschrift für Mathematik und Physik* **40**, 97–155.

van der Tempel, L., Moes, H., and Bosma, R. (1985), "Numerical Simulation of Dynamically Loaded Flexible Short Journal Bearings," *Journal of Tribology* **107**(3), 396–401.

Vance, J.M. (1988), *Rotordynamics of Turbomachinery*, Wiley-Interscience, Chichester.

van de Vorst, E.L.B. (1996), *Long Term Dynamics and Stabilization of Nonlinear Mechanical Systems*, Ph.D. thesis, Eindhoven University of Technology, Eindhoven, The Netherlands.

van de Vorst, E.L.B., Fey, R.H.B., de Kraker, A., and van Campen, D.H. (1996), "Steady-State Behaviour of Flexible Rotordynamic Systems with Oil Journal Bearings," *Nonlinear Dynamics* **11**(3), 295–313.

van de Vrande, B.L., van Campen, D.H., and de Kraker, A. (1997), "Some Aspects of the Analysis of Stick-Slip Vibrations with an Application to Drill Strings," in *Proceedings of the 1997 ASME Design Engineering Technical Conferences*, Sacramento, California, paper DETC97/VIB-4109, 8 pages, CD-ROM.

van de Vrande, B.L., van Campen, D.H., and de Kraker, A. (1999), “An Approximate Analysis of Dry-Friction-Induced Stick-Slip Vibrations by a Smoothing Procedure,” *Nonlinear Dynamics* **19**(2), 159–171.

van de Vrande, B.L. and de Kraker, A. (1999), “Influence of Bearing Compliance on Long-Term Nonlinear Rotordynamics,” in *Proceedings of the 1999 ASME Design Engineering Technical Conferences*, Las Vegas, Nevada, paper DETC99/VIB-8043, 6 pages, CD-ROM.

de Witte, F.C. *et al.* (2000), *DIANA User’s Manual, Version 8*, TNO Building and Construction Research, Delft, The Netherlands.

Curriculum Vitæ

Since 2000	Working on software development for mechatronic systems at the Philips Center for Industrial Technology (CFT) in Eindhoven
Until 2000	Ph.D. student (Assistent in Opleiding) at the Eindhoven University of Technology (TUE), in association with TNO Building and Construction Research in Delft
1996	Mechanical Engineering degree (with high appreciation) at the TUE Final work “Modeling Dry Friction in DIANA,” in association with Shell Research/KSEPL in Rijswijk, awarded best report by the Royal Institute of Engineers (Koninklijk Instituut van Ingenieurs)
1991	Propædeutic degree (with high appreciation) at the TUE
1990	Atheneum-β degree at the St.-Odulphus high school in Tilburg

The author wishes to acknowledge his appreciation to TNO Building and Construction Research for the partial financial support and to all who assisted in the preparation of this thesis.